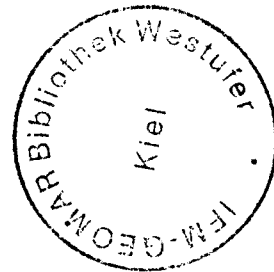


B 2006/1111

**Subduction of the Nazca Ridge
at the Peruvian margin:
Insights from geophysical data, analogue
and numerical modelling**



Dissertation

zur Erlangung des Doktorgrades
im Fachbereich Geowissenschaften
der Freien Universität Berlin

vorgelegt von

Andrea Hampel

März 2003



Erstgutachter:

Zweitgutachter:

Tag der öffentlichen Disputation:

Prof. Dr. Onno Oncken

Prof. Dr. Hans-Jürgen Götze

31. März 2003

*Und hätt' ich nicht geschüttelt und gerüttelt,
Wie wäre diese Welt so schön? -
Wie ständen eure Berge droben
In prächtig-reinem Ätherblau,
Hätt' ich sie nicht hervorgeschoben
Zu malerisch-entzückter Schau?*

Seismos in: Faust. Der Tragödie zweiter Teil
Johann Wolfgang von Goethe (1749-1832)

Contents

Abstract

Zusammenfassung

1 Introduction

2 The Peruvian active margin - geodynamic setting and a new model for the subduction history of the Nazca Ridge 5

- 2.1 The Nazca Ridge 6
- 2.2 The collision zone of the Nazca Ridge and the Peruvian margin 8
- 2.3 The migration history of the Nazca Ridge - a re-evaluation 9
 - 2.3.1 Lateral migration velocity 10
 - 2.3.2 Original length of the Nazca Ridge and onset of ridge subduction 14
 - 2.3.3 Discussion of the new model and geological implications for Peru 16
 - 2.3.4 Conclusions 21

3 Geophysical data acquisition, processing and interpretation 23

- 3.1 Data acquisition and processing 24
- 3.2 Data interpretation 30
 - 3.2.1 The Nazca Ridge 30
 - 3.2.2 The structure of the collision zone 35
- 3.3 Discussion 37
 - 3.3.1 The Nazca Ridge 37
 - 3.3.2 Tectonic erosion at the collision zone 38
- 3.4 Conclusions 43

4 Analogue and numerical modelling of ridge subduction 45

- 4.1 Analogue modelling 46
 - 4.1.1 The critical taper theory and its application to sandbox models 46
 - 4.1.2 The physical properties of the analogue material 49
 - 4.1.3 Monitoring of the 3D sandbox experiments by the PIV system 53
 - 4.1.4 Set-up and concept of the 3D sandbox experiments 55
 - 4.1.5 Simulating ridge subduction at an erosive margin 57
 - 4.1.6 Discussion 69
 - 4.1.7 Conclusions of the analogue modelling 75
- 4.2 Numerical modelling 76
 - 4.2.1 Principles of numerical modelling and application to subduction zones 76
 - 4.2.2 Principles of the Finite-Element method and realization in ABAQUS 77
 - 4.2.3 Isostatic uplift of the Peruvian forearc caused by the Nazca Ridge 79
 - 4.2.4 Deformation of the upper plate caused by oblique ridge subduction 85
 - 4.2.5 Discussion 89
 - 4.2.6 Conclusions of the numerical modelling 92

5 Conclusions 93

6 References 95

7 Acknowledgements 109

Curriculum Vitae

Abstract

The history of the oblique subduction of the Nazca Ridge at the Peruvian active margin and the present collision zone have been investigated by a multidisciplinary approach including plate reconstructions, geophysical data of RV Sonne cruise SO146-GEOPECO, 3D sandbox experiments and Finite-Element modelling. The 1.5 km high Nazca Ridge, composed of 17 km thick igneous crust with seismic velocities similar to normal oceanic crust, but a considerably thicker gabbroic Layer 3, began to subduct beneath Peru ~11.2 Ma ago at ~11°S. Its oblique orientation to the convergence direction of the Nazca Plate results in a southward motion along the Peruvian forearc. The deceleration of the Nazca Plate reduced the lateral migration velocity of the ridge since the onset of its subduction from ~75 mm/a to ~43 mm/a. The ridge did not affect the forearc north of 10°S. It passed the region at 11.5°S off Lima ~9.5 Ma ago. Support for this migration history is provided by the sedimentological and paleo-bathymetric record in ODP Leg 112 cores at 9°S and 11.5°S. A snapshot of the present collision zone at 15°S provided by the geophysical data reveals a thin incoming sediment layer, a large taper of the frontal wedge, presumable shelf sediments near the trench, and erosional features and extension in the continental slope and shelf. An accretionary prism is absent, instead, rocks of high seismic velocities and densities are present close to the trench, which are interpreted as continental basement. The presence of these mechanically strong rocks may explain why the ridge does not deeply indent the lower slope. A causal relation between these two observations has also been recognized in the 3D sandbox experiments. This suite of indications argues for a tectonic erosive regime at the South Peruvian forearc. This mass transfer mode is inferred to be a superposition of enhanced short-term, ridge-induced erosion onto a long-term erosive regime. The latter is inferred from a comparison with the Central Peruvian and North Chilean margins currently not affected by ridge subduction. Numerical modelling showed that the thick crust of the ridge induces buoyancy forces leading to 0.9-1.5 km uplift depending on whether the forearc was subaerial or submarine prior to ridge passage, respectively. In South Peru, uplift of this magnitude is evident from a decrease in water depth above the continental slope, a westward shift of the coastline with formation of marine terraces arched above the ridge, and the presence of marine Cenozoic strata in the Coastal Cordillera. Analogue modelling of the temporal evolution of the forearc shows that the ridge initially pushes the lower part of the wedge up- and sideward, in the direction of its lateral motion. The maximum amount of uplift occurring above the ridge crest is controlled by the height of the ridge and the mechanical strength of the wedge. Later, the ridge uplifts higher parts of the wedge, accompanied by over-steepening and failure of the slope. The location of the maximum uplift shifts towards the leading ridge flank. Above the trailing edge of the ridge, the material subsides again. Both, analogue and numerical modelling show that horizontal extension occurs in the upper plate above the ridge. The modelled sequence of uplift and subsidence and the stress field of the forearc are in excellent agreement with the history of the marine terraces and the stress field inferred from Quaternary normal faults in South Peru. A comparison with accretive margins and analogue models underlines that the style of forearc deformation induced by ridge collision depends on its crustal structure and mechanical strength that, in turn, are influenced by the evolution of the mass transfer regime.

Zusammenfassung

Die Geschichte der schiefen Subduktion des Nazca-Rückens am peruanischen Kontinentalrand und seine heutige Kollisionszone wurden mit einem multidisziplinären Ansatz anhand von Plattenrekonstruktionen, geophysikalischen Daten der FS Sonne-Fahrt SO146-GEOPECO, 3D-Sandkastenexperimenten und Finite-Elemente-Modellierungen untersucht. Der 1.5 km hohe Nazca-Rücken, dessen 17 km mächtige Kruste seismische Geschwindigkeiten ähnlich normaler ozeanischer Kruste, aber eine mächtigere Gabbro-Schicht aufweist, begann vor ~11.2 Ma bei 11°S vor Peru zu subduzieren. Aufgrund seiner schiefen Orientierung zur Konvergenzrichtung der Nazca-Platte wandert der Rücken südwärts am Forearc entlang. Die Verlangsamung der Nazca-Platte reduzierte die laterale Migrationsgeschwindigkeit des Nazca-Rückens seit Beginn seiner Subduktion von ~75 mm/a auf ~43 mm/a. Der Rücken hatte keinen Einfluss auf den Forearc nördlich von 10°S; die Region um 11.5°S bei Lima passierte er vor 9.5°S. Das Modell wird von der Sedimentfazies und Foraminiferenstratigraphie in ODP-Leg 112-Bohrkernen bestätigt. Eine Momentaufnahme der rezenten Kollisionszone bei 15°S mittels geophysikalischer Daten zeigt eine geringmächtige Sedimentschicht auf dem Rücken, einen grossen Öffnungswinkel des frontalen Keils, Schelfsedimente in der Nähe des Tiefseegrabens sowie erosions- und extensionsinduzierte Strukturen im Kontinenthang und -schelf. Ein Akkretionskeil fehlt; hingegen befinden sich als kontinentales Basement interpretierte Gesteine hoher seismischer Geschwindigkeit und Dichte nahe des Tiefseegrabens. Das Vorkommen dieser mechanisch festen Gesteine erklärt, warum der Nazca-Rücken keine Einbuchtung des Forearcs verursacht. Eine kausale Beziehung zwischen diesen beiden Beobachtungen zeigte sich auch in den Analogmodellen. Diese Reihe von Indikatoren deutet auf ein tektonisch erosives Regime in Südperu hin. Dieser Massentransfermodus stellt wahrscheinlich eine Überlagerung von kurzzeitig verstärkter, kollisionsinduzierter und langfristig anhaltender tektonischer Erosion dar, wie ein Vergleich mit den zentralperuanischen und nordchilenischen Kontinentalrändern sowie den Sandkastenmodellen belegt. Numerische Modelle zeigen, dass der Rücken Hebung des Forearcs um 0.9-1.5 km induziert, abhängig davon, ob der Forearc vor der Kollision subaerisch oder submarin war. In Südperu werden solche Hebungsbeträge durch die Abnahme der Wassertiefe über dem Kontinenthang, die Verschiebung der Küstenlinie über dem Rücken nach Westen mit Bildung mariner Terrassen und das Vorkommen mariner, känozoischer Sedimente in der Küstenkordillere belegt. Analogmodellierungen zur zeitlichen Entwicklung des Forearcs während der Kollision zeigen, dass der Rücken das Keilmaterial nach oben und gleichzeitig zur Seite in die Richtung seiner lateralen Migration drückt. Das Hebungsmaximum liegt über dem Rückenkamm und wird von der Höhe des Rückens und der mechanischen Festigkeit des Keilmaterials kontrolliert. In späteren Kollisionsstadien verschiebt sich das Hebungsmaximum zur Rückenflanke. Die Hebung der oberen Bereiche des Keils werden von Übersteilung und Versagen des Hanges begleitet. Analoge und numerische Modelle deuten auf horizontale Extension im Forearc hin. Diese Ergebnisse der Modelle stimmen gut mit Befunden in Südperu überein. Ein Vergleich mit akkretiven Kontinentalrändern und Analogmodellen unterstreicht, dass die kollisionsinduzierte Deformation des Forearcs von der Art der Krustengesteine und ihrer Festigkeit abhängt, die wiederum durch die langfristige Entwicklung des Massentransfermodus kontrolliert werden.

1 Introduction

At convergent plate boundaries, where oceanic plates subduct beneath another oceanic plate or a continent (Figure 1.1), most of the Earth's seismic energy release and explosive volcanism occur. Therefore, active margins have a high geo-hazard risk, since their coastal plains and natural resources make them especially attractive for human settlements. Against this background, intense research has been carried out over the past decades in order to learn about the various dynamic processes shaping convergent margins [overviews e.g. by *Bebout et al.*, 1996; *Kearey and Vine*, 1996; *Turcotte and Schubert*, 2002].

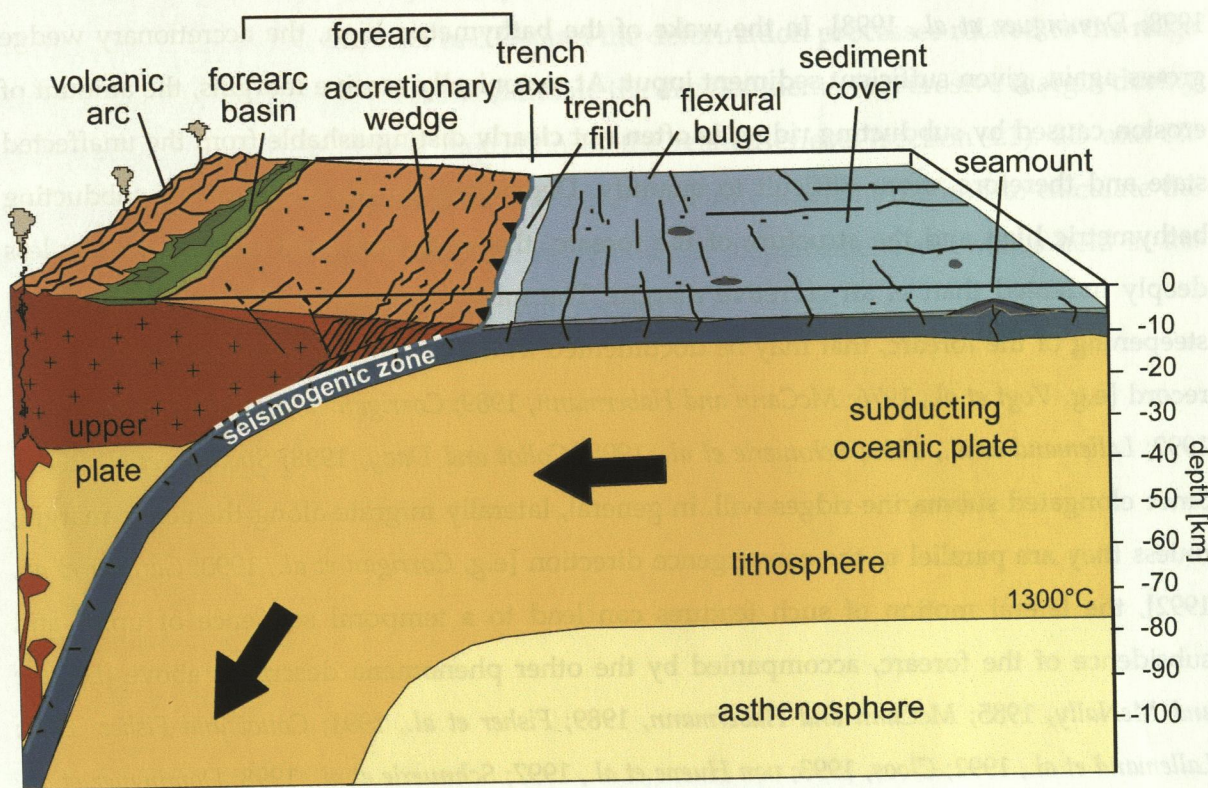


Figure 1.1: Schematic cross-section of a subduction zone.

An important role for the subduction processes plays the nature of the descending oceanic plate. Type and thickness of the sedimentary cover, age surface, and internal structure of the oceanic crust strongly influence the frontal part of the subduction zone, the forearc, the plate interface, and the generation of magmas and thus, the volcanic arc at greater depth [*Jarrard*, 1986]. At the forearc, the input from the oceanic plate is among the main factors governing the mass transfer mode at the frontal wedge [e.g. *Karig and Sharman*, 1975; *Scholl et al.*, 1980; *Hilde*, 1983; *Cloos and Shreve*, 1988; *von Huene and Scholl*, 1991]. The mass transfer regime may vary between two endmember modes, i.e. the complete offscraping of sediments from the

descending plate and their accretion to the upper plate or, if little sediment input is available, the tectonic removal and subduction of material of the upper plate, termed subduction erosion [e.g. *Karig, 1975; Scholl et al., 1980; Hilde, 1983; Cloos and Shreve, 1988; von Huene and Scholl, 1991*].

Seamount chains, submarine ridges and other bathymetric highs on the oceanic plate entering the subduction zone may affect the sedimentological and tectonic evolution of the forearc system significantly. The specific style of deformation depends on the mass transfer regime of the margin. At accretive margins, subducting bathymetric highs cause, in general, large indentation and partial removal of the accretionary prism and reduce the input of sediments from the oceanic plate [*Chung and Kanamori, 1978; Bouysse and Westercamp, 1990; McCann and Habermann, 1989; Lallemand et al., 1994; von Huene et al., 1997; Schnuerle et al., 1998; Dominguez et al., 1998*]. In the wake of the bathymetric high, the accretionary wedge grows again, given sufficient sediment input. At tectonically erosive margins, the amount of erosion caused by subducting ridges is often not clearly distinguishable from the unaffected state and therefore, more difficult to quantify. Depending on the shape of the subducting bathymetric high and the structure of the forearc, the slope and shelf regions may be less deeply indented than at an accretive margin. The most pronounced effects are uplift and steepening of the forearc, that may be documented in the off- and onshore sedimentological record [e.g. *Vogt et al., 1976; McCann and Habermann, 1989; Corrigan et al., 1990; Gardner et al., 1992; Lallemand et al., 1992; Schnuerle et al., 1998; Collot and Davy, 1998; Spikings et al., 2001*]. Since elongated submarine ridges will, in general, laterally migrate along the active margin, unless they are parallel to the convergence direction [e.g. *Corrigan et al., 1990; Gardner et al., 1992*], the lateral motion of such features can lead to a temporal sequence of uplift and subsidence of the forearc, accompanied by the other phenomena described above [*LeFevre and McNally, 1985; McCann and Habermann, 1989; Fisher et al., 1991; Collot and Fisher, 1991; Lallemand et al., 1992; Cloos, 1993; von Huene et al., 1997; Schnuerle et al., 1998; Dominguez et al., 1998*].

A quantification of the effects of ridge subduction benefits from settings, in which regions influenced by ridge subduction can be compared to unaffected areas. Such a favourable setting is provided at the Peruvian active margin, along which the Nazca Ridge migrates southward [*Pilger, 1981; Cande, 1985; von Huene and Lallemand, 1990; von Huene et al., 1996*]. Morphologic features associated with past interaction of the ridge and forearc are located north of the collision zone, however, the ridge did not pass the margin north of 10°S, as constrained by plate reconstructions [*Hampel, 2002*]. The regions north and south of 10°S share similar geodynamic boundary conditions, but for reasons not yet fully understood differ in the sedimentological records of their forearc systems, which imply different tectonic

histories [Kulm *et al.*, 1981; Suess, von Huene *et al.*, 1988; Suess, von Huene *et al.*, 1990; von Huene *et al.*, 1988; von Huene and Lallemand, 1990].

The goal of this thesis is to reconstruct the motion of the Nazca Ridge in the past and to investigate the impact of the ridge on the South Peruvian forearc. Chapter 2 introduces the geodynamic setting of Peru with a focus on the collision zone of the Nazca Ridge and the South Peruvian margin and presents a new reconstruction of the migration history of the Nazca Ridge [Hampel, 2002]. Chapter 3 presents multibeam bathymetric, wide-angle and reflection seismic data collected at the collision zone during cruise SO146-GEOPECO of the German Research Vessel "Sonne" [Bialas and Kukowski, 2000]. The new data provide insights into the topography, geometry and crustal structure of the Nazca Ridge and its intersection with the Peruvian margin. Chapter 4 presents two complementary modelling approaches that have been employed to better understand the deformation processes related to the ridge subduction. 3D analogue experiments simulate the development of an erosive margin during ridge subduction and the lateral migration of the related effects (section 4.1). 2D and 3D numerical modelling has been carried out using the Finite-Element method to calculate the isostatic uplift of the forearc due to the ridge and the displacement and stress field in the upper plate during the passage of the ridge (section 4.2).

2 The Peruvian active margin - geodynamic setting and a new model for the subduction history of the Nazca Ridge

At the Peruvian convergent margin, the oceanic Nazca Plate subducts obliquely beneath the South American continent at a convergence rate of ~ 68 mm/a [Norabuena *et al.*, 1998] (Figure 2.1). Since the Miocene, the tectonic evolution of the Peruvian forearc has been strongly influenced by the collision of the Nazca Ridge. As the ridge has an oblique orientation with respect to the convergence direction of the Nazca Plate, it migrates southward parallel to the plate boundary (Figure 2.1). As a consequence, the Peruvian forearc displays, from south to north, different stages of its tectonic evolution during and after ridge passage.

In regard of the mass transfer mode, the margin was early classified as tectonically erosive north of $\sim 11.5^\circ\text{S}$ [Scholl *et al.*, 1970; Rutland, 1971]. Much of today's knowledge about the Peruvian forearc is derived from results of the Nazca Plate Project [Kulm *et al.*, 1981] and data acquired prior to and during Leg 112 of the Ocean Drilling Program (Figure 2.1) [Suess, von Huene *et al.*, 1988; Suess, von Huene *et al.*, 1990]. However, only few drilling or seismic data is available at 15°S , where the Nazca Ridge collides with the Peruvian forearc [Kulm *et al.*, 1974], or south of the collision zone [Coulburn *et al.*, 1981]. The southernmost sites of ODP Leg 112, which only drilled Late Pliocene strata, were located at $\sim 13.5^\circ\text{S}$, while the recent Leg 202 drilled two sites on the Nazca Ridge, but not the forearc [Shipboard Scientific Party of Leg 202, 2002].

Based on these studies, long-term tectonic erosion off North and Central Peru since at least the Middle Miocene was inferred by rapid subsidence of the forearc and an eastward shift of the trench and the magmatic arc [Hussong *et al.*, 1981; Kulm *et al.*, 1988; von Huene and Lallemand, 1990]. Between at 15°S and 11.5°S , an active accretive regime was proposed to have established after the passage of the Nazca Ridge [von Huene and Lallemand, 1990; von Huene *et al.*, 1996]. Recent studies, however, advocate an erosive regime also for the central and southern Peruvian margin since the Eocene [Clift *et al.*, in press; Kukowski *et al.*, in prep.].

In the following sections 2.1 and 2.2, the characteristics of the Nazca Ridge and the collision zone in South Peru will be described. Section 2.3 introduces a new reconstruction of the migration history of the Nazca Ridge [Hampel, 2002].

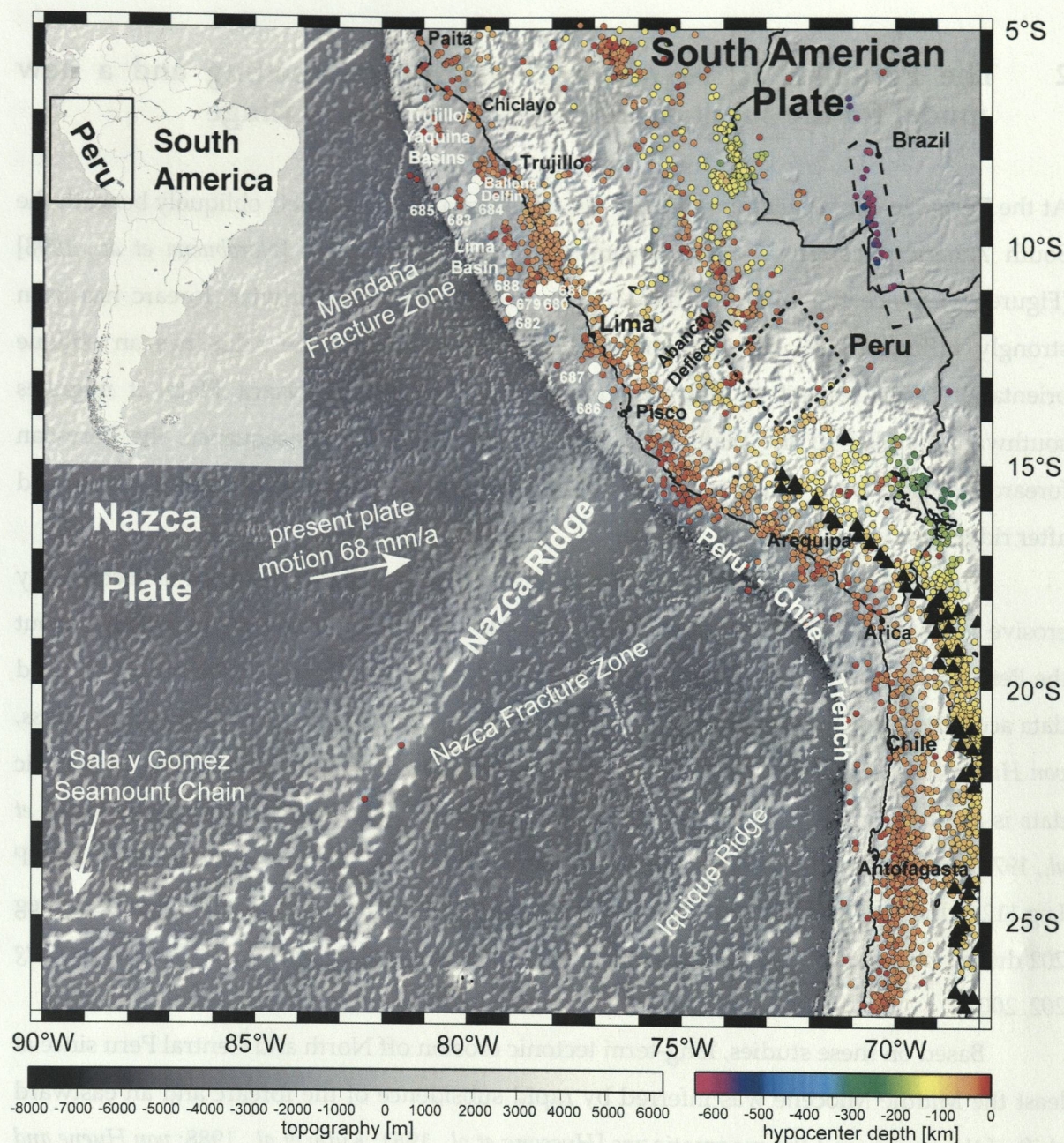


Figure 2.1: Topographic map [Smith and Sandwell, 1997a] of the Nazca Ridge and the South American margin. Coloured circles represent earthquakes recorded from 1973-2002 [US Geological Survey-National Earthquake Information Center]. Note the gap in the intermediate depth seismicity (70-300 km) (dotted line) and the presence of deep seismic events (500-650 km) beneath Brazil (dashed line). Active volcanic centres are marked by black triangles [from the Smithsonian Global Volcanism Program]. Locations of ODP leg 112 sites and two industrial wells (Ballena, Delfin) are indicated by white circles.

2.1 The Nazca Ridge

The 200 km wide submarine Nazca Ridge extends more than 1100 km in the Southeast Pacific with a linear trend of N42°E (Figure 2.1). The crest of the ridge rises 1500 m above the surrounding seafloor and is located above the carbonate compensation depth. The flanks of the ridge dip gently at 1-2° [Hagen and Moberly, 1994]. The crust of the ridge is at least twice

as thick as the crust of the adjacent Nazca Plate, resulting from a thick lower crustal layer, as revealed by gravity data [Couch and Whitsett, 1981]. The free-air anomaly contours do not coincide with the bathymetric contours that mark the outline of the Nazca Ridge (Figure 2.2) [Couch and Whitsett, 1981]. The average crustal thickness of the ridge along its entire length derived from the analysis of Rayleigh waves is 18 ± 3 km [Woods and Okal, 1994].

The Nazca Ridge formed at the Pacific-Farallon/Nazca spreading center in the early Cenozoic [Pilger and Handschumacher, 1981; Pilger, 1981; Woods and Okal, 1994] and has common origin with the Tuamotu Plateau, which represents its conjugate feature on the Pacific Plate [Pilger, 1981] and is located 2000 km west of the East Pacific Rise between 10°S and 20°S today.

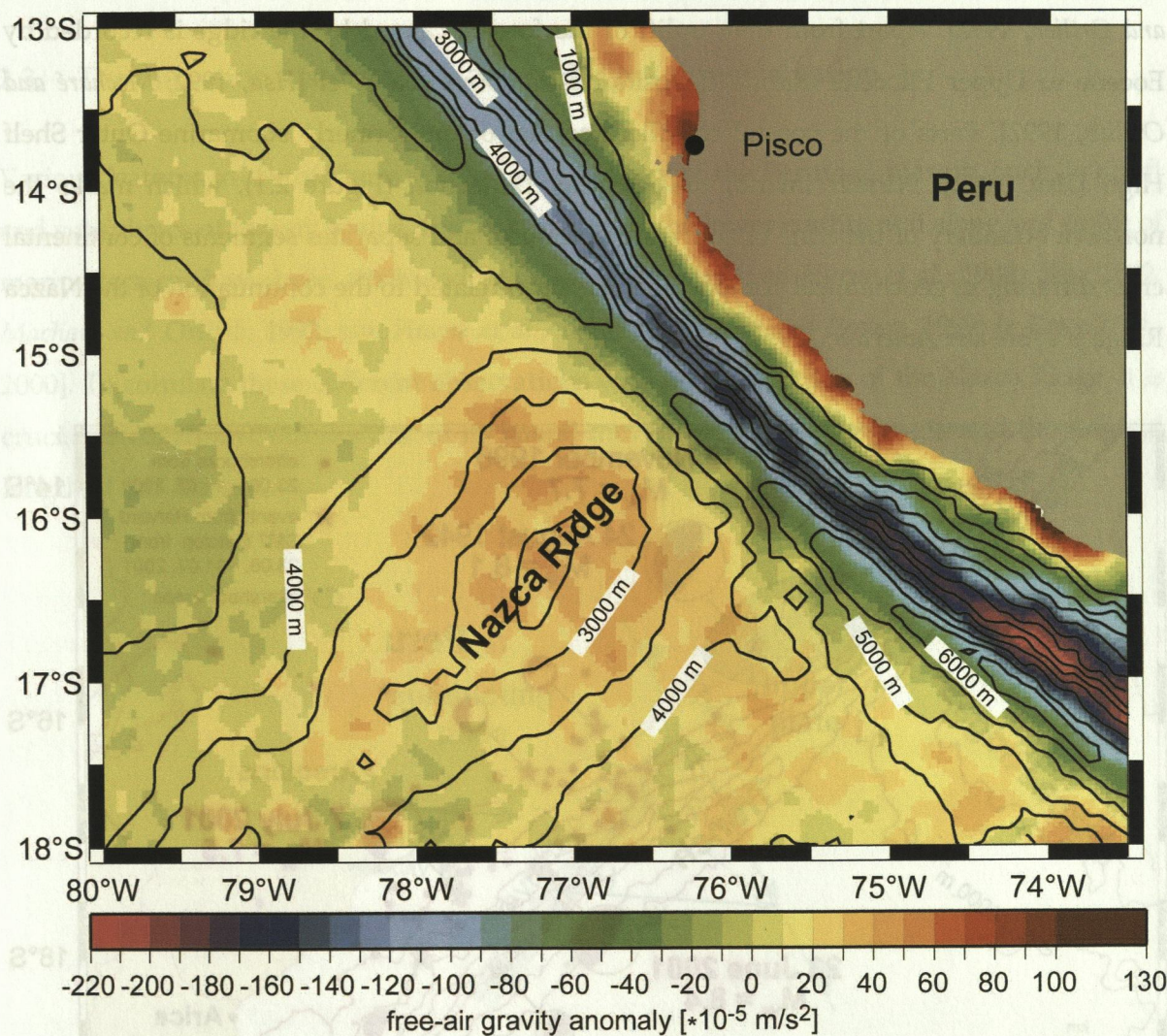


Figure 2.2: Free-air gravity anomaly of the Nazca Ridge and the adjacent Nazca Plate overlain by bathymetry contours [Smith and Sandwell, 1997a, b]. Note that the topography of the ridge does not coincide with the free-air anomaly contours [Couch and Whitsett, 1981].

2.2 The collision zone of the Nazca Ridge and the Peruvian margin

Where the ridge descends beneath the South American Plate, the trench does not show a pronounced deviation from its linear trend, but the water depth along the trench line shoals from 6500 m south of the ridge to 5000 m at the ridge crest. In bathymetry and side-scan sonar images, features indicating ongoing surface erosion and faulting have been identified on the continental slope [Hussong *et al.*, 1988; Hagen and Moberly, 1994; Li and Clark, 1994]. Landwards, the recent collision zone is expressed by a narrowing of the shelf, a westward shift of the coastline and the presence of raised marine terraces at the coast between 13.5°S and 15.6°S [Hsu, 1992; Macharé and Ortlieb, 1992]. Above the northern flank of the subducted ridge, the recent subsidence of the marine terraces, which had been uplifted earlier by the ridge until the passage of its crest, illustrates its southward movement [Hsu, 1992; Macharé and Ortlieb, 1992]. Apart from that, uplift of the forearc caused by the ridge is recorded by Eocene to Upper Pliocene marine deposits raised above sea level [Hsu, 1992; Macharé and Ortlieb, 1992]. Parts of the coastal cordillera consist of the formerly submarine Outer Shelf High [Hsu, 1992]. Further inland, the Abancay Deflection (Figure 2.1), which marks the northern boundary of the zone of active arc volcanism and separates segments of continental crust differing in geochemical composition, has been related to the continuation of the Nazca Ridge [Petford and Atherton, 1995].

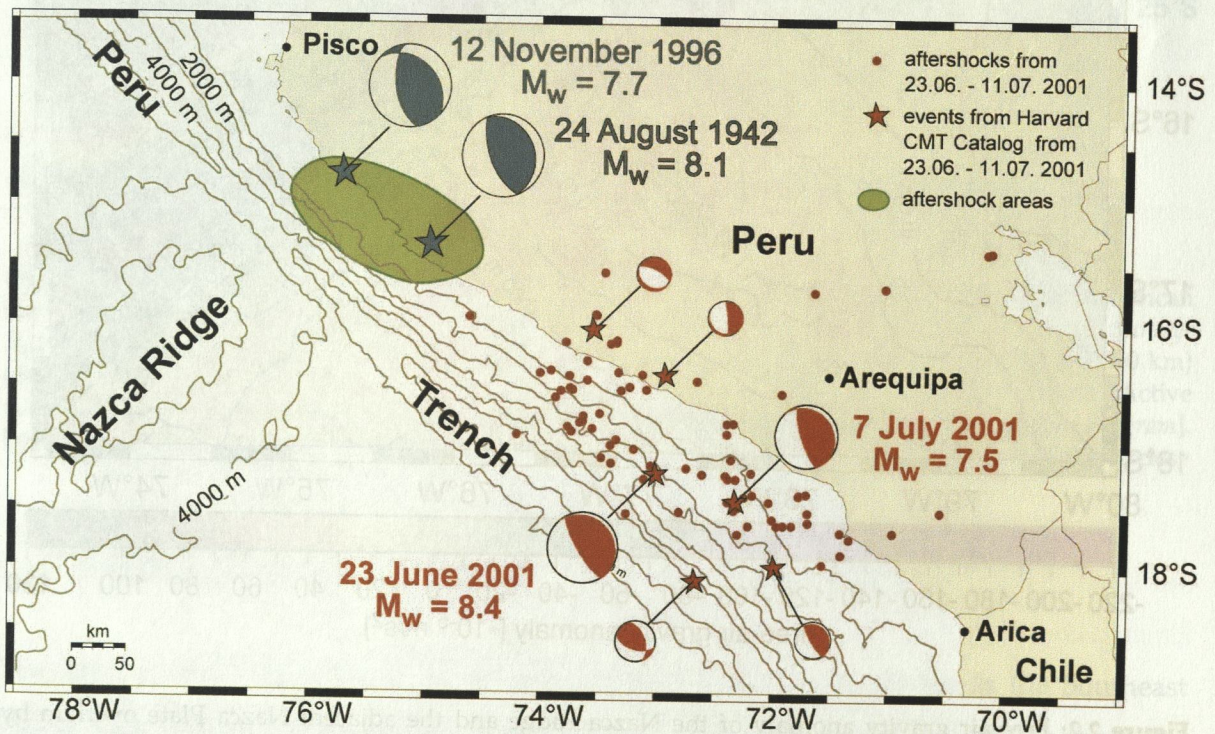


Figure 2.3: Recent earthquakes in the Nazca Ridge region.

In the presumable continuation of the Nazca Ridge, three of the several strong earthquakes that ruptured Peru in the last decades occurred [Swenson and Beck, 1999] (Figure 2.3). The earthquakes in 1942 and 1996 with magnitudes $M_W = 8.1$ and $M_W = 7.7$, respectively, were located above the subducted crest and southeastern flank of the ridge. In 2001, another earthquake with a magnitude of $M_W = 8.4$ and several aftershocks of magnitude $M_W = 6.0$ and larger ruptured the coastal area at the southern edge of the subducted ridge. The downward continuation of the ridge has been related to a zone of reduced intermediate depth seismicity and to the southern boundary of the low-angle subduction segment beneath Southern Peru [Barazangi and Isacks, 1976; Hasegawa and Sacks, 1981; Pilger, 1981], which coincides with the terminus of the Quaternary volcanic arc [Nur and Ben-Avraham, 1981; McGeary et al., 1985; Gutscher et al., 2000].

2.3 The migration history of the Nazca Ridge - a re-evaluation

Various features in the offshore and onshore geology of the Peruvian margin, such as uplift and subsidence of forearc basins, tectonic erosion of the lower continental slope and uplift of marine terraces have been attributed to ridge subduction [von Huene et al., 1988; Hsu, 1992; Macharé and Ortlieb, 1992; von Huene et al., 1996; von Huene and Pecher, 1999; le Roux et al., 2000]. To correlate these different observations with the subduction of the Nazca Ridge, it is crucial to constrain both the rate of its lateral movement along the margin and the original length of this feature.

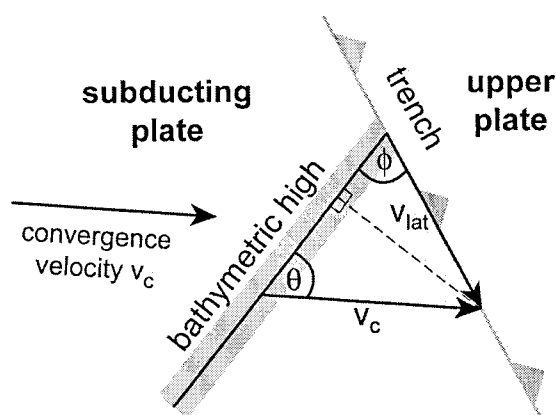


Figure 2.4: Geometric relations between the lateral migration velocity v_{lat} of a bathymetric high parallel to an active plate boundary, the plate convergence velocity v_c , and the orientation of the bathymetric high relative to convergence direction and trench [Geist et al., 1993].

The velocity at which a bathymetric high moves along an active margin is controlled by three parameters: the convergence velocity v_c and the two angles θ and ϕ , defined by the orientation of the bathymetric high relative to convergence direction and trench, respectively (Figure 2.4). The lateral velocity v_{lat} of a bathymetric high parallel to the plate boundary is then:

$$v_{lat} = \frac{v_c \sin \theta}{\sin \phi}$$

Even if the convergence velocity is constant, a curvature of the trench line, i.e. a variable angle ϕ , would result in a variable lateral migration velocity.

Regarding the temporal evolution of the collision between the Nazca Ridge and the Peruvian margin, current models differ in the lateral migration velocities, in the ages of ridge passage assigned to different latitudes and in the predicted length of the original Nazca Ridge. The following reconstructions cover the migration history of the Nazca Ridge along the entire Peruvian margin: *Pilger* [1981; his Figure 4] shows that the ridge first came in contact with the Peruvian trench at 5°S in the Middle Miocene and later passed 10°S at ~9 Ma. Other studies [*von Huene et al.*, 1988; *von Huene and Lallemand*, 1990; *von Huene et al.*, 1996], based on plate reconstructions [*Cande*, 1985] and the NUVEL-1A convergence rate [*DeMets et al.*, 1990], inferred that the Nazca Ridge began to subduct 8 Ma ago at 8°S and was located at 9°S and 11.5°S at 6-7 Ma and 4-5 Ma, respectively. Three other reconstructions concentrate on the migration of the ridge from the end of the Miocene to the present: Based on the plate motion data by *Pardo-Casas and Molnar* [1987], *Hsu* [1992] infers a lateral migration velocity of ~71 mm/a. *Macharé and Ortlieb* [1992] use the plate motion data by *Pardo-Casas and Molnar* [1987] to deduce a passage of the ridge crest at 13°S at 4 Ma, i.e. a lateral velocity of ~64 mm/a. *Le Roux et al.* [2000] suggest that the ridge crest was located at ~13.5°S at 5.3 Ma and thus, off Lima (12°S) before the end of the Miocene, i.e. laterally moving at a velocity of ~42 mm/a derived from convergence rates given by *Stein et al.* [1986]. These differences in the inferred migration rates of the Nazca Ridge underline the importance of the re-evaluation presented here.

2.3.1 Lateral migration velocity

Unravelling the migration history of subducting ridges, seamount chains and other submarine bathymetric highs requires knowledge of past plate motions, which can be obtained by two types of data sets. Plate motions averaged over the last 3 Ma are provided by the NUVEL-1A model, based on evaluation of spreading rates, transform fault azimuths

and earthquake slip vectors [DeMets *et al.*, 1990]. On longer time-scales, paleo-plate positions and motions can be reconstructed by analysing the magnetic anomalies of the oceanic crust. This method yields average velocity vectors for different time intervals (e.g. [Cande, 1985; Mayes *et al.*, 1990]).

This study uses updated Nazca (Farallon)-South American relative motions [Somoza, 1998], which take into account a revision of the global geomagnetic time scale [Cande and Kent, 1995]. This data set provides constant convergence velocities and directions for different time intervals for the last 40 Ma at different latitudes, of which the values given at 12°S are applied (Table 2.1). The convergence rate of 75 mm/a for the last 5 Ma [Somoza, 1998] agrees well with the NUVEL-1A prediction [DeMets *et al.*, 1990]. Both estimates are higher than the current convergence rate determined by space-geodetic measurements, i.e. 61 ± 3 mm/a at 12°S [Norabuena *et al.*, 1999; Angermann *et al.*, 1999]. Since the convergence rate may be slowing with time, the space-geodetic values are less relevant for this reconstruction.

Table 2.1: Relative plate motion between Nazca and South American Plates at 12°S [Somoza, 1998].

time interval [Ma]	convergence velocity ^a [km/Ma]	convergence direction	length of displacement vector [km]	age uncertainty [Ma]
0-4.9 (chron 0-3)	75 ± 4	77°	368 ± 20	± 0.3
4.9-10.8 (chron 3-5)	106 ± 11	82°	625 ± 65	± 0.6
10.8-16 (chron 5-5C)	123 ± 18	84°	640 ± 94	± 0.8

^a Errors are assumed to be 5%, 10% and 15% for the latest, intermediate, and earliest time interval, respectively.

Using the average convergence velocities and directions for the three latest time intervals, three displacement vectors and respective paleo-positions of the Nazca Ridge relative to a fixed South American Plate are constructed (Table 2.1, Figure 2.5a). The resulting time path allows to determine when the ridge crest passed a specific point on the trench line assuming a linear continuation of the ridge towards the trench, as suggested by the shape of the present ridge, and a paleo-trench position similar to the present trench line [Pilger, 1981; Cande, 1985; von Huene and Lallemand, 1990; Hsu, 1992; Macharé and Ortlieb, 1992; von Huene *et al.*, 1996; le Roux *et al.*, 2000] (Figure 2.5b).

Uncertainties in the convergence velocities are not specified [Somoza, 1998], but may be of the order of 10% [Norabuena *et al.*, 1999]. Since the errors are likely to be smaller in the latest time interval, as suggested by the errors of the NUVEL-1A convergence rates [DeMets *et al.*, 1990], and may be larger in the earliest time interval, this study assigns uncertainties of 5%, 10% and 15% to the convergence velocities of the 0-4.9 Ma, 4.9-10.8 Ma and 10.8-16 Ma

time intervals, respectively (Table 2.1). Using these error limits, the uncertainties in the ages of ridge passage with respect to the convergence rates of the three time intervals are given in Table 2.1. Potential errors of the geomagnetic timescale and of the convergence azimuths for the different time intervals have not been taken into account.

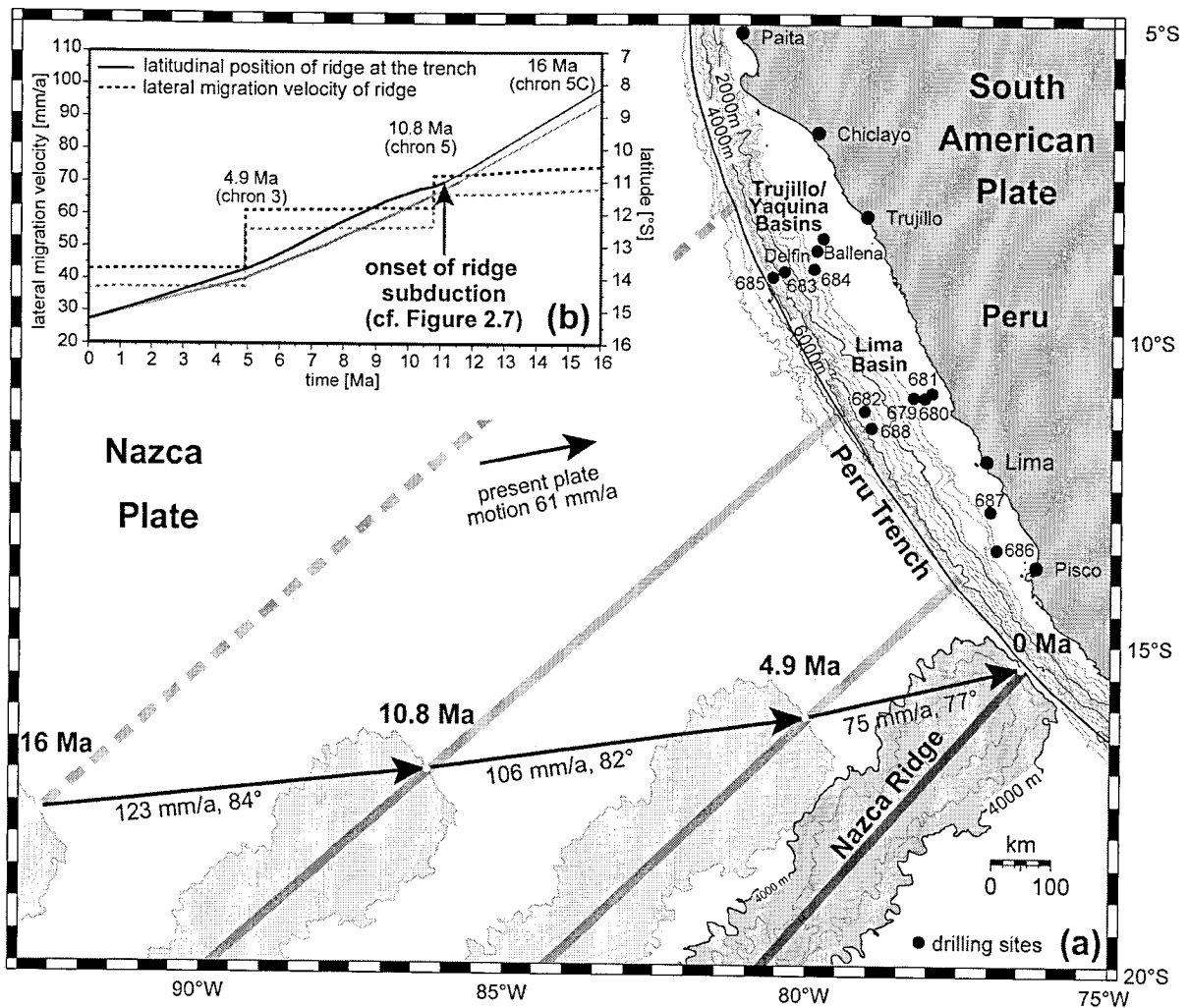


Figure 2.5: (a) Three paleo-positions of the Nazca Ridge and displacement vectors for the present intersection point of ridge and trench. Grey lines represent the assumed linear continuation of the ridge. Inset (b) shows diagram in which the latitudinal position of the linearly continuing ridge crest on the trench line and the migration velocity of the ridge parallel to the plate boundary are plotted versus time. The two black lines are derived by using the relative plate motion data as given in [Somoza, 1998]. The black arrow marks the onset of ridge subduction inferred by this study (section 2.3.2). The two grey lines refer to a scenario in which a small amount of intra-plate deformation (10 mm/a) accommodated in the Peruvian Andes is subtracted from the convergence rates of [Somoza, 1998].

An implicit assumption of this reconstruction is that the decreasing relative convergence rate between the Nazca Plate and stable South America over the last 15–20 Ma, as derived from plate reconstructions, equals the amount of relative motion between the Nazca Plate and the Peruvian forearc. This assumption has also been the basis for all previous reconstructions of

the Nazca Ridge motion [Pilger, 1981; Cande, 1985; von Huene et al., 1988; von Huene and Lallemand, 1990; Hsu, 1992; Macharé and Ortlieb, 1992; von Huene et al., 1996; le Roux et al., 2000]. However, the presence of the Andean mountain belt east of the forearc demonstrates that, strictly speaking, this assumption is not correct, since some of the relative plate motion is taken up by intra-plate deformation within the South American Plate. Obviously, this intra-plate deformation tends to reduce the relative motion between the Nazca Ridge and the Peruvian forearc system. At present, a rigorous assessment of the amount and the direction of shortening accommodated in the Peruvian Andes is difficult due to the lack of sufficient geological data. Nevertheless, space-geodetic measurements [Norabuena et al., 1999] and geological profiles [Koch, 1962; Sébrier et al., 1988; Kley and Monaldi, 1998; and references therein] across the Andes can be used to estimate the present-day and past shortening rates across the Eastern Cordillera and the Subandean belt [Hindle et al., 2002]. These data show that geologic and space-geodetic displacement rates are generally consistent and that directions of shortening in the Eastern Andes are approximately parallel to the Nazca-South America convergence vector. The data have been interpreted in terms of a two-stage model with rates of shortening across the Eastern Andes of 5-8 mm/a for the last 25-10 Ma and of 10-15 mm/a for the last 10 Ma [Hindle et al., 2002]. In order to account for the Andean intra-plate deformation, the lateral migration velocity of the Nazca Ridge is also presented for a scenario in which an average Andean shortening rate of 10 mm/a for the last 16 Ma is subtracted from the relative convergence velocity between Nazca and South American Plates (grey lines in Figure 2.5b). Considering the intra-plate deformation tends to slightly increase the ages of ridge passage assigned to specific latitudes, in other words, the lateral migration velocity of the ridge slightly decreases. However, the geological implications of the model (see below) remain valid, even if the intra-plate deformation is taken into account. To allow a straightforward comparison of the model with previous reconstructions of the Nazca Ridge motion, the following discussion uses the model-curve neglecting intra-plate deformation (black lines in Figure 2.5b). Once more detailed information on Andean shortening rates and directions in Peru becomes available, it should be incorporated into the model.

In summary, the first part of the reconstruction demonstrates that the ridge moved significantly slower parallel to the margin than inferred by previous studies [Pilger, 1981; von Cande, 1985; Huene et al., 1988; von Huene and Lallemand, 1990; Hsu, 1992; Macharé and Ortlieb, 1992; von Huene et al., 1996; le Roux et al., 2000]. In particular, a ridge of sufficient length would have passed the ODP Leg 112 sites in the Trujillo/Yaquina Basins (9°S) and Lima Basin (11.5°S) at ~14.5 Ma and at ~9.5 Ma, respectively. Apart from this migration history, deducing the onset of ridge subduction requires estimating the length of the original ridge.

2.3.2 Original length of the Nazca Ridge and onset of ridge subduction

The preservation of oceanic ridges and plateaus in the Southeastern Pacific offers the possibility to constrain the shape of already subducted parts of bathymetric highs on the Nazca Plate by their mirror images on the Pacific Plate (Figure 2.6). As these pairs of conjugate highs have formed simultaneously at the Pacific-Farallon/Nazca spreading center (e.g. [Pilger and Handschumacher, 1981; Cande and Haxby, 1991]) they are thought to have a similar length and shape assuming symmetric spreading [Pilger, 1981; Cande and Haxby, 1991]. The Nazca Ridge has a common origin with the Tuamotu Plateau at the Pacific-Farallon/Nazca spreading center [Pilger, 1981; Pilger and Handschumacher, 1981; Woods and Okal, 1994] and the pre-condition of symmetric spreading seems to be met, since the respective segments of the Nazca and Pacific Plates between chrons 13 to 23 have similar widths (see Figures 2.6, 2.7).

The N70°W trending, elongated Tuamotu Plateau is a composite feature consisting of island chains and oceanic plateaus with volcanic edifices that once were subaerial and today form atolls [Ito et al., 1995], whereas the Nazca Ridge is characterized by smaller, but similar submarine volcanic features [Hagen and Moberly, 1994; Bialas and Kukowski, 2000]. Despite these differences in their topography, both ridges have an overall linear trend. Therefore, the 4000 m water depth contour line of the Tuamotu Plateau has been used to approximate the outline and total length of the original Nazca Ridge [Pilger, 1981; Cande, 1985; von Huene and Lallemand, 1990; von Huene et al., 1996]. To estimate the length of the subducted part of the Nazca Ridge, however, it has to be taken into account that the northwesternmost part of the Tuamotu Plateau formed on 10-20 Ma old oceanic crust of the Pacific Plate, indicating an origin 600 km off the spreading center [Ito et al., 1995]. The hotspot that generated the northwesternmost part of the Tuamotu Plateau [Okal and Cazenave, 1985] most likely had no effect on the Nazca Plate [Ito et al., 1995]. For this reason, the northwestern end of the plateau probably does not have a counterpart on the Nazca Plate. Another assumption made to specify the onset of ridge subduction is the use of the present trench line as the paleo-trench position [Pilger, 1981; Cande, 1985; von Huene and Lallemand, 1990; Hsu, 1992; Macharé and Orthlieb, 1992; von Huene et al., 1996; le Roux et al., 2000].

To estimate the length of the original Nazca Ridge, a mirror image of the Tuamotu Plateau is created using its 4000 m contour line. To find the correct position of the mirror image on the Nazca Ridge, magnetic anomaly lineations of the surrounding sea floor are fitted, using a global data set [Cande et al., 1989; Cande and Haxby, 1991] together with specific data for the Tuamotu Plateau region [Munsch et al., 1996]. Chrons 15-20 are the oldest magnetic anomalies common to the sea floor close to both features (Figure 2.6b).

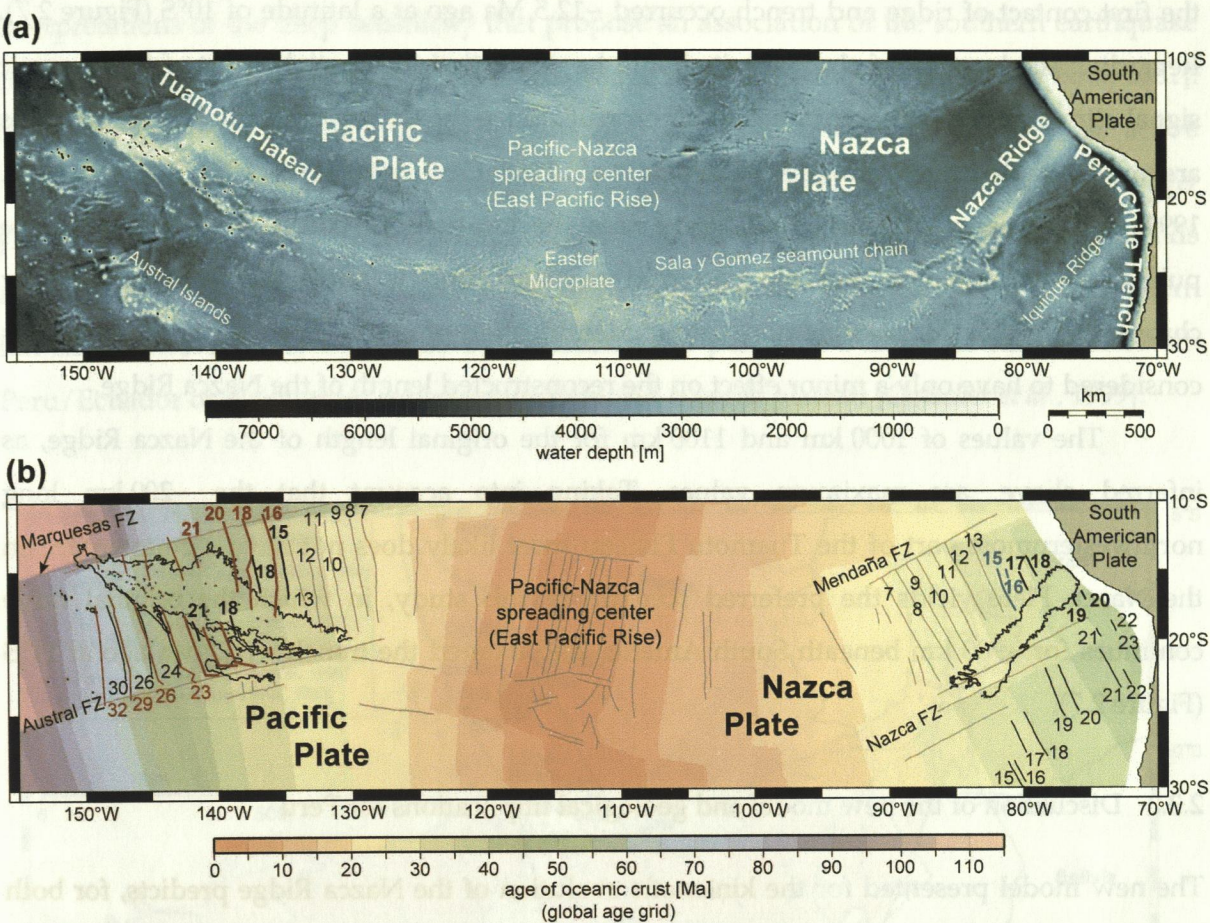


Figure 2.6: (a) Bathymetric map [Smith and Sandwell, 1997a] of the South Pacific showing the Pacific-Nazca spreading center and the conjugate features Nazca Ridge and Tuamotu Plateau. (b) Outlines of the Nazca Ridge and the Tuamotu Plateau are shown by their 4000 m water depth contour lines. The global age grid [Mueller et al., 1997] of the oceanic crust interpolated from magnetic anomalies is shown by colour code. Selected magnetic anomaly lineations are represented by black [Cande et al., 1989], blue [Cande and Haxby, 1991] and red [Munsch et al., 1996] lines.

To fit these chrons north and south of the Tuamotu Plateau to the ones on the Nazca Plate, no scaling of the mirror image is needed, which indicates symmetric sea floor spreading. On the Nazca Plate, the trends of the chrons are better constrained north than south of the ridge and appear to be roughly parallel to each other (Figure 2.6b). In contrast, the same magnetic lineations are at an angle with each other north and south of the Tuamotu Plateau. As a consequence, fitting the chrons leads to two endmember positions (Figure 2.7). Matching chrons 19 and 20, located south of the ridges, with chrons 18-21 being parallel, leads to an abrupt bend of the original Nazca Ridge which results in a N16°W trend and a length of about 1000 km corresponding to an onset of subduction ~10.0 Ma ago at 8.5°S (Figure 2.7). Adjusting chrons 16 and 18, located north of the bathymetric highs, with chrons 15-20 being parallel, leads to the position of the mirror image preferred by this study, because in that case the Nazca Ridge continues linearly beneath South America for 1100 km suggesting that

the first contact of ridge and trench occurred ~12.5 Ma ago at a latitude of 10°S (Figure 2.7). Regarding the location of chron 18, it should be noted that the spatial extent of its magnetic signal allows to pick different phases as chron 18. Since the details of the picking procedures are not available for all publications [Cande *et al.*, 1989; Cande and Haxby, 1991; Munschy *et al.*, 1996; and references therein], this study uses the locations of chron 18 as shown in the published maps. Given that the preferred reconstruction is additionally constrained by chrons 15 and 16, the possible non-unique identification of chron 18 by different authors is considered to have only a minor effect on the reconstructed length of the Nazca Ridge.

The values of 1000 km and 1100 km for the original length of the Nazca Ridge, as inferred above, are maximum values. Taking into account that the ~200 km long northwesternmost part of the Tuamotu Plateau most likely does not have a counterpart on the Nazca Plate yields the preferred scenario of this study, in which the original ridge continues for ~900 km beneath South America and entered the trench ~11.2 Ma ago at 11°S (Figure 2.7).

2.3.3 Discussion of the new model and geological implications for Peru

The new model presented for the kinematic evolution of the Nazca Ridge predicts, for both endmember positions described above (Figure 2.7), a lateral migration history that differs significantly from previous studies [Pilger, 1981; von Cande, 1985; Huene *et al.*, 1988; von Huene and Lallemand, 1990; Hsu, 1992; Macharé and Ortlieb, 1992; von Huene *et al.*, 1996; le Roux *et al.*, 2000]. With respect to the two possible positions of the mirror image of the Tuamotu Plateau, this study prefers fitting the magnetic anomaly lineations 16 and 18 north of the plateau instead of chrons 19 and 20 south of it for the following reasons: First, with this fit, the straight Nazca Ridge continues without a bend. Second, the outline of the northern arm of the Tuamotu Plateau resembles the modern Nazca Ridge, in agreement with their probable alignment during their common origin [Woods and Okal, 1994]. Apart from that, the uncertainties in the direction of the magnetic anomalies 16 and 18 are considerably smaller than those of the shorter chrons 19 and 20, which, like in the Tuamotu Plateau region, might not be parallel to chrons 16 and 18. Different orientations of chrons 18 and 19 are also suggested by the magnetic anomalies of the Nazca Plate south of the Nazca Fracture Zone (Figure 2.6). Another argument is that a linear continuation of the Nazca Ridge coincides well with the zone of reduced intermediate depth seismicity and the southern boundary of the segment of low-angle subduction beneath South Peru (Figures 2.1, 2.7). The predicted northeastern end of the ridge correlates with the cluster of deep seismic events beneath Brazil between ~8.5°S and ~10.5°S (compare Figures 2.1, 2.7). This agrees well with

interpretations of the deep seismicity that propose an association of the southern earthquake cluster with the subducted part of the Nazca Ridge [Okal and Bina, 1994; Okal and Bina, 2001]. Moreover, a ~N42°E trending ridge coincides with the northern boundary of active volcanism and the Abancay Deflection [Petford and Atherton, 1994; Gutscher et al., 2000]. Pilger [1981], however, argued for the position fitted to chron 19, because the ridge then extends farther to the north and thus, can explain the flat slab beneath Northern Peru. This northern flat slab, however, may be caused by the subducted part of the Carnegie Ridge off North Peru/Ecuador or by another, completely subducted oceanic plateau [Gutscher et al., 1999].

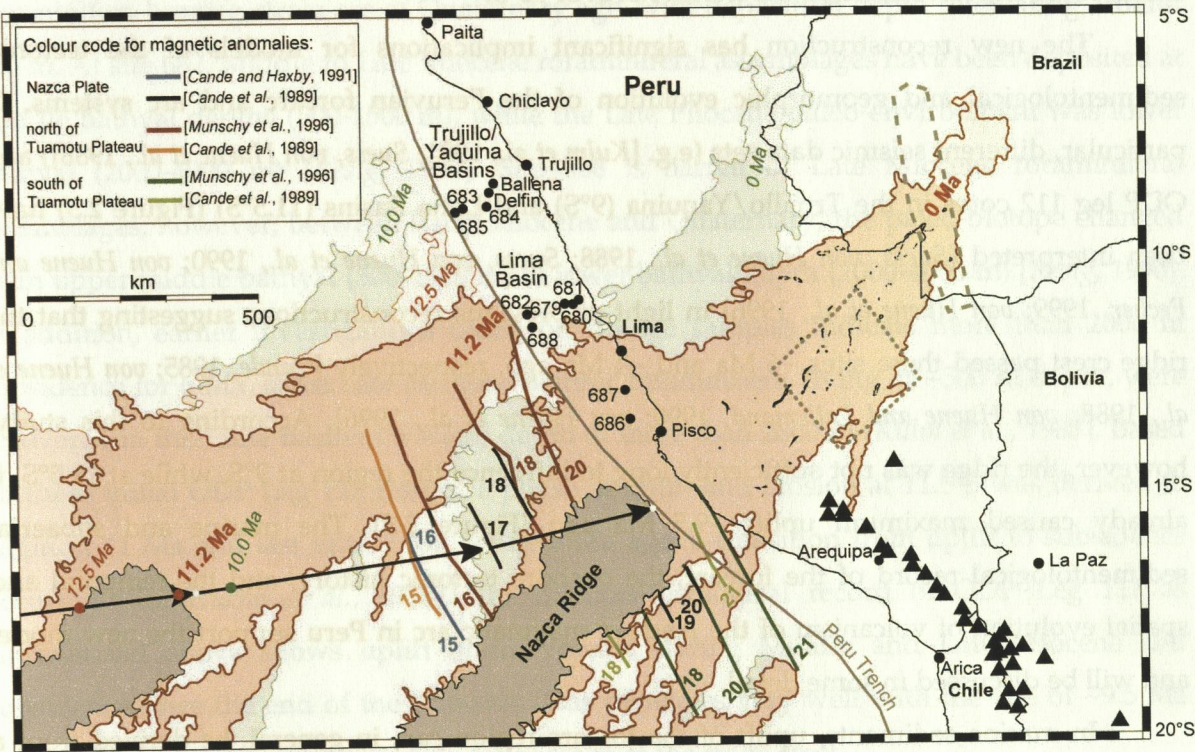


Figure 2.7: Migration history of the Nazca Ridge on the assumption that the mirrored Tuamotu Plateau resembles the subducted part of the Nazca Ridge. The magnetic anomalies on the Nazca Plate are marked in black and blue. The magnetic lineations north and south of the Tuamotu Plateau have red and green colours, respectively (see inset). At the present collision zone, two endmember models for the continuation of the Nazca Ridge are shown: Adjusting chrons 15-20, located north of both features, yields the red mirror image of the plateau. Fitting chrons 18-21, located south of both ridges, leads to a position of the mirrored Tuamotu Plateau shown as the green mirror image. Both mirror images are plotted without consideration of the variable dip of the subducting plate. For both mirror images, the lighter colours at their northeasternmost ends mark the ~200 km long part of the Tuamotu Plateau which most likely does not have a counterpart on the Nazca Plate (see text for details). Thus, the red mirror image with a linear continuation of ~900 km is the preferred scenario of this study. Note the coincidence of the preferred red mirror image with the reduced intermediate depth seismicity (dotted line) and with the presence of deep seismic events beneath Brazil (dashed line). For the onset of ridge subduction, three different scenarios are presented: Using the preferred configuration, the original Nazca Ridge entered the trench ~11.2 Ma ago at 11°S (red). If the original Nazca Ridge continues for 1100 km, its subduction began ~12.5 Ma ago at 10°S (light red). The northernmost possible contact of ridge and trench at 8.5°S corresponds to a mirror image adjusted to chrons 19-21 (green).

Taken together, these arguments strongly support a linear continuation of the ridge of ~900 km and an onset of ridge subduction ~11.2 Ma ago at 11°S.

If the Nazca Ridge, continuing with a linear trend, had entered the trench at 8°S [Cande, 1985; Huene *et al.*, 1988; von Huene and Lallemand, 1990; von Huene *et al.*, 1996], its subduction would have begun ~16 Ma ago and the original ridge would have to be at least 1500 km long. Such a length is not supported by the conjugate feature of the Nazca Ridge on the Pacific Plate, since the entire Tuamotu Plateau is at most 1100 km longer than the modern Nazca Ridge. Thus, although the trench has probably been shifted eastward for at least 20 Ma due to tectonic erosion [von Huene and Lallemand, 1990], a linearly trending original Nazca Ridge could not have reached the trench north of 10°S.

The new reconstruction has significant implications for models of the tectonic, sedimentological and geomorphic evolution of the Peruvian forearc and arc systems. In particular, different seismic data sets (e.g. [Kulm *et al.*, 1981; Suess, von Huene *et al.*, 1988]) and ODP leg 112 cores in the Trujillo/Yaquina (9°S) and Lima Basins (11.5°S) (Figure 2.5) have been interpreted [Suess, von Huene *et al.*, 1988; Suess, von Huene *et al.*, 1990; von Huene and Pecher, 1999; von Huene *et al.*, 1996] in light of previous reconstructions suggesting that the ridge crest passed these sites ~6 Ma and ~4 Ma ago, respectively [Cande, 1985; von Huene *et al.*, 1988; von Huene and Lallemand, 1990; von Huene *et al.*, 1996]. According to this study, however, the ridge was not sufficiently long to influence the region at 9°S, while at 11.5°S, it already caused maximum uplift ~9.5 Ma ago (Figure 2.5). The marine and subaerial sedimentological record of the forearc, the onshore tectonic history, and the temporal and spatial evolution of volcanism of the Andean magmatic arc in Peru support the new model and will be discussed in some detail.

In marine sediments, uplift of the forearc region can, in general, be derived from a trend to coarser deposits, possibly accompanied by an increase in the number of unconformities, and from benthic foraminiferal stratigraphy that gives information on the water depth at which the sediment was deposited. At 9°S, benthic foraminiferal assemblages in ODP Leg 112 cores and dredge samples indicate that the continental slope and shelf subsided ~1500 m between the Middle Eocene to Middle Miocene and experienced further subsidence of 1300 m since 12-13 Ma [Kulm *et al.*, 1988; Resig, 1990]. Apart from that, cores recovered during ODP Leg 112 and two industrial wells are characterized by the deposition of fine-grained material, while sandy deposits are missing in the Miocene (Figure 2.8) [Suess, von Huene *et al.*, 1988]. Especially in the Ballena industrial well, located above the crest of the outer shelf high, continuous shale deposition between 18–7 Ma [Schrader and Castaneda, 1990] argues against the disturbance of the deposition milieu due to the passage of a ridge (Figure 2.8a). A comparison with the recent collision zone shows that the shelf area is

strongly affected by the Nazca Ridge. Marine deposits of Eocene to upper Pliocene age, that correlate with equivalent strata in submerged offshore forearc basins off Central Peru, have been raised above sea level [Hsu, 1992].

At 11.5°S, deposits at ODP Leg 112 sites become coarser, with a decrease in mud and an increase in silt and sand during the Middle and Late Miocene (Figure 2.8b). At site 679, a layer of conglomerates has been deposited before the end of the Miocene. In cores recovered at ODP site 679, Middle and Late Miocene benthic foraminiferal assemblages reflect deposition on the inner shelf in shallow water [Resig, 1990]. Following the hiatus at the end of the Late Miocene, deposition resumed at the outer shelf in the early Pliocene. The next foraminifers-bearing strata are of Quaternary age, with deposition depth fluctuating around 400 m. At site 682, Middle to Late Miocene foraminiferal assemblages have been deposited at middle bathyal depths (500-1500 m), while the Late Pliocene paleo-environment was lower bathyal (2000-4000 m) [Resig, 1990]. Site 688 is barren of Late Miocene foraminiferal assemblages, however, between Early Miocene and Quaternary, the paleo-biotope changed from upper middle bathyal (500-1500 m) to lower bathyal depth (2000-4000 m) [Resig, 1990]. In addition, earlier investigations based on dredge samples indicate more than 2000 m subsidence for 6 Ma, since Late Miocene benthic foraminifers, living at ~500 m depth, were recovered in the Lima Basin at a water depth of more than 2600 m [Kulm *et al.*, 1988]. Based on these initial ODP Leg 112 results, a phase of uplift and erosion at 11.5°S was derived to begin at 11 Ma and last until 7 Ma, while 6 Ma ago, a transition from uplift to subsidence occurred [von Huene *et al.*, 1988]. The offshore geological record of ODP Leg 112 as summarized above shows uplift of the forearc during Middle and Late Miocene and subsidence since the end of the Miocene. This correlates very well with the age of ~9.5 Ma derived from the new reconstruction for passage of the ridge crest.

The new model is also compatible with the sedimentological record of the Rímac-Chillón Rivers at 12°S, which eroded deep valleys on the Lima coastal plain during the Miocene. The alluvial fan deposited by these rivers experienced uplift of at least 500 m, which is attributed to the passage of the Nazca Ridge [le Roux *et al.*, 2000]. Potential sea level changes during the Quaternary and Pliocene are smaller than ~125 m and have been considered [le Roux *et al.*, 2000]. The uplift maximum at 12°S was attained before the end of the Miocene [le Roux *et al.*, 2000].

Another piece of evidence in support of the presented model may be inferred from the correlation of the Nazca Ridge with the associated segment of low-angle subduction and the cessation of magmatic arc activity. At present, the boundary between active and ceased volcanism in the south and in the north, respectively, is located in the landward continuation

of the ridge, but may have gradually propagated southward due to the lateral movement of the ridge. Offshore, volcanic ash layers recovered during ODP leg 112 have been interpreted to show higher activity of the Peruvian volcanic arc in the Late Miocene for 9°S than for 12°S [Pouclet *et al.*, 1990]. Onshore geochronological data throwing light on a possible southward propagating zone, where volcanism has ceased, is, however, rather limited [Noble *et al.*, 1974; Mégard *et al.*, 1976]. Pulses of Miocene volcanic activity [Noble *et al.*, 1974; Mégard *et al.*, 1976] have been interpreted in context of the Quechua tectonic phases of the Andean orogeny in Peru during the Middle to Late Miocene [Pouclet *et al.*, 1990; Mégard *et al.*, 1984]. The Quechua II (~10 Ma) and Quechua III (~5 Ma) tectonic phases, which seem to be related to changes in the relative plate motion of the Nazca and South American Plates [Noble *et al.*, 1974; Pardo-Casas and Molnar, 1987], have been correlated with unconformities in ODP leg 112 cores at 11.5°S [von Huene *et al.*, 1988]. According to this study, the Nazca Ridge influenced this region ~9.5 Ma ago, which seems to coincide with the Late Miocene Quechua II tectonic phase. Despite this apparent correlation, it should be noted that the concept of distinct tectonic phases in Peru has been criticized, as the available temporal constraints argue in favour of prolonged periods of tectonic activity [Noble *et al.*, 1996]. Nevertheless, in the Ecuadorian Andes, subduction of the Carnegie Ridge since the Middle Miocene may be responsible for the development of a higher topography, a compressional stress regime, and increased crustal cooling and exhumation rates, deduced from fission track data in the collision zone [Spikings *et al.*, 2001].

While, in summary, no single observation is conclusive about its relation to the subduction of the Nazca Ridge, the combination of the arguments raised above strongly suggests that the new model is more compatible with the existing geological and geomorphic data.

2.3.4 Conclusions

This reconstruction of the migration history of the Nazca Ridge along the Peruvian margin suggests that the lateral motion of the ridge has decelerated through time. Considering that a small amount of the relative convergence rate between the Nazca and South American plates is taken up by intra-plate deformation in the Andean mountain belt results in slower lateral migration of the ridge. However, this has no effect on the geological implications of the new model. On the assumption that the original Nazca Ridge has a length similar to its mirror image on the Pacific Plate, it continues for ~900 km beneath South America. Therefore, the northeastern end of the Nazca Ridge entered the trench ~11.2 Ma ago at 11°S. As a consequence, the ridge did not have an impact on the region north of 10°S, where the

northern transect of ODP Leg 112 is located. The region at 11.5°S off Lima has been affected by ridge subduction ~9.5 Ma ago. Support for the model is provided by the sedimentological and paleo-bathymetric record in ODP Leg 112 and industrial well cores. At 9°S, cores show mostly fine-grained sediments on the continental slope and, on the shelf, continuous shale deposition. At 11.5°S, the predicted age of the new model correlates well with a Late Miocene period of uplift and erosion followed by subsidence since ~6 Ma. In light of this study, seismic and drilling data sets acquired along the Peruvian margin in the last decades offer the possibility to compare regions that have not been affected by the ridge passage with regions that have been influenced by the ridge, but otherwise share similar boundary conditions. Such a comparison may enable a better quantification of the geodynamic influence of the Nazca Ridge on the Peruvian margin in future studies. The case of the Nazca Ridge emphasizes that models regarding the geodynamic evolution of active margins have to take into account the migration history and three-dimensional effects associated with laterally migrating bathymetric highs.

3 Geophysical data acquisition, processing and interpretation

The Nazca Ridge and its collision zone with the South Peruvian active margin were investigated by wide-angle and reflection seismic profiles as well as bathymetric, gravimetric, and magnetic surveying. This study focusses on the seismic and bathymetric data (Figure 3.1); gravimetric and magnetic data have been treated in *Heinbockel* [2003]. All data were acquired during cruise SO146 of the German research vessel "Sonne", which lasted from March to May 2000 and covered several key regions off Peru [*Bialas and Kukowski, 2000*]. The cruise was carried out within the framework of the GEOPECO project (GEOphysical experiments at the PERuvian COntinental margin - investigations of tectonics, mechanics, gas hydrates, and fluid transport), a collaboration of institutes in Germany, USA and Peru (GEOMAR Kiel, GFZ Potsdam, Universities of Hamburg and Bremen; Universities of Texas in Austin and of Utah in Salt Lake City; Peruvian Institute for Geophysics in Lima). The objectives of the project were multidisciplinary geophysical and geological investigations focussing on the quantitative characterization of the structures and geodynamics of the Peruvian section of the Andean subduction zone and the associated gas hydrate and fluid transport systems.

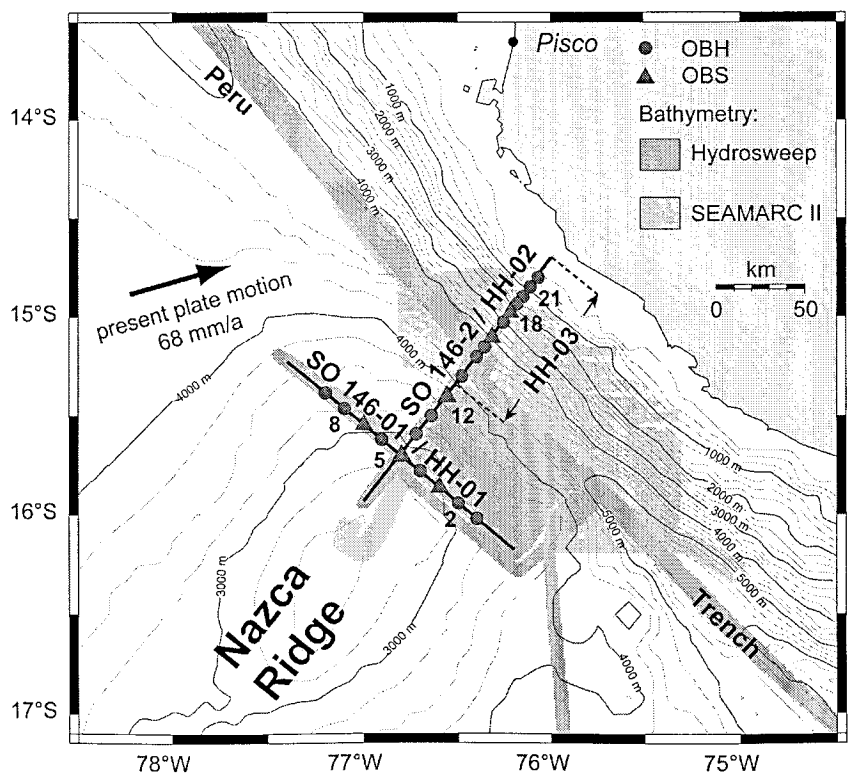


Figure 3.1: Location map of the Nazca Ridge at the intersection with the Peru margin. Wide-angle seismic profiles SO146-01 and SO146-02 coincide with reflection seismic lines HH-01, HH-02 and HH-03. Areas shaded in dark and light grey were covered by Hydrosweep (this cruise) and SEAMARC II (acquired in 1987 by SOEST, Hawaii) bathymetry, respectively.

3.1 Data acquisition and processing

Multibeam swath bathymetry was collected between 14°S and 17°S (Figure 3.2) using the onboard Hydrosweep system [Grant and Schreiber, 1990]. The data were edited and processed with the MB-System software package [Caress and Chayes, 1995]. The spatial resolution is ~200 m at 6000 m water depth. The data of the SO146-GEOPECO cruise has been compiled with bathymetry extracted from side-scan sonar data acquired by SOEST, Hawaii, in 1987 [Hussong *et al.*, 1988; Hagen and Moberly, 1994; Li and Clark, 1994].

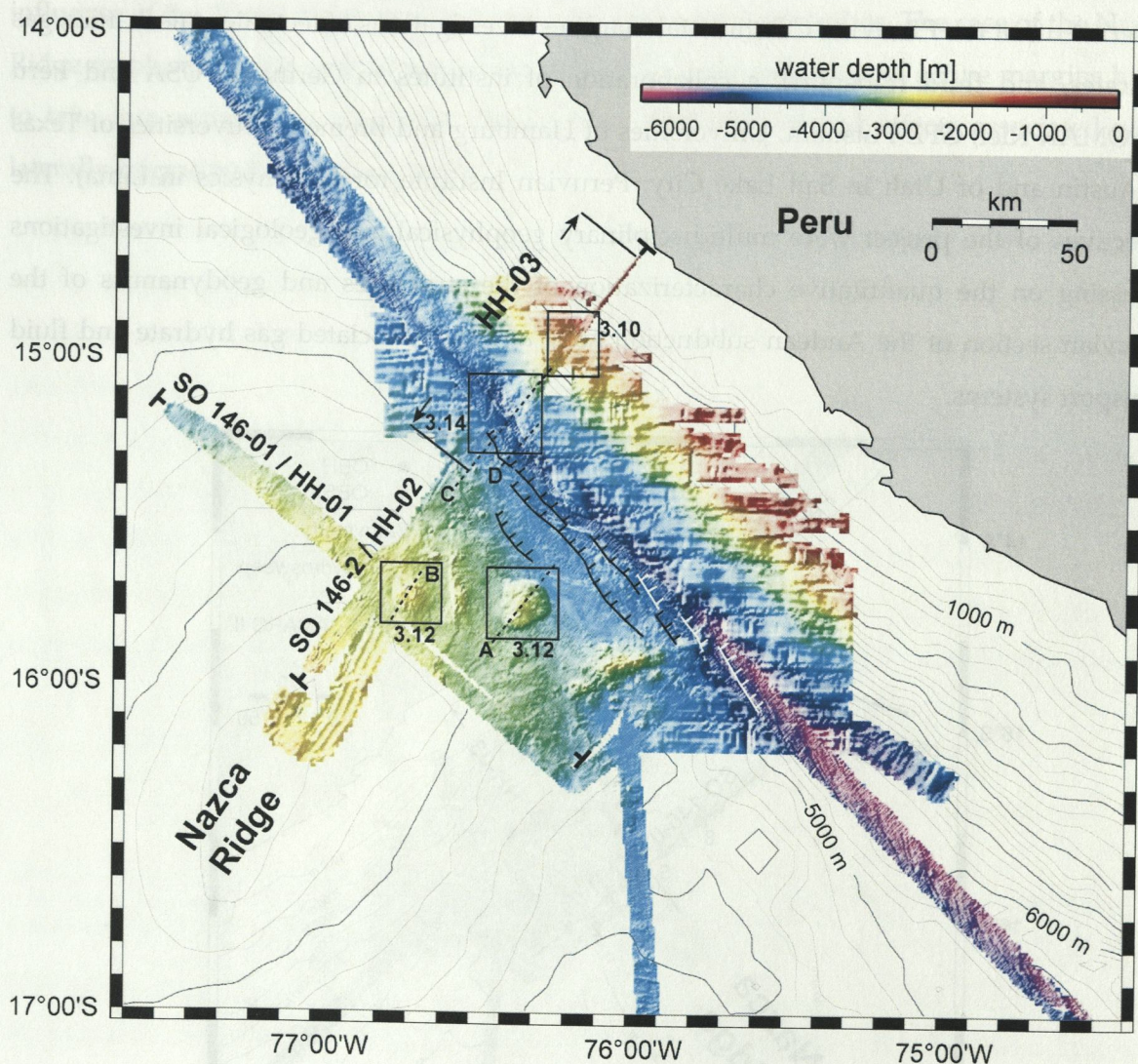


Figure 3.2: Bathymetric map compiled from Hydrosweep and SEAMARC II data, underlain by ETOPO5 contour lines [Smith and Sandwell, 1997a]. Boxes with numbers refer to detailed sections shown in Figures 3.11a, 3.13a and 3.15a. Dashed lines mark the locations of bathymetric profiles shown in Figures 3.13b and 3.15b. Note the normal faults striking parallel to the trench.

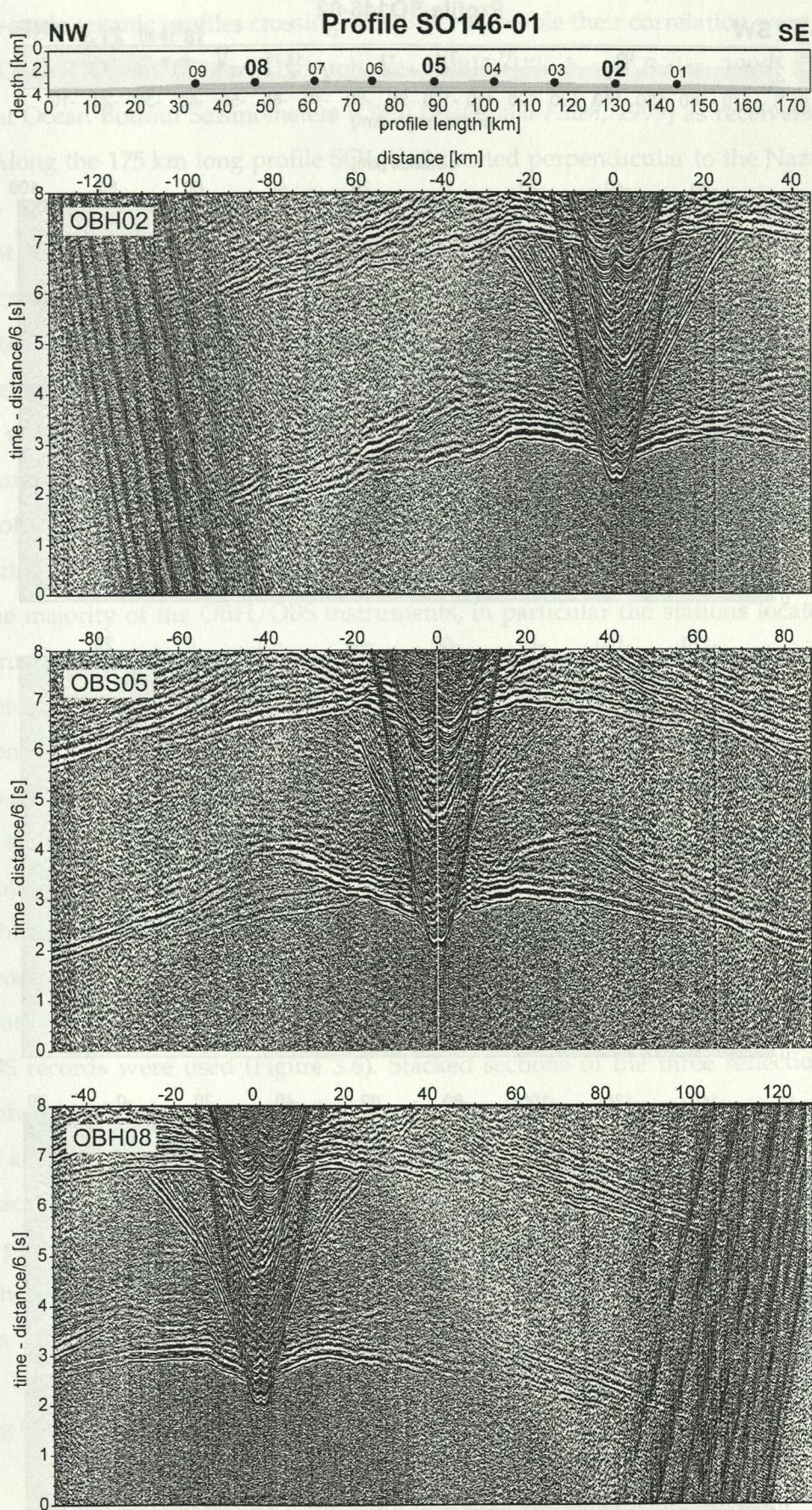


Figure 3.3: Example OBH record sections of the wide-angle seismic profile SO146-01 located perpendicular to the ridge axis. The sections are displayed time-reduced by 6 km/s.

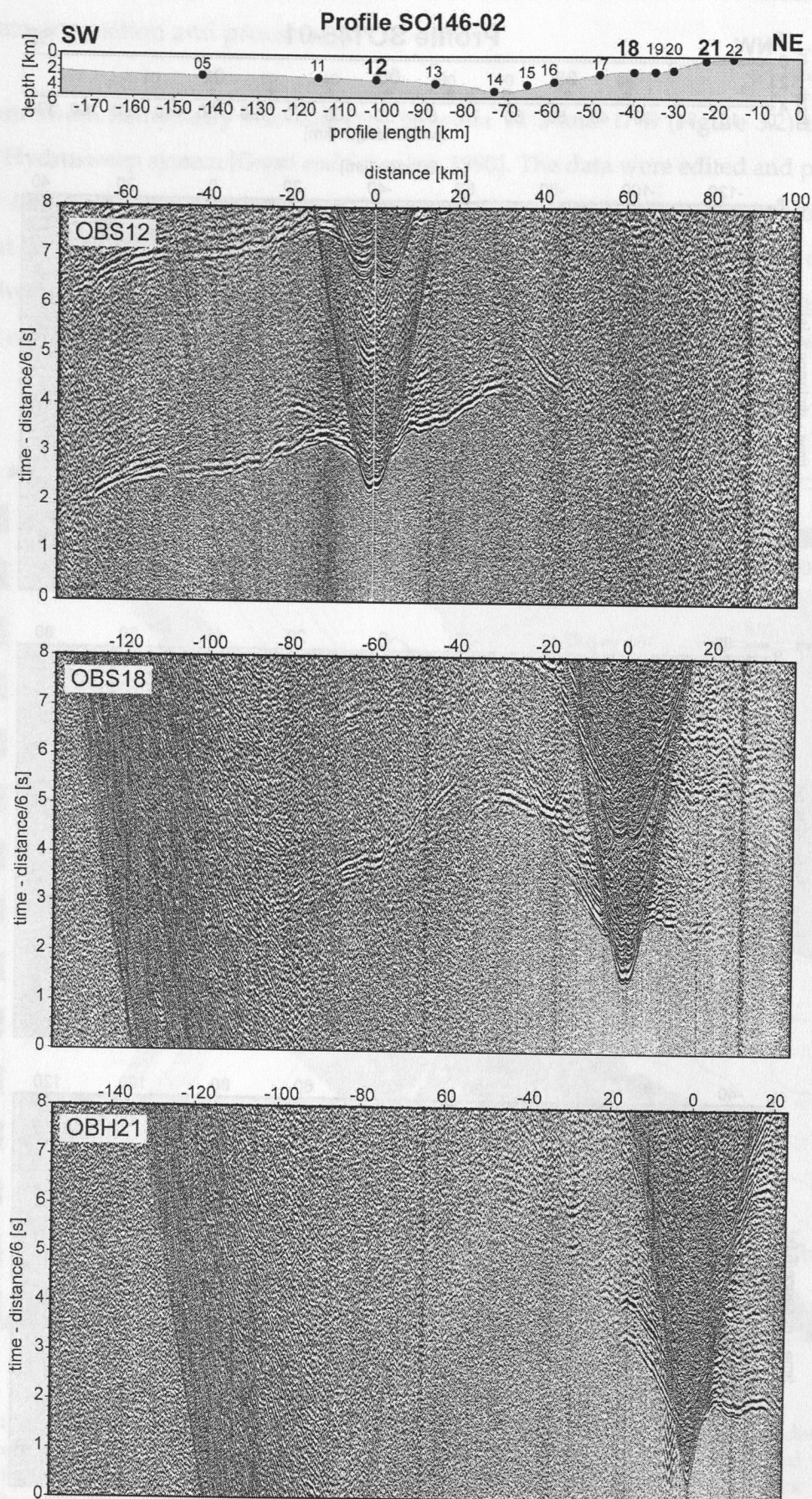


Figure 3.4: Example OBH record sections of the wide-angle seismic profile SO146-02 running along the ridge crest and extending towards the shelf. The sections are displayed time-reduced by 6 km/s.

Two wide-angle seismic profiles crossing each other to enable their correlation were acquired using GEOMAR Ocean Bottom Hydrophones (OBH) [Flueh and Bialas, 1996] and three-component Ocean Bottom Seismometers (OBS) [Bialas and Flueh, 1999] as receivers (Figures 3.3, 3.4). Along the 175 km long profile SO146-01 located perpendicular to the Nazca Ridge, six OBHs and three OBSs were symmetrically positioned around station OBS05. This instrument was also used as the westernmost station for the other profile (SO146-02) along the ridge crest (Figure 3.1). On this line, which extends up to the continental shelf, three other OBS and ten OBH instruments were deployed. For both profiles, an array of three 32 1 Bolt airguns generated the seismic signal every 60 seconds, resulting in a shot distance of 120 m. The shots were additionally recorded by a single-channel streamer (profiles HH-01, HH-02). Furthermore, a shorter multi-channel seismic line (HH-03), coincident with the northeastern part of profile SO146-02 that covers trench and continental slope, was acquired using two GI airguns firing every 20 m, to achieve higher resolution (Figure 3.5).

The majority of the OBH/OBS instruments, in particular the stations located on the oceanic crust and on the lower slope, recorded high quality data with the exception of the seismometer of OBS05 and three OBHs on profile SO146-02. Most instruments including the hydrophone of OBS05 show clear signals to large offsets, some over the entire profile length and up to an offset of ~140 km (Figures 3.3, 3.4). All stations on profile SO146-01 and most of SO146-02 show pronounced wide-angle reflections (PmP) at large offsets related to the crust-mantle boundary, allowing to tightly constrain the location of the Moho. Stations located on the shelf have a higher noise level than those located more seaward.

Processing of the wide-angle seismic data included frequency filtering and deconvolution analysis. To derive the final velocity models of both profiles, all available OBH/OBS records were used (Figure 3.6). Stacked sections of the three reflection seismic profiles provided information about the morphology of the sediment layers and crystalline crust and additionally constrained the velocity models (Figures 3.7-3.10). Forward modelling by ray-tracing was carried out using programs by Luetgert [1992] and Zelt and Smith [1992]. The two profiles were correlated by OBS05 station. Ray coverage is good for both profiles, despite the three missing records on SO146-02 (Figure 3.6). The resolution of the velocity models is ~100 m and ~800 m for the lower and upper layers respectively. A very good fit between observed and calculated traveltimes is achieved, with time differences not exceeding 0.3 s (Figures 3.8, 3.10) in the near-offset and 0.5 s in the far-offset.

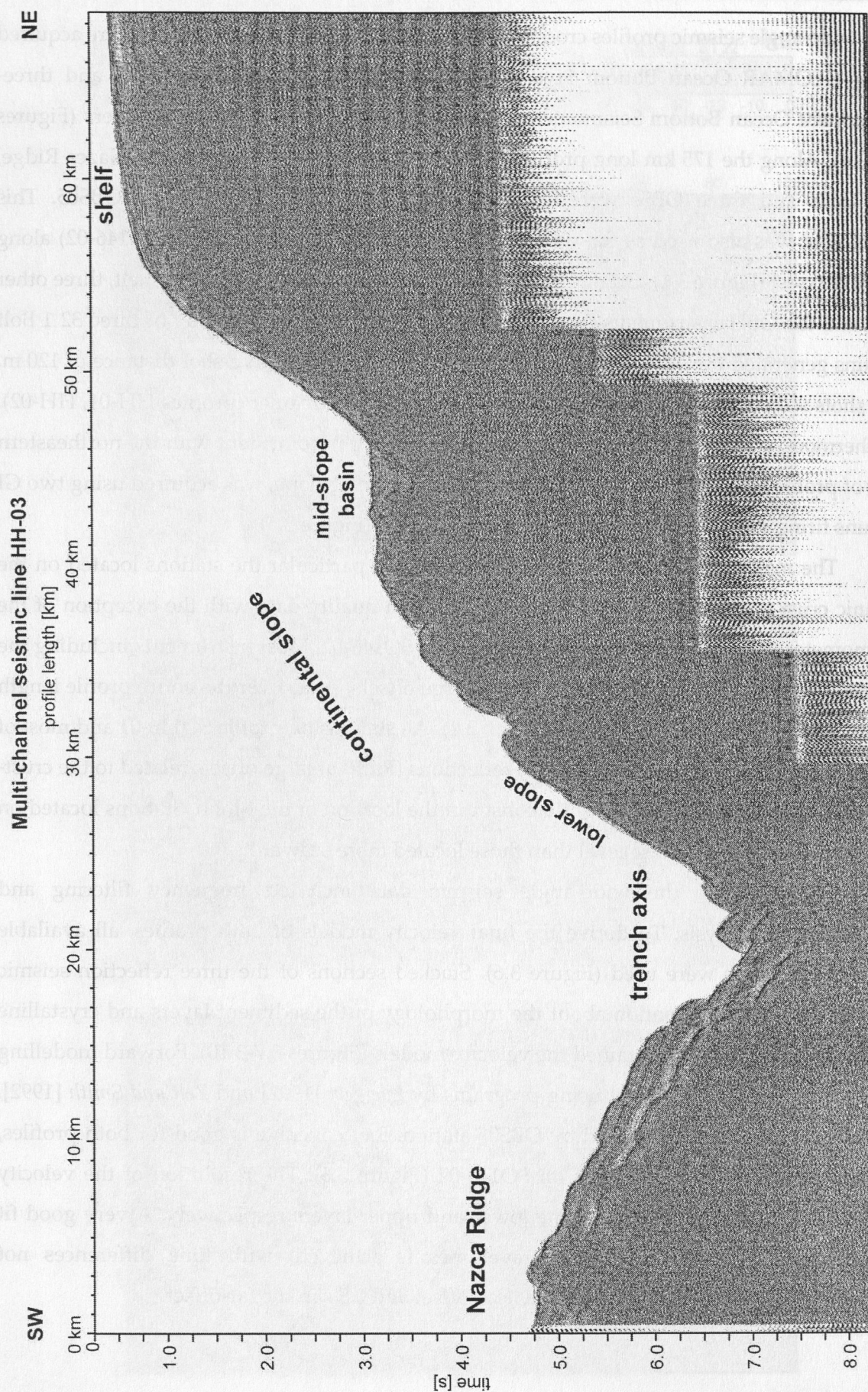


Figure 3.5: Overview of multi-channel seismic line HH-03 covering the crest of the Nazca Ridge, trench and continental slope. For detail sections see Figure 3.9.

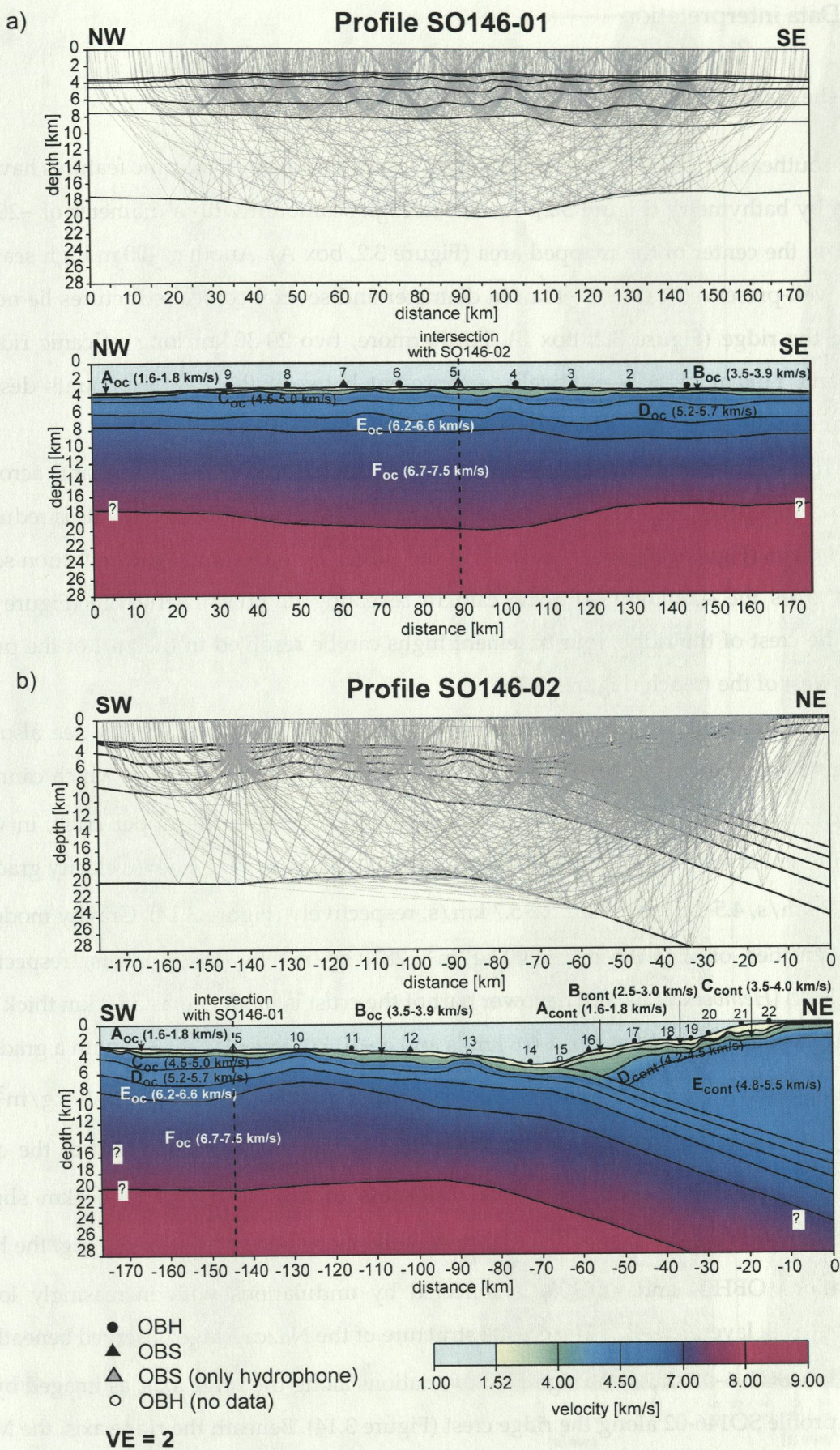


Figure 3.6: Ray coverage for the associated velocity fields obtained by forward modelling of the wide-angle seismic lines a) SO146-01 and b) SO146-02. The profiles intersect at station OBS05.

3.2 Data interpretation

3.2.1 The Nazca Ridge

On the southeastern flank of the Nazca Ridge, several prominent volcanic features have been imaged by bathymetry (Figure 3.2). A ~800 m high seamount with a diameter of ~20 km is located in the center of the mapped area (Figure 3.2, box A). Another 400 m high seamount with a well-preserved caldera ~4 km in diameter and several conical structures lie near the crest of the ridge (Figure 3.2, box B). Furthermore, two 20-30 km long volcanic ridges of 500 m and 1100 m high, respectively, are present between the two seamounts described above and in the south of the mapped area, respectively (Figure 3.2).

The sedimentary cover on the ridge is 300-400 m thick both, along and across the ridge axis, except on the volcanic features, where the thickness of the sediments is reduced to tens of meters (Figure 3.7). Near the crest of the ridge, the wide-angle and reflection seismic profiles cross the seamount with the caldera revealing its crustal structure (Figure 3.7a). Along the crest of the ridge, four basement highs can be resolved in the part of the profiles located west of the trench (Figures 3.7b).

Forward modelling of the wide-angle seismic data (Figures 3.6, 3.8, see also 3.14) yields a velocity between 1.6-1.8 km/s for the oceanic sediment layer A_{oc} , which cannot be resolved any further. Seismic velocities increase rapidly within the upper crust, in which three different layers (B_{oc} - D_{oc}) can be distinguished. Layers B_{oc} - D_{oc} show velocity gradients of 3.5-3.9 km/s, 4.5-5.0 km/s and 5.2-5.7 km/s, respectively (Figure 3.14). Gravity modelling yields densities of 2500 kg/m³, 2700 kg/m³, 2810 kg/m³ for these layers, respectively (Figure 3.12) [Heinbockel, 2003]. The lower part of the crust is modelled as a ~2 km thick layer (E_{oc}) with a velocity gradient of 6.2-6.6 km/s and a ~10 km thick layer (F_{oc}) with a gradually increasing velocity of 6.7-7.5 km/s. Layers E_{oc} and F_{oc} show densities of 2910 kg/m³ and 2980 kg/m³, respectively (Figure 3.12). Layer F_{oc} constitutes more than half of the entire crustal thickness (Figure 3.14). The total thickness of layers B_{oc} - E_{oc} of 4-5 km slightly increases towards the southeast. The highly variable morphology of layer B_{oc} , e.g. the highs near stations OBH04 and OBH06, is reflected by undulations with increasingly longer wavelengths in layers C_{oc} - E_{oc} . The crustal structure of the Nazca Ridge observed beneath the crest in line SO146-01 shows no significant variations along the ridge axis, as imaged by the seismic profile SO146-02 along the ridge crest (Figure 3.14). Beneath the ridge axis, the Moho is located ~20 km below sea level, while it lies at ~18 km and ~16 km below sea level beneath the northwestern and southeastern ends of the profile, respectively.

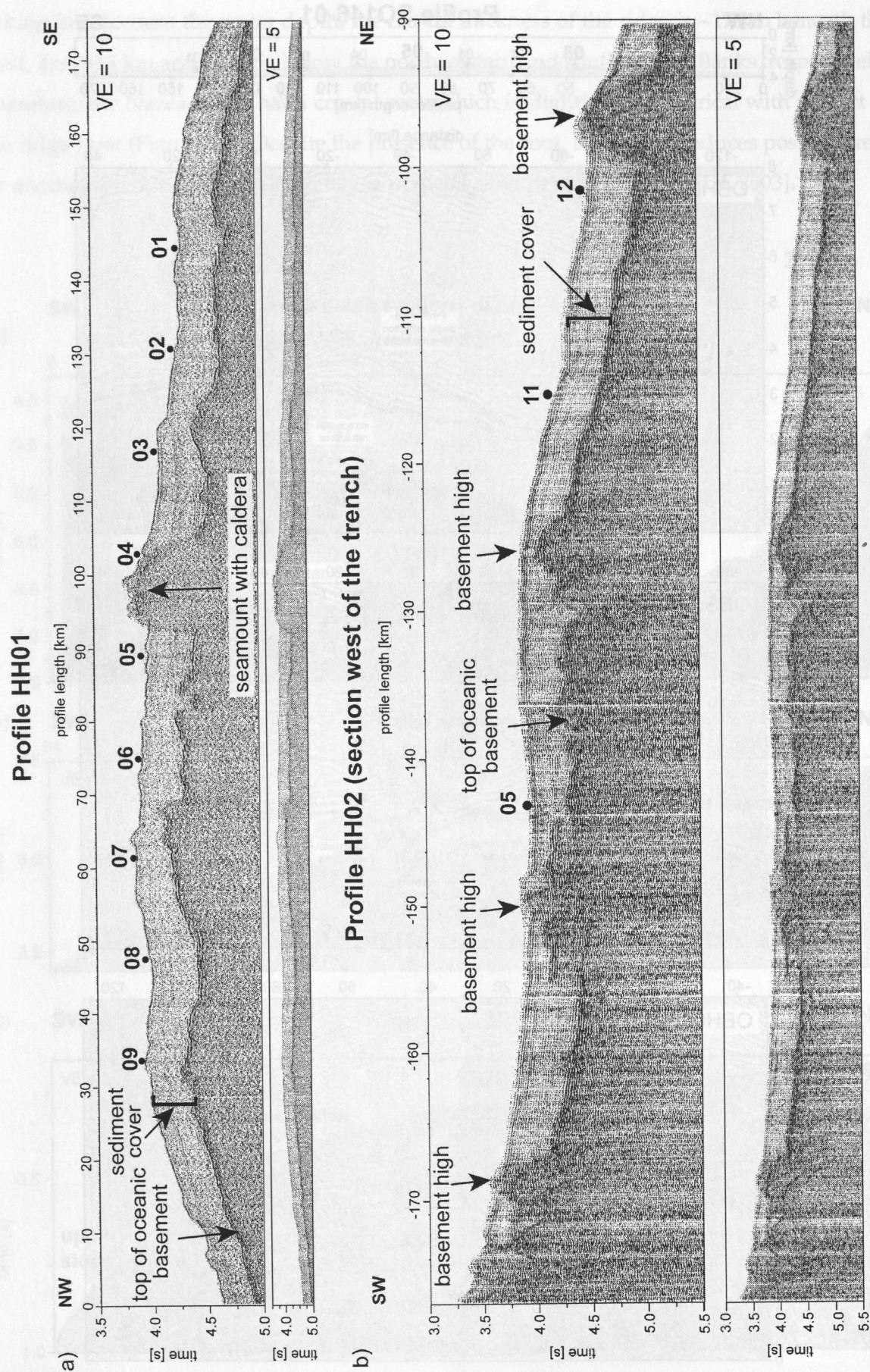


Figure 3.7: a) Reflection seismic line HH-01 (single-channel) perpendicular to the ridge axis and b) the part of HH-02 located west of the trench running along the ridge crest. See Figure 3.1 for location.

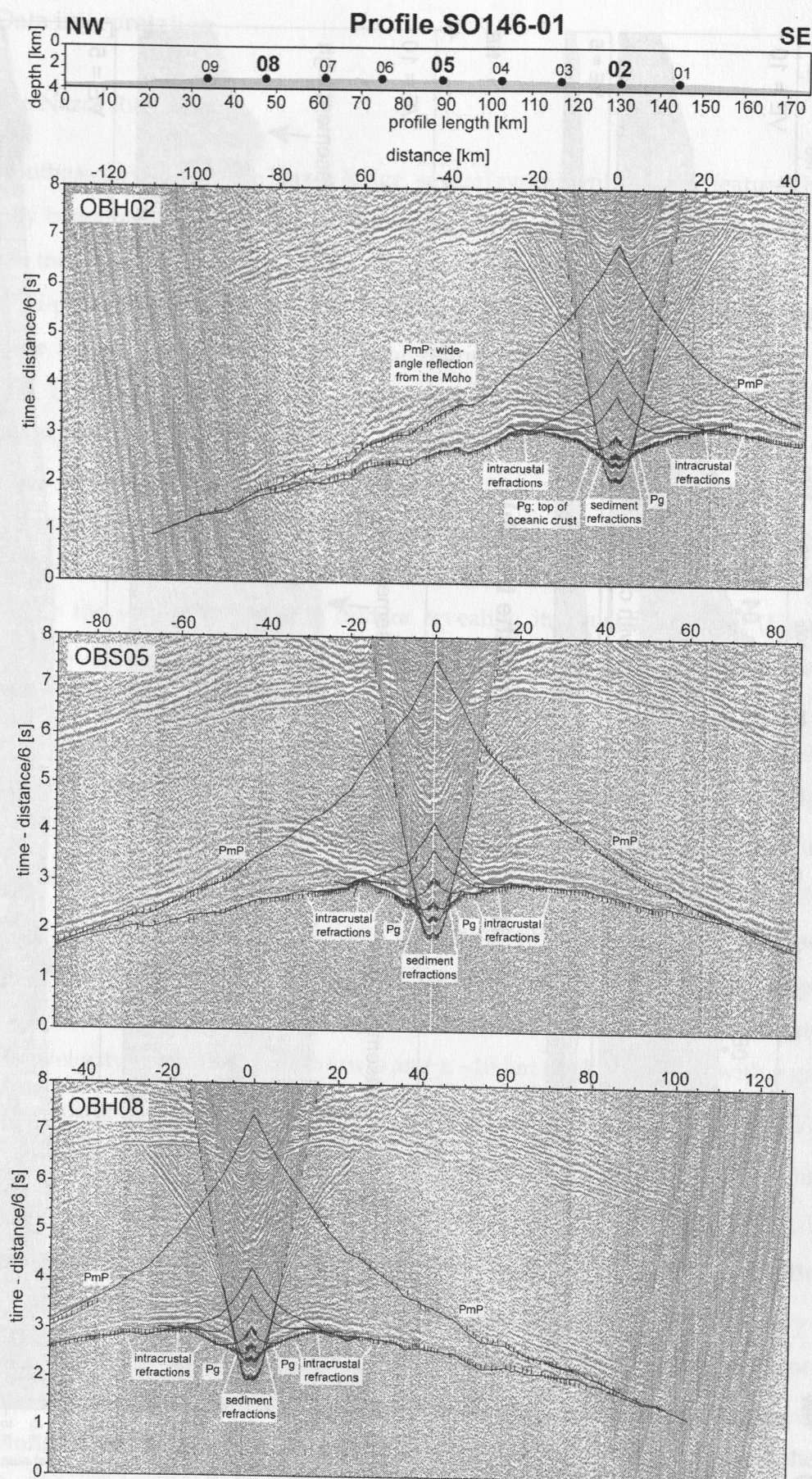


Figure 3.8: Interpretation of OBH sections of profile SO146-01 shown with observed and calculated travel times obtained by two-dimensional ray-tracing.

Taking into account the water depth, the crustal thickness of the ridge is ~17 km beneath the crest, and ~16 km and ~14 km below the northwestern and southeastern flanks, respectively. Therefore, the Nazca Ridge has a crustal root, which is slightly asymmetrical with respect to the ridge crest (Figure 3.6). Despite the presence of the root, the ridge produces positive free-air anomalies, thus it is not completely isostatically compensated [Heinbockel, 2003].

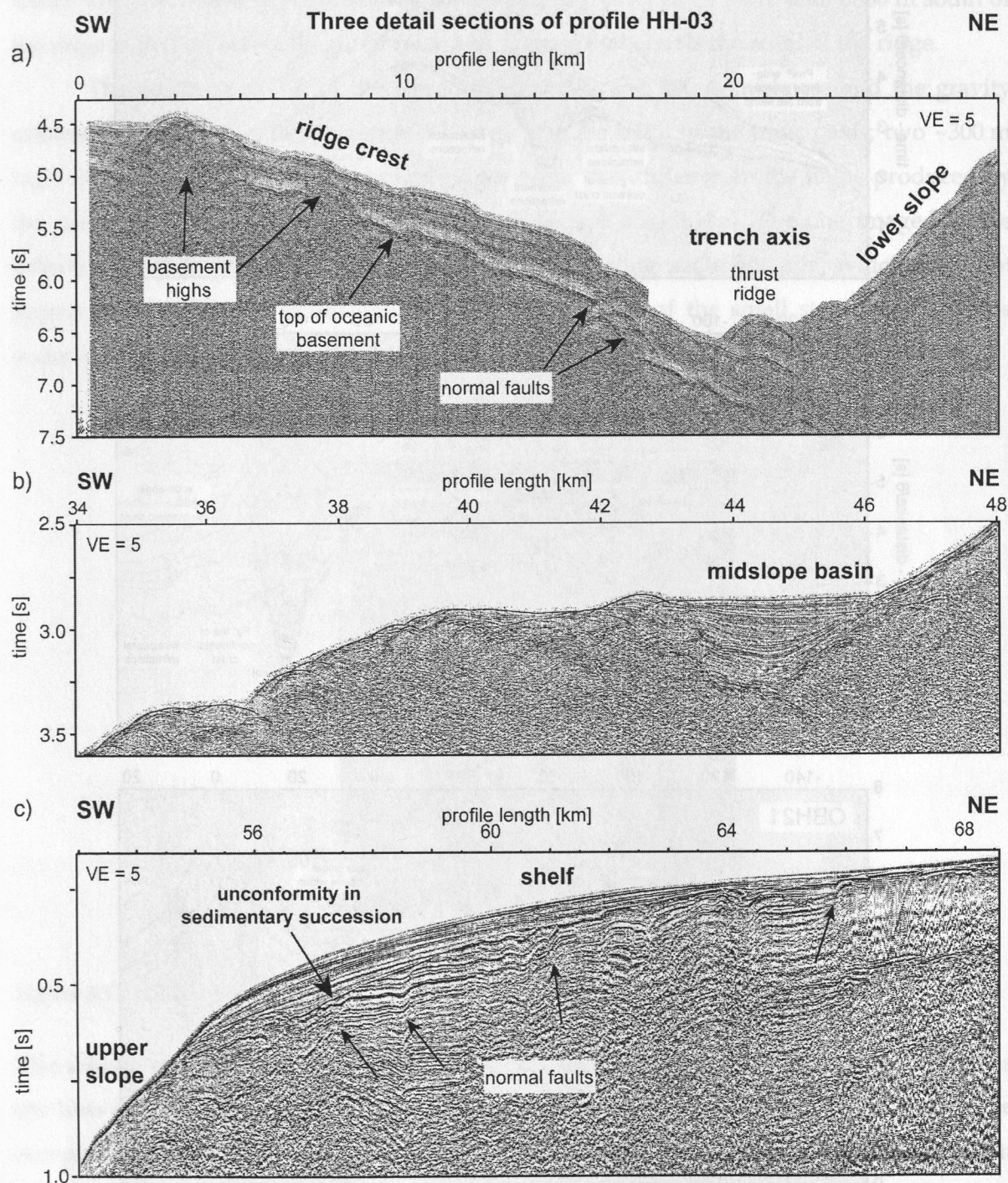


Figure 3.9: Three parts of multi-channel seismic line HH-03: a) ridge crest, trench and lower slope (profile kilometer 0-28), b) mid-slope basin (km 34-48) and c) upper slope and shelf (km 50-69).

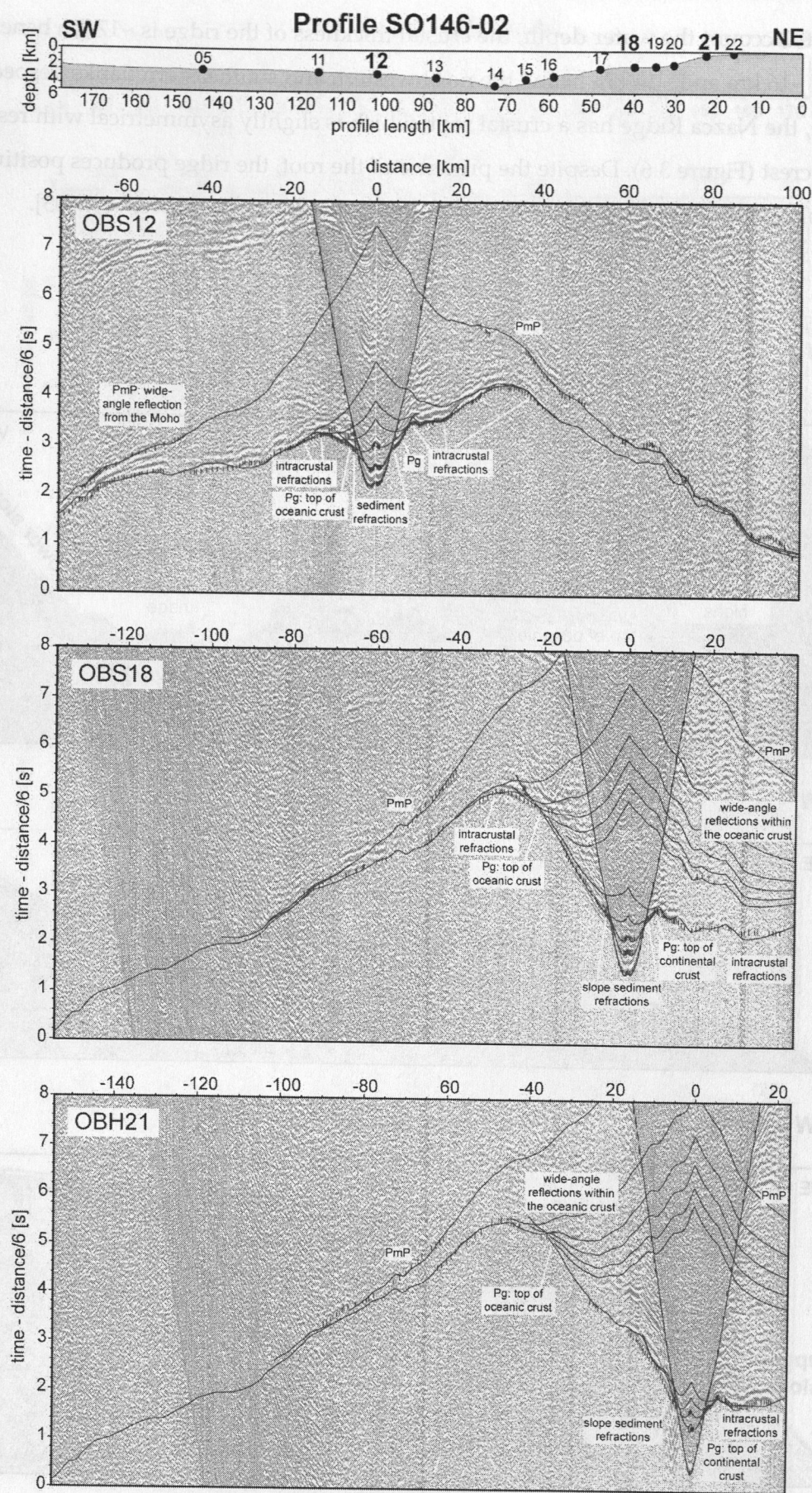


Figure 3.10: Interpretation of OBH sections of profile SO146-02 shown with observed and calculated travel times obtained by two-dimensional ray-tracing.

3.2.2 The structure of the collision zone

The Nazca Ridge does not seem to undergo major deformation due to the collision with the margin before it has approached the trench by ~20 km. At this distance, bending of the plate into the subduction zone leads to the trench-parallel normal faults that increase in number and frequency trenchward (Figures 3.2, 3.9). The normal faults have vertical offsets of up to 200 meters (Figure 3.9). At the collision zone, the ridge does not alter the curvature of the trench line. The water depth along the trench axis decreases from more than 6500 m south of the ridge to 5000 m above the ridge crest, a difference that equals the relief of the ridge.

The sedimentary fill of the trench does not exceed 400 m thickness and the gravity minimum associated with the trench is narrow (Figure 3.12). In the trench axis, two ~300 m high and 10-15 km long trench-parallel ridges occur that differ from the highs produced by the normal faults in the oceanic plate (Figure 3.2, see also 3.15a). The one imaged in the reflection seismic section is located above the subducting sediment pile, which does not appear to be deformed significantly (Figure 3.9a). North of the small structural high, the water depth reaches a local maximum located in the middle of a 20 km wide re-entrant.

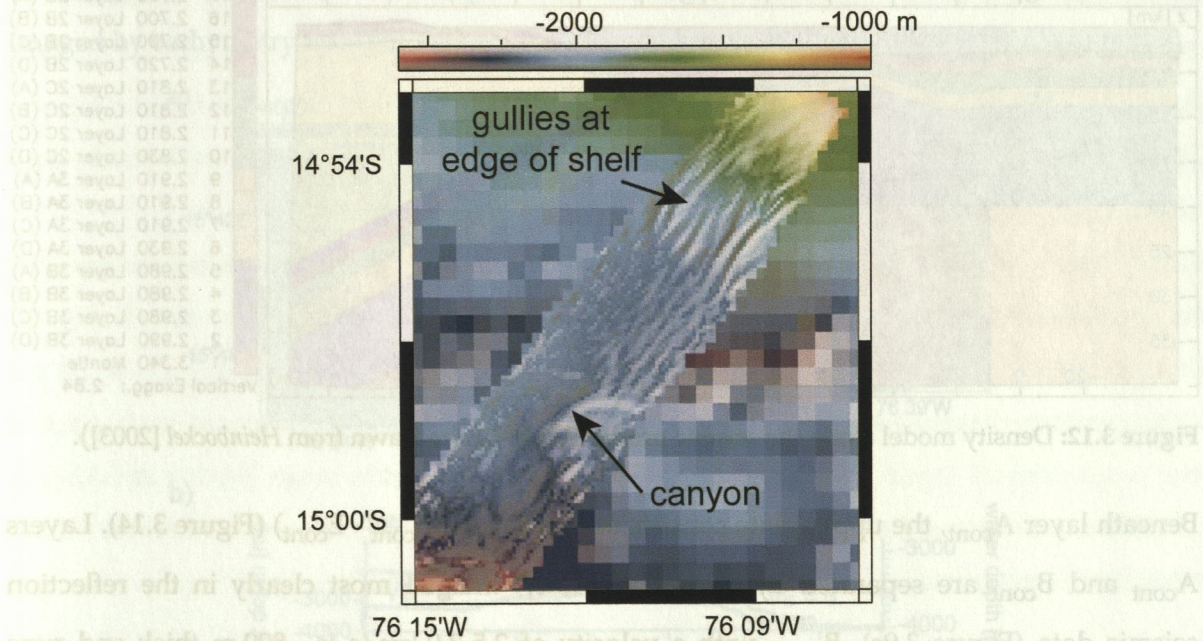


Figure 3.11: Gullies and canyon at the upper continental slope. See Figure 3.2 for location.

The seismic profiles running along the ridge crest show the same thin layer of sediments as the lines across the ridge. The reflection seismic section shows that the sediments seem to be completely subducted. In the velocity model derived from the wide-angle seismic data, an individual downgoing sediment layer cannot be resolved (Figures 3.10, 3.14). The steep 9.5° dipping lower continental slope and the mid-slope with an angle of 4.4° have a rough

topography with structural highs and canyons (Figure 3.2, 3.5). Up to the mid-slope, the sediment layer with a velocity of 1.6-1.8 km (A_{cont}) is only few hundred meters thick. On the 2.4° dipping mid-slope, two small sediment-filled basins are present (Figures 3.9b, 3.14). Another ~1 km thick sequence of sediments fills a depression of the basement on the outer shelf along 10 km of the profile SO146-02. Gullies present at ~2000 m water depth originate at the transition from the outer shelf to the upper slope (Figure 3.11). The uppermost sedimentary layer (A_{cont}) on the shelf is less than 100 m thick.

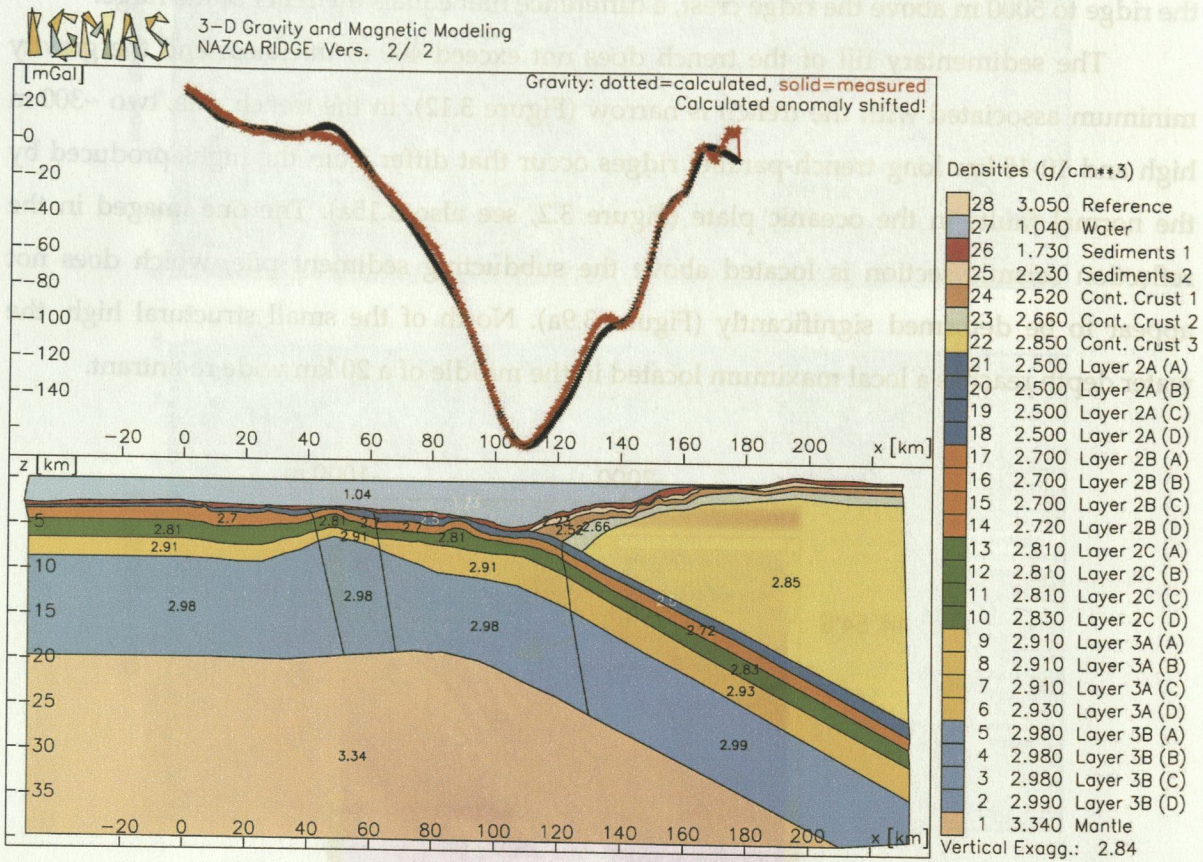


Figure 3.12: Density model along the seismic profile SO146-02 (redrawn from Heinbockel [2003]).

Beneath layer A_{cont} , the upper plate consists of four layers (B_{cont} - E_{cont}) (Figure 3.14). Layers A_{cont} and B_{cont} are separated by an unconformity, imaged most clearly in the reflection seismic data (Figure 3.9c). B_{cont} with a velocity of 2.5-3.0 km/s is ~800 m thick and runs parallel to the seafloor from the trench to the mid-slope (OBS18). Between OBS18 and OBH22, this layer forms the structural highs separating the basins described above. C_{cont} has a downward increasing velocity of 3.5-4.0 km/s. Its thickness decreases landwards from 2 km beneath the lower slope to 1 km at OBS18. D_{cont} that runs sub-parallel to the seafloor comprises velocities of 4.2-4.5 km/s, while the core of the continental wedge (E_{cont}) shows velocities between 4.8-5.5 km/s. The free-air gravity across the continental slope shows a

steep and relatively uniform gradient, while free-air anomalies around 10^{-5} m/s^2 occur along the coast [Heinbockel, 2003].

The Nazca Plate can be traced to a depth of $\sim 28 \text{ km}$ and subducts at an angle of $\sim 9^\circ$. In the subducted part of the ridge, seismic velocities and densities of the crustal layers increase by $\sim 0.5\text{--}1.0 \text{ km/s}$ and $\sim 200 \text{ kg/m}^3$, respectively (Figure 3.12) [Heinbockel, 2003].

3.3 Discussion

3.3.1 The Nazca Ridge

The surface of the Nazca Ridge lies, unlike the surrounding seafloor, above the carbonate compensation depth (at 4000 m water depth) and thus, a thin sediment cover consisting of calcareous ooze overlies the igneous crust of the ridge [Rosata and Kulm, 1981]. The observed $300\text{--}400 \text{ m}$ thickness of the sediments is in agreement with results of recently drilled ODP Leg 202 site 1237 [Shipboard Scientific Party of Leg 202, 2002]. This sediment cover leads to a rather smooth topography of the southeastern flank of the Nazca Ridge, except where volcanic structures are located, compared to the rough relief of the surrounding Nazca Plate imaged by bathymetry north of the ridge [Bialas and Kukowski, 2000; Kukowski et al., in prep.].

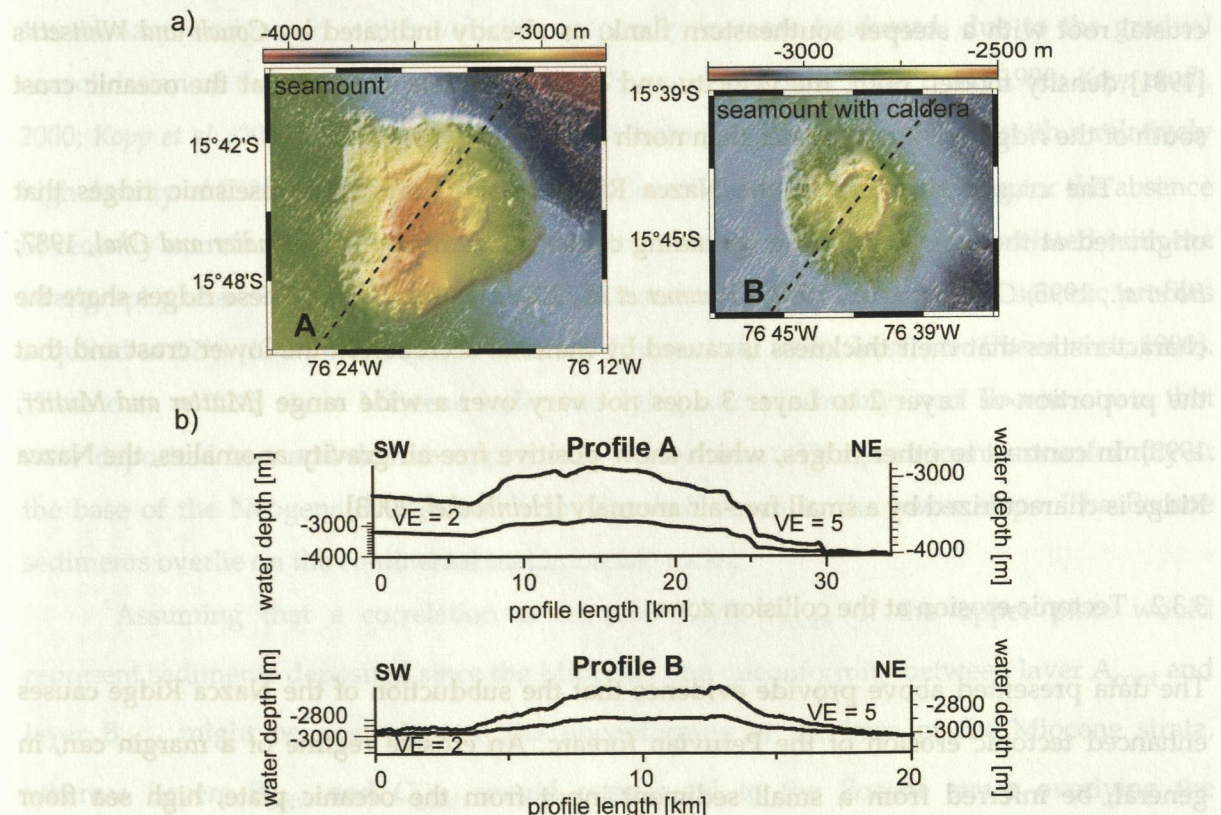


Figure 3.13: a) Detail bathymetric maps of prominent seamounts. b) Bathymetric profiles across the seamounts. For location of detail maps and profiles see Figure 3.2.

The structure of the volcanic edifices on the ridge flank may indicate a time lag between their formation and the formation of the main body of the ridge, since they look quite intact, e.g. the seamount with the preserved caldera (Figure 3.13). An origin off the spreading center is supported by the chemical composition of samples dredged on the small ridge located in the southeast corner of the mapped area (Figure 3.2) [Hagen and Moberly, 1994]. The observation that the sediment cover on these features is smaller than in the vicinity may indicate that their tops, which are now located at water depths between 2500-3000 m, once were near or above the sea level.

The seismic velocities of the crustal layers, as derived from the wide-angle seismic data, are similar to those of normal oceanic crust [Kennett, 1982; Mutter and Mutter, 1993]. Thus the upper (B_{oc} , C_{oc} , D_{oc}) and lower (E_{oc} , F_{oc}) layers are interpreted to correspond to Layers 2A, 2B, 2C, 3A, and 3B of normal oceanic crust, respectively (see Figure 3.14). The maximum thickness of 17 km of the ridge crust is in excellent agreement with the value of 18 ± 3 km obtained by analysing earthquake waves [Woods and Okal, 1994] and a thickness of 15 km inferred by interpretation of gravity data [Couch and Whitsett, 1981]. More than half of the crustal thickness of the ridge is accommodated by the lower crustal layer (F_{oc}), in agreement with observations at aseismic ridges worldwide [Mutter and Mutter, 1993]. Furthermore, the wide-angle seismic data constrain the presence of a slightly asymmetric crustal root with a steeper southeastern flank, as already indicated by Couch and Whitsett's [1981] density model. Both, the velocity and density models suggest that the oceanic crust south of the ridge is 1-2 km thinner than north of it.

The crustal structure of the Nazca Ridge is similar to other aseismic ridges that originated at the intersection of a spreading center and a hot spot [Talandier and Okal, 1987; Ito et al., 1995; Corrigan et al., 1990; Trummer et al., 2002; Walther, 2002]. These ridges share the characteristics that their thickness is caused by material accretion in the lower crust and that the proportion of Layer 2 to Layer 3 does not vary over a wide range [Mutter and Mutter, 1993]. In contrast to other ridges, which show positive free-air gravity anomalies, the Nazca Ridge is characterized by a small free-air anomaly [Heinbockel, 2003].

3.3.2 Tectonic erosion at the collision zone

The data presented above provide evidence that the subduction of the Nazca Ridge causes enhanced tectonic erosion of the Peruvian forearc. An erosive regime of a margin can, in general, be inferred from a small sediment input from the oceanic plate, high sea floor roughness, a large taper, high basal friction, a characteristic morphology and internal structure of the forearc [Scholl et al., 1980; Hilde, 1983; Cloos and Shreve, 1988a,b; Moore et al.,

1986; Ballance et al., 1989; von Huene and Lallemand, 1990; von Huene and Scholl, 1991; Lallemand et al., 1992; Lallemand et al., 1994; von Huene et al., 1994; Clift and MacLeod, 1999; von Huene et al., 1999; Vannucchi et al., 2001]. At erosive margins, in general, the slope of the upper plate is steep, irregular and cut by numerous canyons and gullies indicating surface erosion, while the trench may be filled with debris from slumping [Ranero and von Huene, 2000; Vanneste and Larter, 2002; Adam et al., submitted]. In contrast to accretive margins, the slope at erosive margins is characterized by the lack of actively growing thrust ridges extending several tens to hundreds kilometers along strike. In the following, the features indicative of ongoing tectonic erosion at the collision zone of the Nazca Ridge are discussed.

The important prerequisite of little sediment input is given at the Nazca Ridge, with the sedimentary cover not exceeding 400 m thickness. The lack of a thick sedimentary cover contributes to a high sea floor roughness, which is further intensified by the presence of seamounts and volcanic ridges. Accretive margins such as for example Makran, Cascadia or Nankai show a several kilometers thick pile of sediments on the downgoing plate [Platt, 1985; Davis and Hyndman, 1989; von Huene et al., 1994; Kukowski et al., 2001]. As revealed by the seismic data, the incoming sediments on the ridge are not accreted, but completely subducted. In the upper plate, the different layers of the velocity model show little lateral variation of the vertical velocity gradients. This is in contrast to similar velocity models for accretionary wedges, in which velocities generally increase landward, due to the gradual consolidation of the accreted sediments [von Huene et al., 1994; Flueh et al., 1998; Kopp et al., 2000; Kopp et al., 2002]. The density model of Heinbockel [2003] shows rocks with a relatively high density of 2520-2660 kg/m³ 700-1000 m below the sea floor, also arguing for the absence of recently accreted sediments. The layers of the velocity model may be correlated with the stratigraphy observed in cores of ODP Leg 112 and to reflective horizons in seismic profiles acquired at 12°S [Kulm et al., 1981; Suess, von Huene et al., 1998; Suess, von Huene et al., 1990]. These data at 12°S show Miocene sediments lying unconformably over Eocene strata that were deposited in a mid-shelf to upper slope environment. This prominent unconformity at the base of the Neogene is observed from the shelf down to the lower slope. The Eocene sediments overlie on the continental metamorphic rocks.

Assuming that a correlation is feasible, Layer A_{cont} of the upper plate would represent sediments deposited since the Miocene. The unconformity between layer A_{cont} and layer B_{cont} might be equivalent to the unconformity at the base of the Miocene strata, whereas Layers B_{cont} and C_{cont} would correspond to the Eocene strata overlying the crystalline rocks (D_{cont}). This correlation implies that Eocene mid-shelf to upper slope sediments are located near the trench and that the crystalline core of the continental wedge

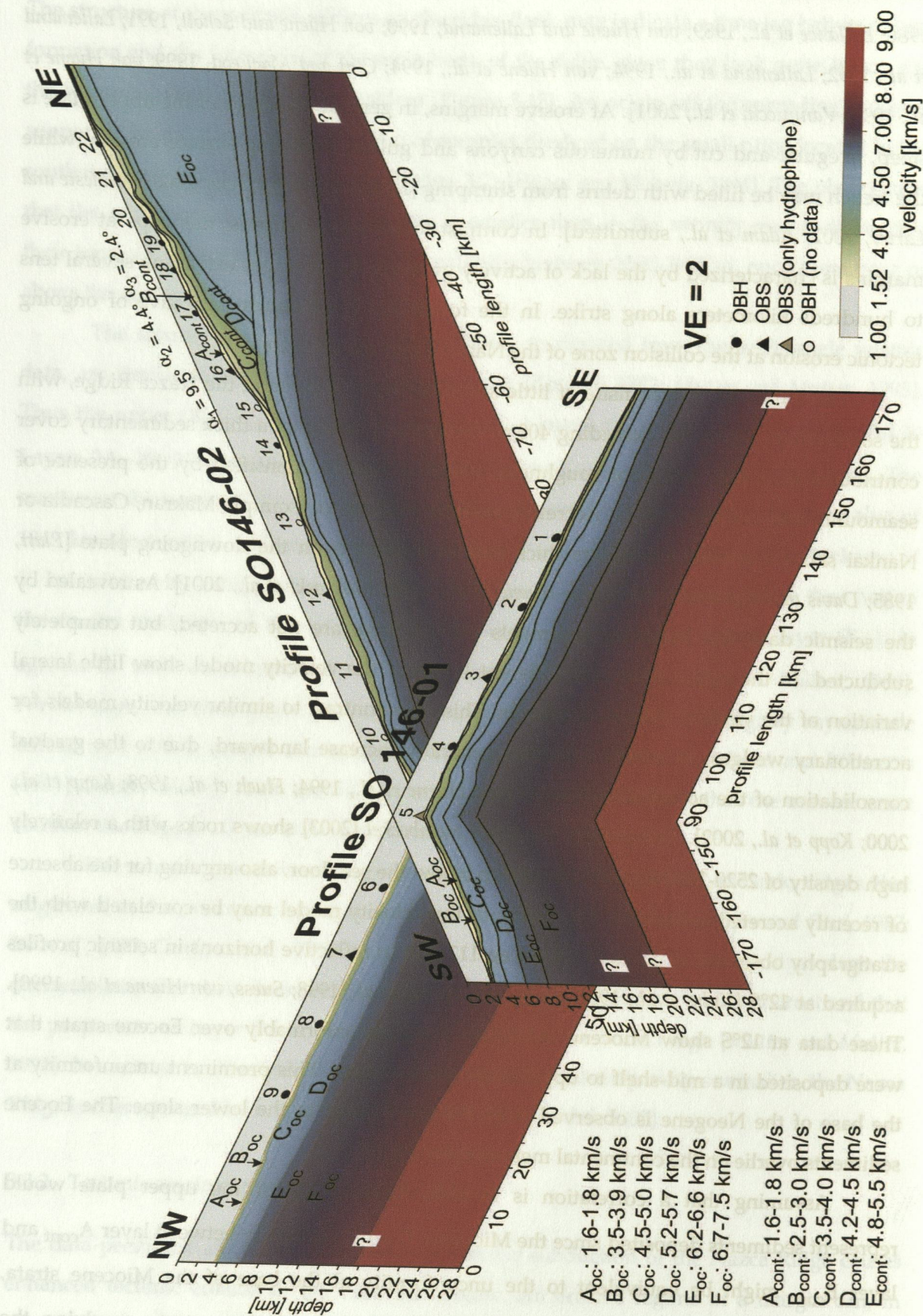


Figure 3.14: Velocity models for the wide-angle seismic profiles SO146-01 and SO146-02. Layers are correlated at station OBS05. For location of profiles see Figure 3.1.

may extend as far seaward as 15 km from the trench (Figure 3.14). This interpretation is in agreement with the observation that rocks of high density and seismic velocities are located a few kilometers away from the trench (Figures 3.14). The presence of these mid-shelf to upper slope sediments near the trench at few hundred meters depth below sea floor requires a much longer time period of tectonic erosion than 2 Ma, the time span since the onset of ridge subduction at 15°S, and thus, can be regarded as a diagnostic feature of a long-term erosive regime. It should be noted, however, that the correlation of drilled strata at 12°S and modelled layers at 15°S is not straightforward due to the distance of 500 km between the Nazca Ridge and the ODP sites. In addition, the forearc at the collision zone has recently been uplifted by 1-2 km compared to the location of the drilling sites.

Another argument supporting an erosive regime is provided by the observation that a re-entrant as wide as the Nazca Ridge is absent at the collision zone. How deep a ridge indents a forearc, may depend on the mechanical strength of the material of the continental wedge that, in turn, may be linked to the mass transfer regime. The rocks of high seismic velocities and densities, which are present close to the trench, are likely to be mechanically strong. We envision that the strength of these rocks has prohibited a deep indentation of the wedge by the ridge. A comparison with other margins experiencing ridge subduction shows that deep re-entrants develop preferentially in settings where ridges migrate along accretionary prisms composed of mechanically weak rocks. [McCann and Habermann, 1989; Bouysse and Westercamp, 1990; Schnuerle *et al.*, 1998; Dominguez *et al.*, 1998]. In contrast, the subduction of the Carnegie and Cocos Ridges at the erosive Ecuadorian and Costa Rican continental margins, respectively, does not lead to a significant indentation of the forearcs [McCann and Habermann, 1989; Corrigan *et al.*, 1990; Gutscher *et al.*, 1999]. At the Louisville Ridge, a chain of seamounts subducting at the Tonga subduction zone, the largest arcward displacement of the plate boundary is observed at the northern edge of the southward-migrating collision zone [Vogt, 1976; McCann and Habermann, 1989; Ballance *et al.*, 1989; Lallemand *et al.*, 1994]. In conclusion, the Peruvian margin is similar to the Ecuadorian and Costa Rican subduction zones. Off Peru, re-entrants of much smaller scale may be produced by the seamounts and volcanic ridges located on the ridge when they collide with the upper plate. Such a small volcanic feature may have caused the 20 km wide marginward deflection of the lower slope (Figure 3.15).

The geometry of the two 10-15 km long, nearly trench-parallel ridges, located at the intersection of the ridge crest with the trench (Figure 3.7a, 3.15), suggests that they formed by thrusting [Schweller *et al.*, 1981]. The ridges, which apparently developed in the calcareous sediments on the ridge, are exclusively found near the ridge crest. Such ridges may provide

an explanation for the locally limited material transfer from the Nazca Ridge to the inner trench wall, as inferred from cores drilled into the lowermost slope opposite to the thrust ridges (Figure 3.15) [Kulm *et al.*, 1974; Rosata and Kulm, 1981]. The cores contain calcareous ooze from the Nazca Ridge as exotic minor constituent, which has been incorporated within the last 400,000 a into the terrigenous turbidites and hemipelagic mud of the frontal wedge [Kulm *et al.*, 1974; Rosata and Kulm, 1981]. Another explanation for this locally limited thrusting may be that the lower slope is steepest opposite to the ridge crest, increasing the material flux into the trench and thus its sediment fill. The presence of a locally thicker sediment fill may trigger the creation of the thrusts. We speculate that the thrust ridges are transient features and the sediments will eventually be dragged beneath the continental wedge (Figures 3.7a). Such underthrusting of erosional debris is known to be a characteristic mass transfer mode at erosive margins [Scholl *et al.*, 1980; Cloos and Shreve, 1988a,b; von Huene and Lallemand, 1990; Lallemand *et al.*, 1994; Vanneste and Larter, 2002].

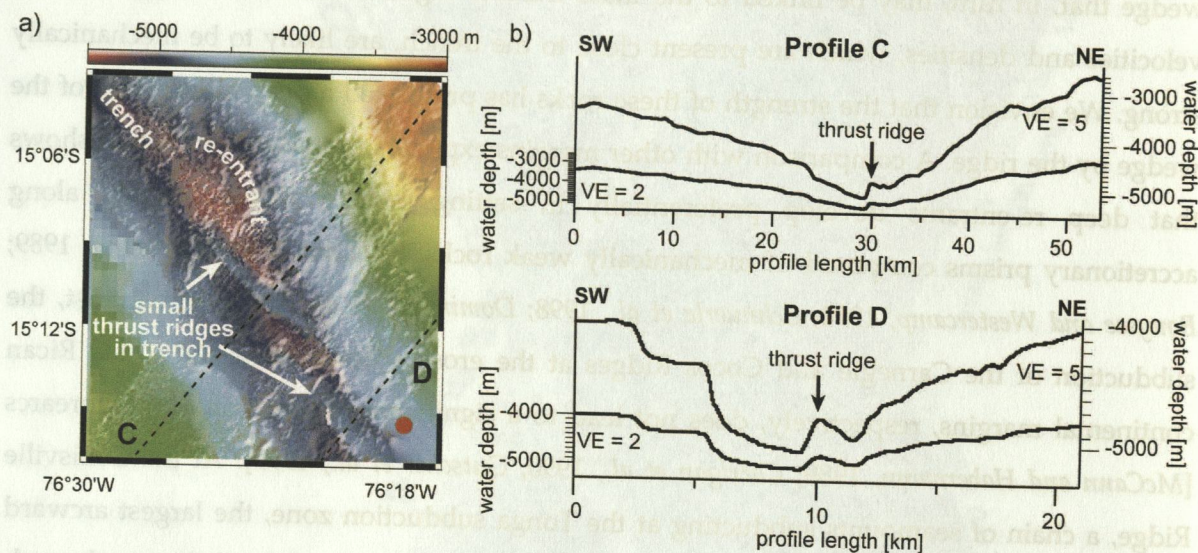


Figure 3.15: a) Bathymetric map of the trench where the ridge crest enters the subduction zone. Red dot marks drilled sites after Kulm *et al.* [1974]. b) Bathymetric profiles of thrust ridges in the trench axis. For location of detail map and profiles see Figure 3.2.

A comparison with the forearc systems north of the Nazca Ridge [Kukowski *et al.*, in prep.; Krabbenhoft *et al.*, in prep.] shows that both, the angle of the lower slope and the taper are largest at 15°S. The geological record at 9°S, where the ridge did not affect the margin, differs significantly from 11.5°S, where the ridge crest passed 9.5 Ma ago [Hampel, 2002], and the present collision zone at 15°S. While the margin at 9°S has subsided more than 1000 m for 12–13 Ma, the region at 11.5°S has undergone a phase of uplift and enhanced tectonic erosion during 11–7 Ma with subsequent subsidence of more than several hundred meters for 6 Ma [von Huene *et al.*, 1988; von Huene and Lallemand, 1990; Clift *et al.*, in press]. Erosion rates

derived from subsidence reconstruction for the Lima Basin at 11.5°S show a rate 10 times higher during and shortly after the passage of the Nazca Ridge than before [Clift *et al.*, in press].

Based on these lines of argument, we suggest that tectonic erosion at the collision zone is more intense than off Central Peru and that this observation can be attributed to the passage of the Nazca Ridge. Furthermore, we speculate that long-term tectonic erosion was already prevailing before the ridge arrived. A look at the regions south of the Nazca Ridge would help to support this idea, however, little data are available off the adjacent Arica Bight [Coulburn, 1981]. However, it is known that the geodynamic boundary conditions do not change significantly around the Arica Bight, in particular, that the sediment cover on the Nazca Plate is as small as off Peru and North Chile [von Huene *et al.*, 1999; Adam and Reuther, 2000]. We propose that the geodynamic setting of the South Peruvian margin prior to the subduction of the ridge was similar to the well-documented long-term erosion at the North Chilean margin [von Huene *et al.*, 1999; Adam and Reuther, 2000]. In other words, the subduction of the Nazca Ridge causes enhanced, short-term tectonic erosion that is superposed on a long-term erosive regime.

3.4 Conclusions

The GEOPECO geophysical survey revealed that the crust of the Nazca Ridge is built by layers of seismic velocities similar to normal oceanic crust. Due to a considerably thicker Layer 3, the total crustal thickness of the ridge is about 17 km. The relative proportion of Layer 2 to Layer 3 is in agreement with observations from other aseismic ridges worldwide, formed at the intersection of spreading centers and hotspots.

The collision zone of the Nazca Ridge at 15°S shows characteristics of a margin undergoing tectonic erosion, which include, among others, a small sediment input, a large taper of the continental wedge indicating high basal friction, and the presence of rocks with high seismic velocities and densities near the trench. Correlation of modelled layers from a well constrained velocity model with ODP Leg 112 stratigraphy north of the ridge suggests, that shelf deposits and the crystalline part of the continental wedge extend close to the trench. The presence of mechanically strong material extending almost to the trench is able to explain why the subduction of the ridge does not lead to a marginward deflection of the trench. We propose that the tectonic erosion caused by the Nazca Ridge intensifies a long-term erosive regime, inferred for southern Peru by a comparison with the Central Peruvian margin.

4 Analogue and numerical modelling of ridge subduction

The geophysical data acquired during the RV Sonne cruise SO146-GEOPECO tightly constrain the morphology, the crustal structure, the style of faulting and the physical properties of the Peruvian margin at the collision zone with the Nazca Ridge. They provide a snapshot in time of an erosive margin undergoing ridge subduction. In order to gain insight into the temporal sequence of the deformation processes during and after the collision, analogue and numerical simulation techniques have been applied. These two different approaches are complementary as each of them throws light on specific aspects of ridge subduction.

The analogue experiments have been carried out at the Geodynamic Laboratory of the GFZ Potsdam and were the first 3D experiments monitored by the recently installed Particle Imaging Velocimetry (PIV) system. The sandbox experiments have been designed to model the influence of a ridge colliding with an erosive continental margin. Their three-dimensional set-up accounts for the oblique convergence of the Nazca plate, which results in trench-parallel motion of the Nazca Ridge. The analogue models aim at getting insights into the temporal evolution of the margin during ridge subduction, the mass transfer regime, the development of faults, as well as the amount and localisation of forearc uplift. Section 4.1 presents the concepts of analogue modelling, the realization of the experiments as well as a discussion the results.

Numerical modelling has applied the Finite-Elements method using the commercial software ABAQUS by Hibbitt, Karlsson and Sorensen Inc. (section 4.2). Information on the crustal thickness and the densities of ridge and upper plate obtained by the SO146-GEOPECO cruise has been incorporated into the models. 2D numerical models have been used to calculate the amount of isostatic uplift of the forearc. Furthermore, 3D models have been designed to yield the displacement field and stress distribution in the upper plate above the obliquely subducting, laterally migrating ridge. Section 4.2 describes the Finite-Element method, the design and performance of the models and finally discusses the results.

4.1 Analogue modelling

4.1.1 The critical taper theory and its application to sandbox models

The mechanics of accretionary prisms at convergent margins has been described in terms of the critical taper theory that considers natural wedges to be analogous to wedges of sand or snow that form in front of a moving bulldozer (Figure 4.1) [Chapple, 1978; Dahlen, 1984; Davis and Dahlen, 1989, Dahlen, 1990]. Such wedges grow by internal deformation until they reach their critical taper, which is the angle between the surface slope and the basal plane called decollement (Figure 4.1). After attaining the critical taper, the wedge slides stably along the decollement and is everywhere at the verge of shear failure [Davis *et al.*, 1983].

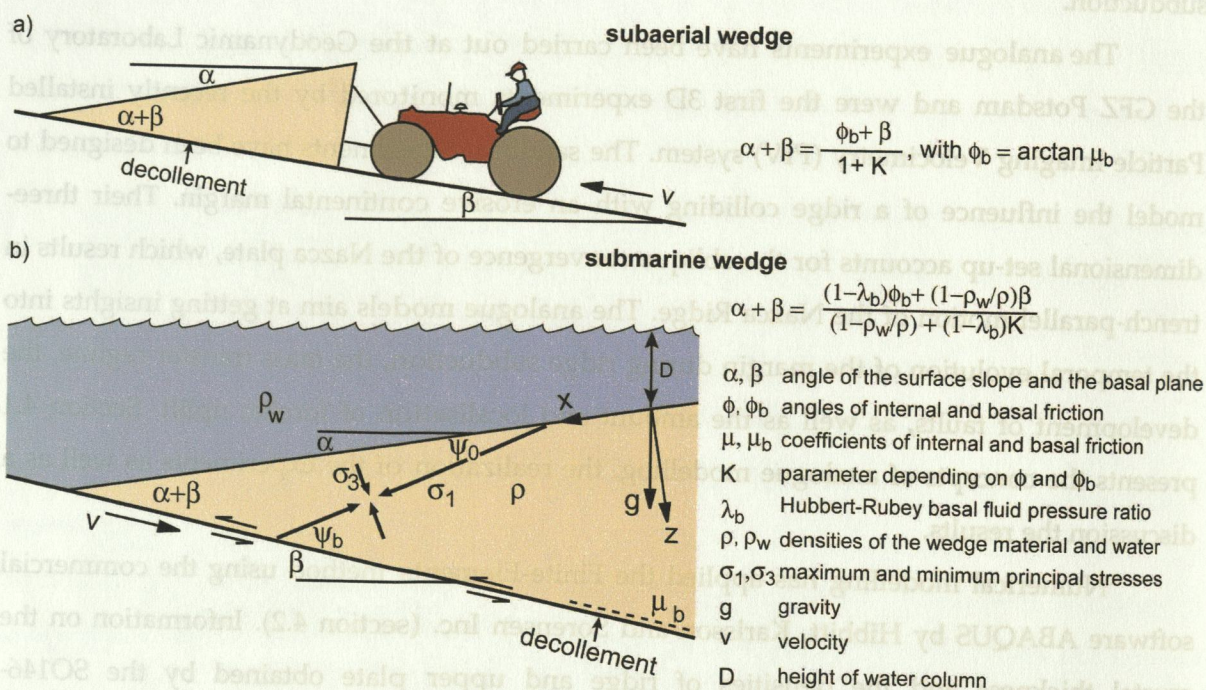


Figure 4.1: a) The growth of an accretionary wedge is equivalent to a self-similarly growing prism of sand or snow in front of a moving bulldozer. The wedge grows by internal deformation, until the critical taper is reached. The critical taper equals the sum of the angles α and β of the surface slope and the basal plane, respectively. It is related to material-dependent frictional properties and, in case of a submarine prism (b), on the basal fluid pressure ratio, and on the density contrast between water and the wedge material (after Davis *et al.* [1983]).

The critical taper theory assumes a Mohr-Coulomb rheology, i.e. the material shows a pressure-dependent, strain-rate-independent brittle behaviour [Davis *et al.*, 1983]. The Coulomb failure criterion in the absence of pore fluids is

$$|\tau| = C + \mu (\sigma_n),$$

where τ is the shear stress, C the cohesion, μ the coefficient of internal friction and σ_n the normal stress. The coefficient of internal friction μ and the angle of internal friction ϕ are

related by

$$\mu = \tan \phi$$

Accordingly, the coefficient of the basal friction μ_b is defined by $\mu_b = \tan \phi_b$, with ϕ_b being the angle of basal friction.

The fundamental equation of the critical taper for non-cohesive Coulomb wedges is

$$\alpha + \beta = \Psi_b - \Psi_0,$$

where the right-hand side describes the difference between the orientation of the maximum principal stress σ_1 with respect to the basal plane (Ψ_b) and the surface slope (Ψ_0) (Figure 4.1). The orientation of the principles stresses is assumed to be constant everywhere in the wedge. The above equation relates the taper $\alpha + \beta$ to the mechanical properties of wedge and basal plane, since the angles Ψ_b and Ψ_0 depend on the angle of basal friction ϕ_b on the decollement. Substituting $\Psi_b - \Psi_0$ by expressions containing only ϕ_b and ϕ , the critical taper of a subaerial wedge consisting of cohesionless material can be written as

$$\alpha + \beta = \frac{\phi_b + \beta}{1 + K}$$

where K is a function of the internal and basal coefficients of friction.

In the case of a submarine wedge, the density contrast between water (ρ_w) and the wedge material (ρ) as well as the dimensionless basal fluid pressure ratio λ_b [Hubbert and Rubey, 1959] that relates the basal pore fluid pressure p_f^b to the effective stress σ_z under consideration of the overlying water column of height D by

$$\lambda_b = \frac{p_f^b - \rho_w g D}{|\sigma_z| - \rho_w g D}$$

have to be considered (Figure 4.1b) [Dahlen, 1984]. Thus, the equation of the critical taper becomes

$$\alpha + \beta = \frac{(1 - \lambda_b)\phi_b + (1 - \rho_w / \rho)\beta}{(1 - \rho_w / \rho) + (1 - \lambda_b)K}$$

The relationship between the frictional properties and the resulting taper of the wedge has been illustrated by taper stability diagrams (Figure 4.2) [Dahlen, 1984].

Critically tapered wedges are in a state of dynamic equilibrium, which the wedge tries to maintain under changing material influx. If material is added to the wedge, it

continues to grow self-similarly, i.e. independent of the length scale, with the taper remaining constant. The influx of the new material is compensated by internal deformation during ongoing stable sliding. A wedge of a less than critical taper first adjusts by internal deformation and steepening of its slope before it slides stably (Figure 4.2). In the opposite case of an over-critical taper, the wedge adjusts by extensional failure [Dahlen, 1984]. The critical taper theory can also be used to explain the mechanics of wedges undergoing subduction erosion and extensional failure [Dahlen, 1984; Adam *et al.*, submitted]. Basal erosion may occur if there is no contrast between the basal and internal shear strength, i.e. at the stability limit of the wedge. Under this condition, which is most likely found beneath the frontal part of a wedge, a new detachment forms within the wedge, and material beneath is dragged into the subduction channel [Lohrmann, 2002; Adam *et al.*, submitted].

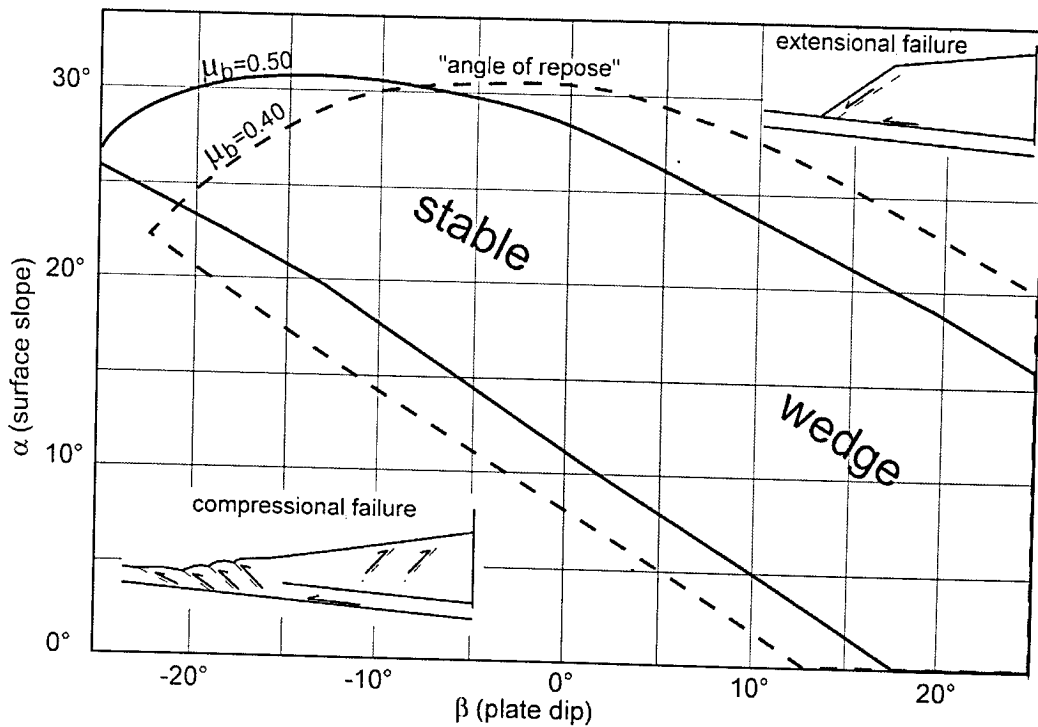


Figure 4.2: Typical taper stability field for a given wedge with basal friction coefficients $\mu_b = 0.5$ and $\mu_b = 0.4$. Below the critical taper (lower left corner), the wedge tries to reach the critical taper by internal deformation. If the taper is over-critical (upper right corner), extensional failure occurs. The angle of repose is the largest possible angle of the surface slope (modified after Dahlen [1984]).

The scale-independence of the critical taper theory lays the foundation to investigate the behaviour of wedges by analogue models in the laboratory. In order to be directly comparable to natural settings, the experiment and the analogue material are scaled in length units, density and frictional properties, respectively [Hubbert, 1937; Schellart, 2000]. The scaling factor of the models carried out under normal gravity can be calculated by $[C/\rho g]_{\text{nature}}/[C/\rho g]_{\text{model}}$ [Hubbert, 1937; Koyi, 1997; Schellart, 2000]. An analogue material

with a deformation behaviour similar to brittle crustal rocks is sand. Sand shows an elasto-plastic rheology with strain hardening and softening before and after failure, respectively, before stable sliding under constant frictional conditions is achieved [Mandl, 1988; Byerlee, 1978; Marone, 1998; Krantz, 1991; Schellart, 2000]. Both, sand and upper crustal rocks tend to localize deformation, i.e. the frictional strength along faults is reduced compared to the undeformed material [Byerlee, 1978].

Over the past decades, sandbox experiments have successfully been applied to model the mechanics of frontal wedges at convergent margins. The approach proved to be suitable to study the influence of different taper stability configurations on the growth of accretionary prisms [e.g. Mulugeta, 1988; Mulugeta and Koyi, 1992; Koyi, 1997, Davis and Dahlen, 1983; Dahlen, 1990; Liu *et al.*, 1992; Kukowski *et al.*, 1994]. Experiment series systematically investigated how accretionary wedges behave in case of high or low basal friction, variable influx and outflux of material, as well as in the presence of a deformable backstop or a weak layer within the incoming material [Kukowski *et al.*, 1994; Gutscher *et al.*, 1996; Gutscher *et al.*, 1998; Kukowski *et al.*, 2002]. Other experiments simulated ridge or seamount subduction at accretive margins [Lallemand *et al.*, 1992; Dominguez *et al.*, 1998] or investigated the effects of pore fluids, surface erosion or sedimentation acting on the growing wedge [Storti and McClay, 1995; Cobbold and Castro, 1999; Cobbold *et al.*, 2001; Persson and Sokoutis, 2002; Marques and Cobbold, 2002]. Recent experiments designed to study the mechanics of erosive margins show the important role of low sediment input and high basal roughness of the subducting plate in establishing a steady-state erosive regime [Lallemand *et al.*, 1994; Lohrmann, 2002; Lohrmann *et al.*, in press; Adam *et al.*, submitted].

4.1.2 The physical properties of the analogue material

Scaling of the sandbox experiments to natural settings requires the measurement of the frictional properties of the analogue material. The frictional strength of the material is defined by the peak friction for the undeformed material, the static-stable friction for the strength of previously deformed material and the dynamic-stable friction for the strength of active shear zones (Figure 4.3) [Byerlee, 1978]. While the peak friction controls the initiation of a shear zone, the static stable friction controls its reactivation.

A ring shear apparatus is used to measure the peak, static-stable and dynamic-stable frictions of the analogue material (Figure 4.4). During a measurement set, normal loads between 1-12 kg are applied to the ring shear apparatus. These loads are of the same order of magnitude as the loads the material experiences during an experiment. In the first loading cycle, the shear box is set rotating and a connected PC records the occurring shear forces. In a

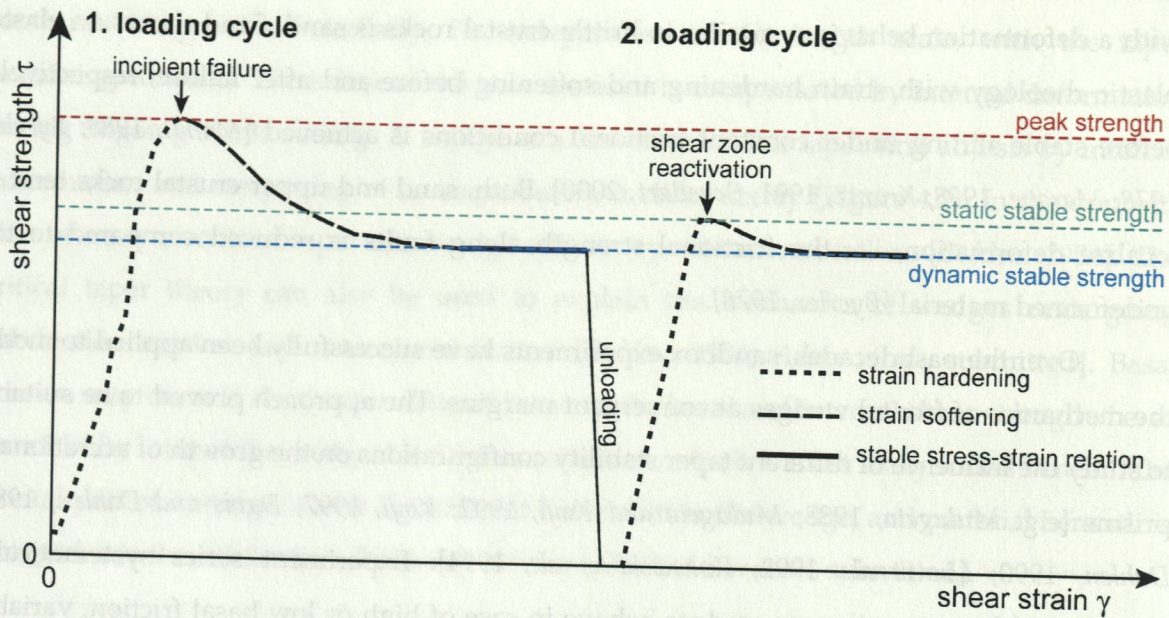


Figure 4.3: Characteristic stress-strain curve for analogue materials (after Adam *et al.* [submitted]).

following unloading phase, the rotation direction is reversed until the shear strength drops to zero. At this moment, the rotation direction is again reversed for a second loading cycle, in which the shear zone is re-activated. This whole procedure is carried out three times to assess the error of the measured values. Since the preparation method of the material, i.e. sifted or poured, influences the behaviour during deformation in the experiment [Lohrmann *et al.*, in press], the measurements are performed for both types of preparation. Friction coefficients and cohesion are calculated by linear regression (Figures 4.4b, 4.5).

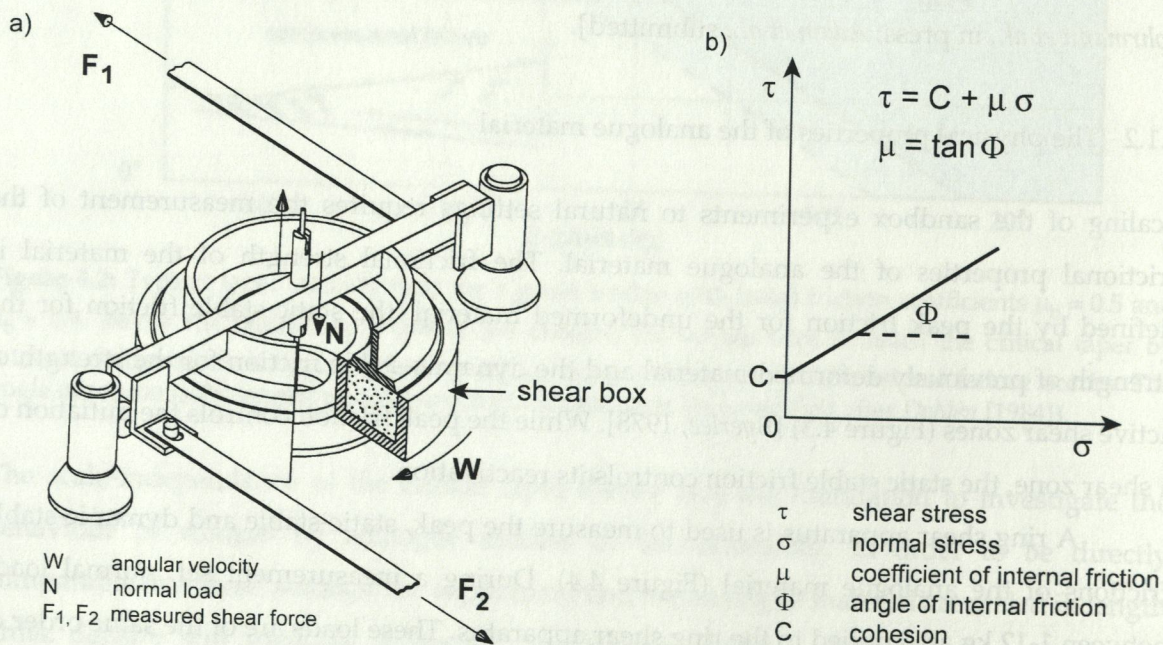


Figure 4.4: a) Set-up of the ring shear device used to measure the frictional strength and the cohesion of the analogue material. b) Relation between shear and normal stresses from which internal friction and cohesion can be determined by linear regression.

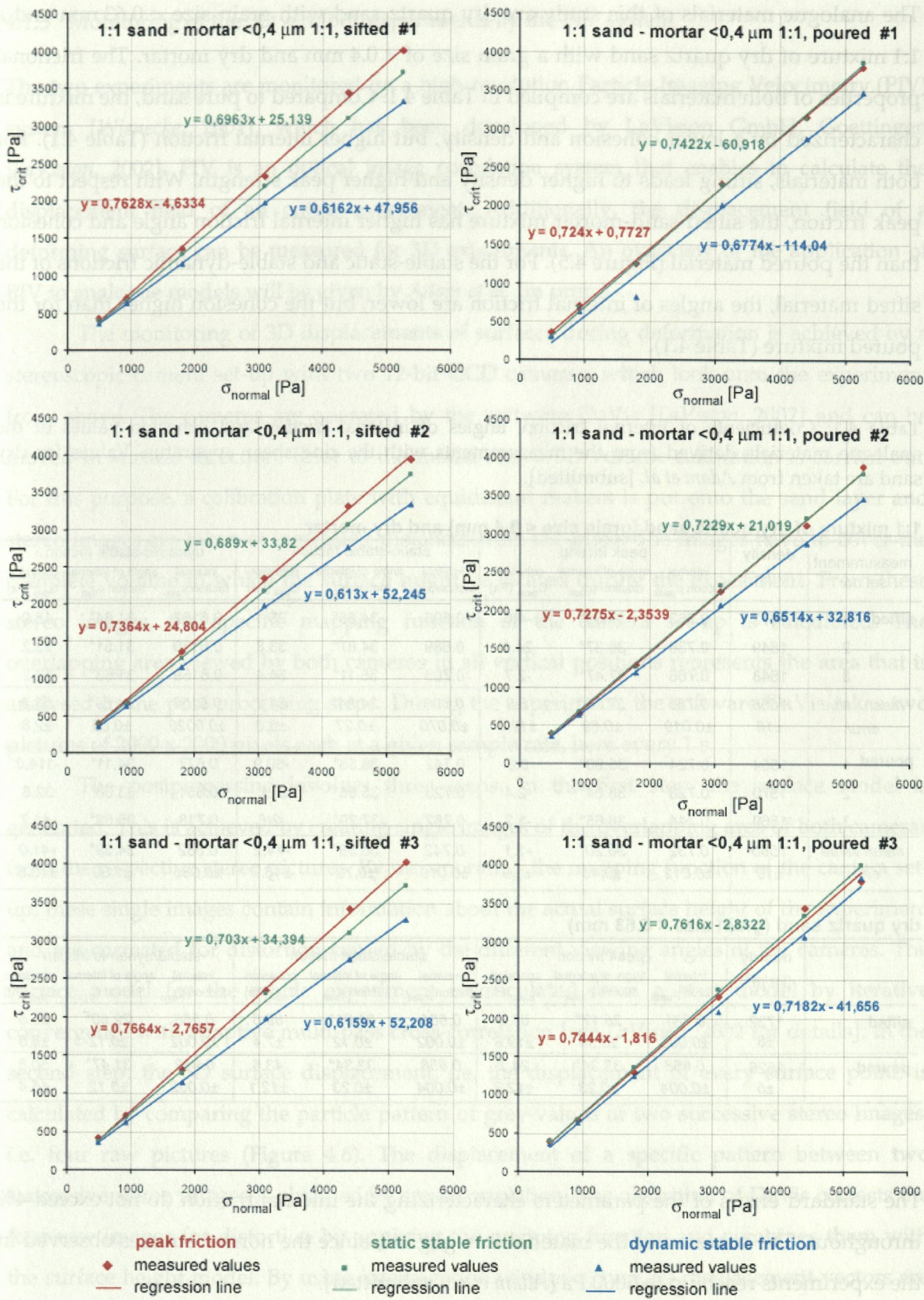


Figure 4.5: Plots showing the experimental results obtained for the frictional properties of the sifted and poured sand-mortar-mixtures in the left and right column, respectively (see Table 4.1 for numerical values).

The analogue materials of this study are dry quartz sand with grain size < 0.63 mm and a 1:1 mixture of dry quartz sand with a grain size of < 0.4 mm and dry mortar. The frictional properties of both materials are compiled in Table 4.1. Compared to pure sand, the mixture is characterized by a lower cohesion and density, but higher internal friction (Table 4.1). For both materials, sifting leads to higher density and higher peak strength. With respect to the peak friction, the sifted sand-mortar mixture has higher internal friction angle and cohesion than the poured material (Figure 4.5). For the stable-static and stable-dynamic frictions of the sifted material, the angles of internal friction are lower, but the cohesion higher than for the poured mixture (Table 4.1).

Table 4.1: Coefficients of internal friction, angles of internal friction and cohesion values of the analogue materials derived from the measurements with the ring shear apparatus. Values for dry sand are taken from *Adam et al.* [submitted].

1:1 mixture of dry quartz sand (grain size < 0.4 mm) and dry mortar

measurement set no.	density [kg/m ³]	peak friction			static-stable friction			dynamic-stable friction			
		internal friction μ_{peak}	angle of internal friction ϕ_{peak}	cohesion C_{peak} [Pa]	internal friction μ_{stat}	angle of internal friction ϕ_{stat}	cohesion C_{stat} [Pa]	internal friction μ_{dyn}	angle of internal friction ϕ_{dyn}	cohesion C_{dyn} [Pa]	
sifted	1	1672	0.763	37.34°	-4.6	0.696	34.85°	25.1	0.6162	31.64°	48.0
	2	1649	0.736	36.37°	24.8	0.689	34.87°	33.8	0.6130	31.51°	52.2
	3	1648	0.766	37.47°	-2.7	0.703	35.11°	34.4	0.6159	31.63°	52.2
mean value	1656	0.755	37.06°	5.8	0.696	34.84°	31.1	0.6150	31.59°	50.8	
error	±16	±0.019	±0.69	±19.0	±0.070	±0.27	±6.0	±0.0020	±0.09	±2.8	
poured	1	1554	0.724	35.90°	0.8	0.742	36.58°	-60.9	0.677	34.11°	-114.0
	2	1570	0.728	36.04°	-2.4	0.723	35.86°	21.0	0.651	33.08°	32.8
	3	1569	0.744	36.65°	-1.2	0.762	37.29°	-2.8	0.718	35.69°	-41.7
mean value	1560	0.732	36.20°	-1.1	0.742	36.58°	-14.2	0.682	34.29°	-41.0	
error	±10	±0.012	±0.46	±1.9	±0.019	±0.72	±46.7	±0.036	±1.39	±73.8	

dry quartz sand (grain size < 0.63 mm)

	density [kg/m ³]	peak friction			stable/static friction			stable/dynamic friction		
		internal friction μ_{peak}	angle of internal friction ϕ_{peak}	cohesion C_{peak} [Pa]	internal friction μ_{stat}	angle of internal friction ϕ_{stat}	cohesion C_{stat} [Pa]	internal friction μ_{dyn}	angle of internal friction ϕ_{dyn}	cohesion C_{dyn} [Pa]
sifted	1732 ±8	0.731 ±0.006	36.17° ±0.34	63.5 ±19.8	0.601 ±0.002	31.01° ±0.12	89.6 ±7.4	0.568 ±0.002	29.60° ±0.12	66.5 ±5.0
poured	1526 ±5	0.658 ±0.004	33.34° ±0.23	24.2 ±12.3	0.658 ±0.004	33.34° ±0.23	43.6 ±12.1	0.612 ±0.002	31.47° ±0.12	50.8 ±5.4

The standard errors of the parameters characterizing the internal friction do not exceed 4% throughout. The cohesion of the material is negligible, since the normal stresses observed in the experiments reach up to 6000 Pa [*Adam et al.*, submitted].

Inserting the mean cohesion and density values of the analogue and natural materials into the relationship $[C/\rho g]_{\text{nature}}/[C/\rho g]_{\text{model}}$ [*Hubbert, 1937; Koyi, 1997; Schellart, 2000*] yields a scaling factor of $\sim 10^5$ for the experiment. This means that 1 cm in the experiment is equivalent to 1 km in nature.

4.1.3 Monitoring of the 3D sandbox experiments by the PIV system

The two experiments are monitored by a high-resolution Particle Imaging Velocimetry (PIV) system [Wienecke, 2001], which has been developed by LaVision GmbH, Goettingen [LaVision, 2002]. PIV is an optical image correlation system that enables to calculate the displacement field of an entire experiment. Additionally, the displacement field of a deforming surface can be measured for 3D experiments. An overview of the application of PIV to analogue models will be given by Adam *et al.* [in prep.]

The monitoring of 3D displacements of surfaces during deformation is achieved by a stereoscopic camera set-up with two 12-bit CCD cameras, which look onto the experiment from above. The cameras are operated by the software DaVis [LaVision, 2002] and can be moved in vertical direction. Prior to the model run, a 3D volume calibration is carried out. For this purpose, a calibration plate with equidistant markers is put onto the sand layer and stereo images are taken at increasing distances from the plate. The images have to cover the complete volume in which the surface might be located during the experiment. From these stereo images, the specific mapping function of the camera set-up is calculated. The overlapping area viewed by both cameras in all vertical positions represents the area that is analysed in the post-processing steps. During the experiment, the software DaVis takes two pictures of 2000 x 2000 pixels each at a given sample rate, here every 1 s.

The postprocessing involves three steps. In the first step, the surface model is generated. This is achieved by creating single images of the overlapping area of both cameras from the respective stereo pictures. By incorporating the mapping function of the camera set-up, these single images contain information about the actual surface height of the experiment and are corrected for distortion caused by the different viewing angles of the cameras. The surface model for the whole experiment is calculated from a start model by iterative convergence with adaptive multi-pass cross-correlation [see LaVision, 2002 for details]. In the second step, the 3D surface displacement, i.e. the displacement of every surface point, is calculated by comparing the particle pattern of grey-values of two successive stereo images, i.e. four raw pictures (Figure 4.6). The displacement of a specific pattern between two successive stereo images is obtained by cross-correlation. The algorithm of DaVis corrects the four raw images for distortion by applying the mapping function and combines them with the surface height model. By using interrogation windows, two 2D displacement vectors are computed for the two successive pictures of each camera (Figure 4.6) [LaVision, 2002]. From these two vectors, the 3D displacement vector of a specific surface point is determined. In an initial pass, the displacement field is calculated locally for the area in the interrogation window. The final displacement field of higher resolution is determined using an adaptive

multi-pass and iterations with decreasing interrogation window size. The last step includes post-processing and quality control of the calculated vector fields. DaVis offers numerous possibilities to display the calculated quantities of the experiment in 2D and 3D, e.g. the surface height, the velocity vector field, different velocity vector components and the motion of parts relative to each other. The output function allows exporting snapshots of the experiment and the PIV results as pictures and movies.

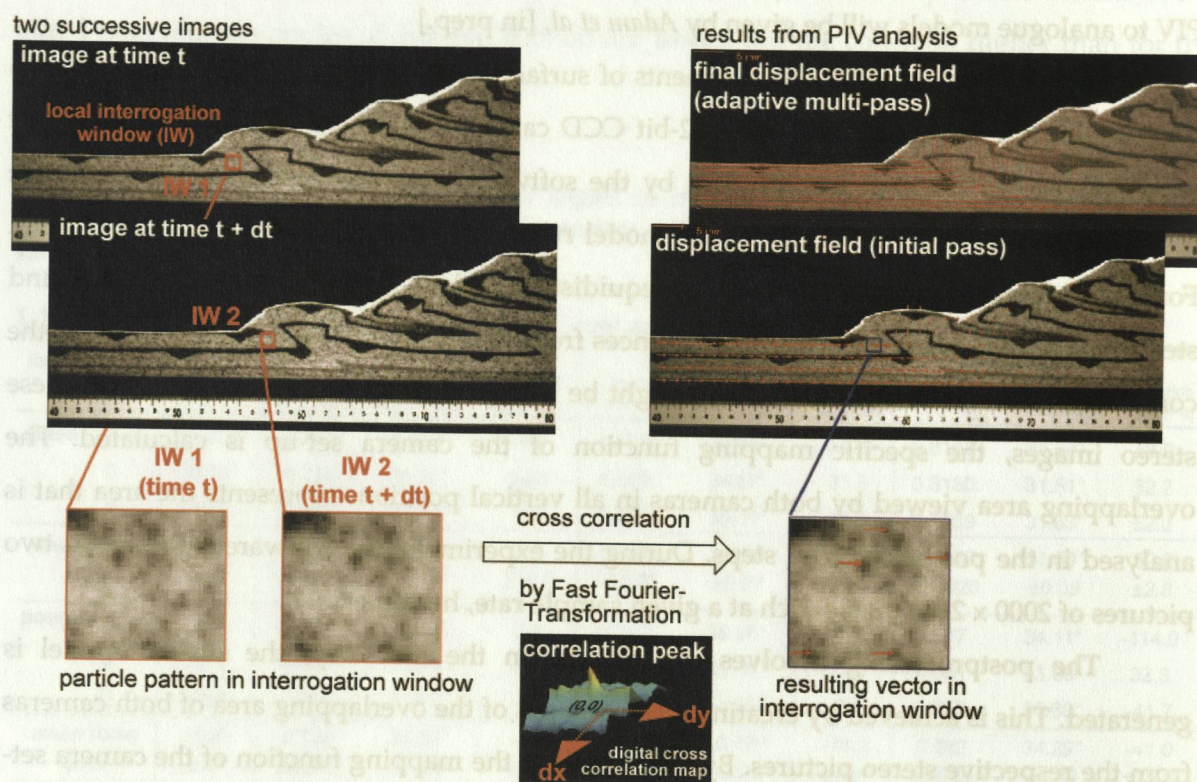


Figure 4.6: An example illustrating the computation of the displacement field for a 2D sandbox model by the Particle Imaging Velocimetry (PIV) system. The particle patterns in the interrogation window IW of two successive images are compared by cross-correlation. The displacement vector of the interrogation window is derived from the peak in the cross-correlation map. In this example, the particles moved to the right (after Adam *et al.* [in prep.]).

The maximum temporal resolution is limited by the image transfer rate of the digital cameras at ~ 15 Hz. Reducing the convergence velocity in the experiment can increase the resolution. The spatial resolution of the PIV system is determined by the distance of the cameras from the imaged object, since the optical resolution of the cameras is fixed at 2000×2000 pixels. The accuracy of the vector length is better than 0.1 pixel [LaVision, 2002], which translates into a resolution of 0.38 mm in the experiments of this study. Apart from that, the resolution of the displacement paths of particles depends on the ability of the cross-correlation algorithm to trace particle patterns through successive images. Therefore, particles of different grey-values must not move too fast in the time interval between two successive

images. The successful imaging of slumping events (section 4.1.5) demonstrates that the system is robust in tracing even fast moving particles.

4.1.4 Set-up and concept of the 3D sandbox experiments

The experimental apparatus consists of a fixed horizontal plate on which a conveyor belt is dragged underneath a rigid backwall, representing the subducting oceanic plate and the undeformable part of the continental margin, respectively (Figure 4.7). The conveyor belt is driven by an electric motor at known velocity. It should be noted, however, that the governing equations for the state of a Mohr-Coulomb wedge are independent of the convergence velocity. A glass panel bounds one side of the sandbox; the other is open to allow lateral material transfer parallel to the rigid backwall. The angle between the backwall

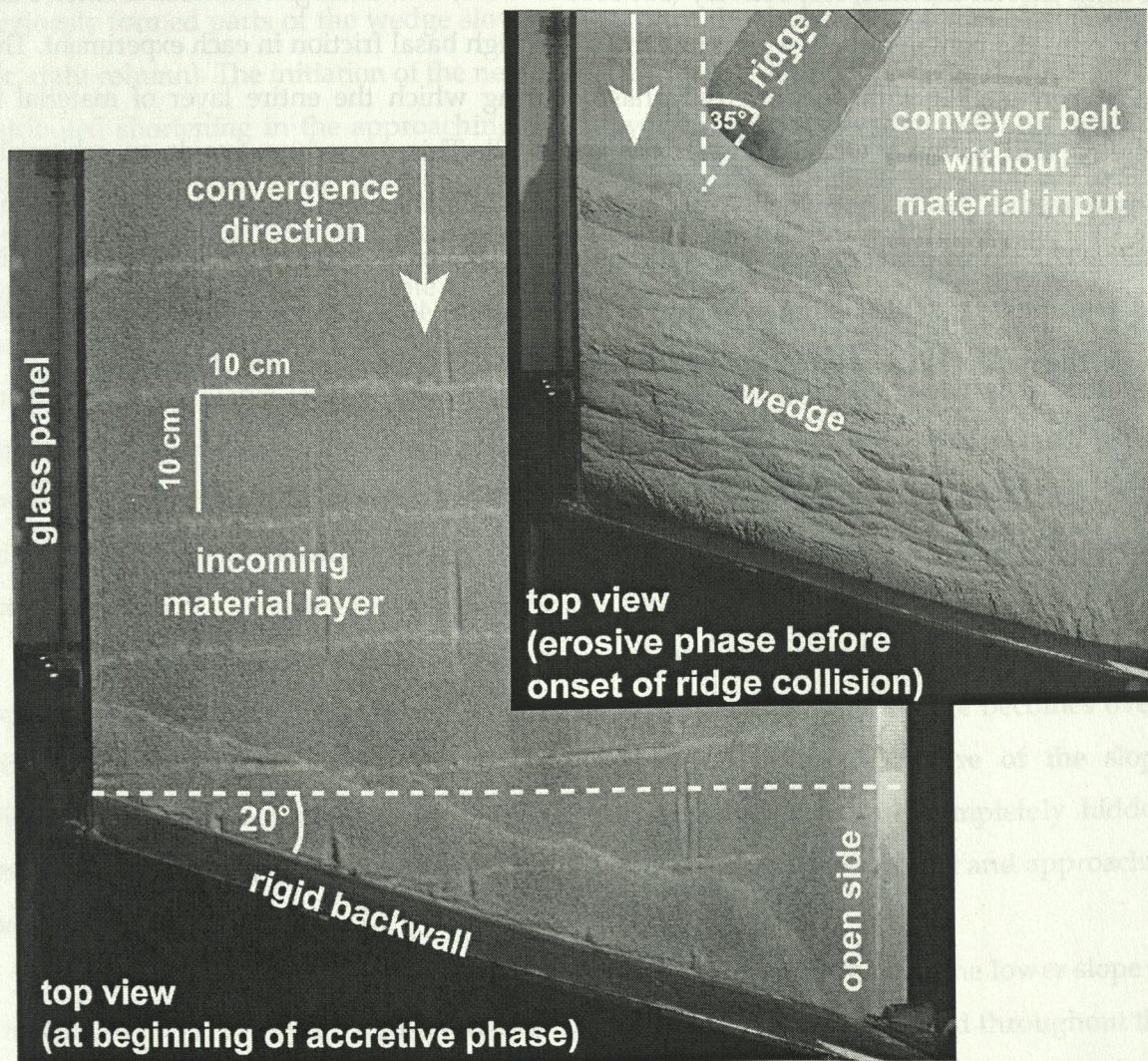


Figure 4.7: Set-up of the 3D sandbox experiment apparatus with 20° obliquity, high basal friction and no material outflux. The incoming material layer is 3 cm thick. In a first phase, the entire material layer is accreted and builds a wedge. After ~120 cm of convergence, the material input ceases and the erosive phase begins, during which the model ridge approaches the wedge.

and the normal on the glass panel is set to 20° according to the natural configuration off Peru (see Figure 4.7). The rigid backwall does not allow outflux of the material. The conveyor belt is formed by an adhesive foil with sprinkled sand and has a high basal friction with $\mu_b = 0.6$ relative to sifted sand [Adam *et al.*, submitted]. This agrees with the value inferred for the Peruvian margin [Davis *et al.*, 1983; Kukowski *et al.*, 1994]. A 15 cm wide and 3 cm high ridge made of modelling clay and sprinkled with sand is put onto foil with an orientation of 35° to the motion direction of the conveyor belt. It should be noted that the model ridge is not scaled to the dimensions of the Nazca Ridge, but made twice higher to exaggerate the observed effect to achieve a better spatial resolution with the monitoring system (see section 4.1.3). Despite a height of 3 cm, the model ridge still is within the range of elevations observed at natural submarine ridges.

Two experiments have been carried out, one with pure sand and the other using the 1:1 sand-mortar mixture, respectively (see section 4.1.2). The analogue material is sifted 3 cm thick onto the conveyor belt, which has the same high basal friction in each experiment. The model run begins with an accretive phase, during which the entire layer of material is accreted and forms a wedge against the backwall. This procedure avoids an arbitrarily chosen wedge geometry, which could potentially influence the course of the experiment. After ~120 cm of convergence, the sediment input ceases and the erosive phase begins in order to create a setting similar to South Peru (Figure 4.7). After the onset of the erosive phase, the model ridge is put onto the conveyor belt and approaches the wedge.

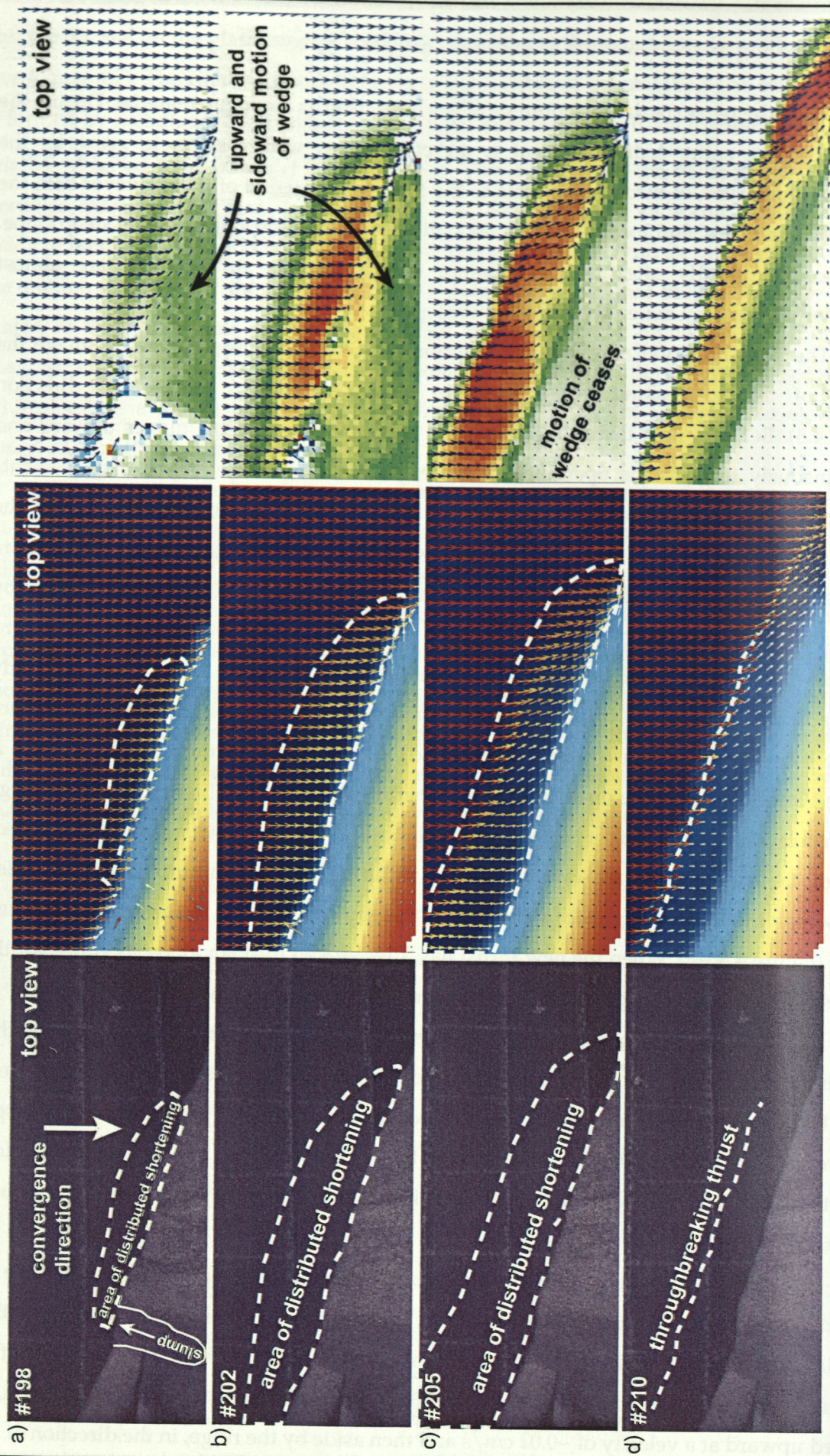
4.1.5 Simulating ridge subduction at an erosive margin

In the first of the two experiments, pure sand has been used as analogue material. During the first phase, the entire sediment input is accreted and a wedge starts to grow by the successive formation of thrust slices. Due to the high basal friction of the conveyor belt, the wedge soon reaches, and locally exceeds, its critical taper causing failure of the steep slope. Consequently, shortly after their formation, the developing thrust slices are almost completely covered by material moving downslope.

The high temporal and spatial resolution of the PIV pictures allows to image the growth of throughbreaking thrust faults in both, the vertical and lateral direction (Figure 4.8). Before a new thrust is created, the material of the wedge moves upward and simultaneously towards the open side of the experiment, with the largest displacements close to the toe of the wedge (Figure 4.8a, b, right column). The upward motion of the previously formed parts of the wedge slows down, once the thrust starts to develop (Figure 4.8c, right column). The initiation of the new thrust is clearly identifiable in the PIV results by distributed shortening in the approaching sand layer close to the wedge, with an upward movement of the sand by up to 0.1 cm/s (Figure 4.8b, right column). This motion is already observable for about 2 cm of convergence before the thrust breaks through the surface (Figure 4.8a-c) and becomes visible (Figure 4.8d). The material of the new thrust slice is dragged immediately to the open side of the experiment, while the other parts of the wedge remain relatively stable (Figure 4.8c-f, right column). While the new material is accreted, parts of the upper slope are over-steepened, resulting in local failure. The sand slides downward onto the newly growing thrust slice, thereby covering the formerly created thrust ridges (Figure 4.8d-g). When the new thrust has fully broken through along its entire width, upward motion of the wedge sets in again (Figure 4.8g, right column).

After 120 cm of convergence, the sediment input ceases and the erosive phase of the experiment begins, in which a setting similar to Peru is created. The wedge becomes over-critical throughout and adjusts to the ceased material influx by failure of the slope (Figure 4.9). The thrust slices formed during the accretive phase are completely hidden beneath the sliding sand. Now the model ridge is put onto the conveyor belt and approaches the wedge.

When the ridge collides with the wedge, its crest gradually indents the lower slope to a maximum of ~3 cm (Figure 4.10, left column). This re-entrant is maintained throughout the collision, although sliding sand sometimes fills it for short time intervals. The material of the wedge, which tends to move towards the open side of the experiment before the collision, is pushed upward at a velocity of ~0.02 cm/s and then aside by the ridge, in the direction of its



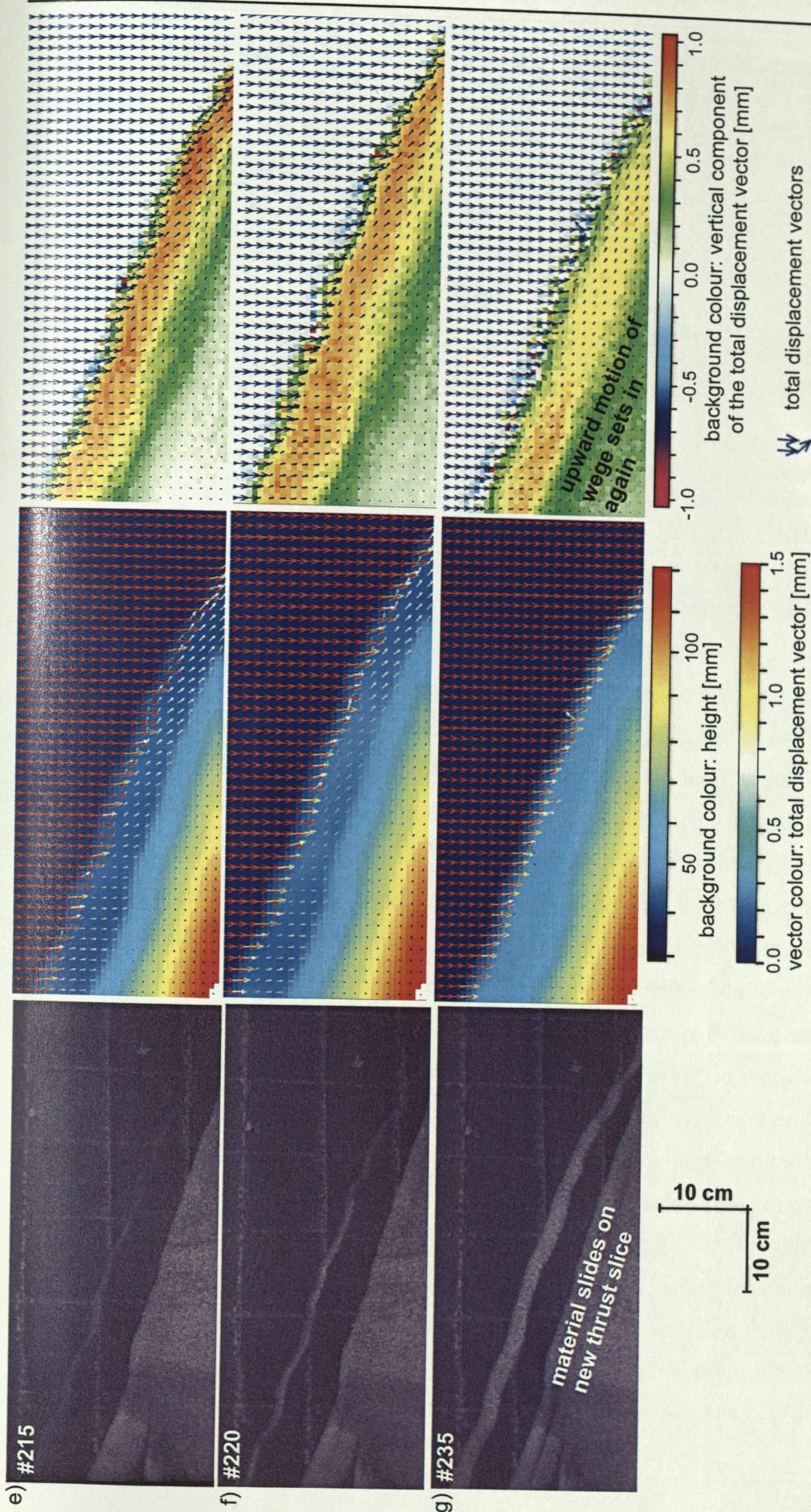


Figure 4.8: Image sequence of the experiment with pure sand showing the growth of a thrust (left column) and results derived from PIV analysis (middle and right columns) in top view. The arrows in all PIV images represent the total displacement vector field, which is calculated from two successive images. In the middle column, the displacement vectors are colour-coded, while in the right column the vectors are shown by blue arrows (length of vectors is 20 times the displacement; note that the map projection reduces the true length of the vectors proportional to their inclination). The total displacement vectors are overlain on colour-coded backgrounds showing the height of the experiment (middle column) and the vertical component of the displacement vector (right column), respectively. In the areas with no vectors, the particles moved faster than the PIV system could trace them. The total convergence between images #198 and #230 is ~4.5 cm.

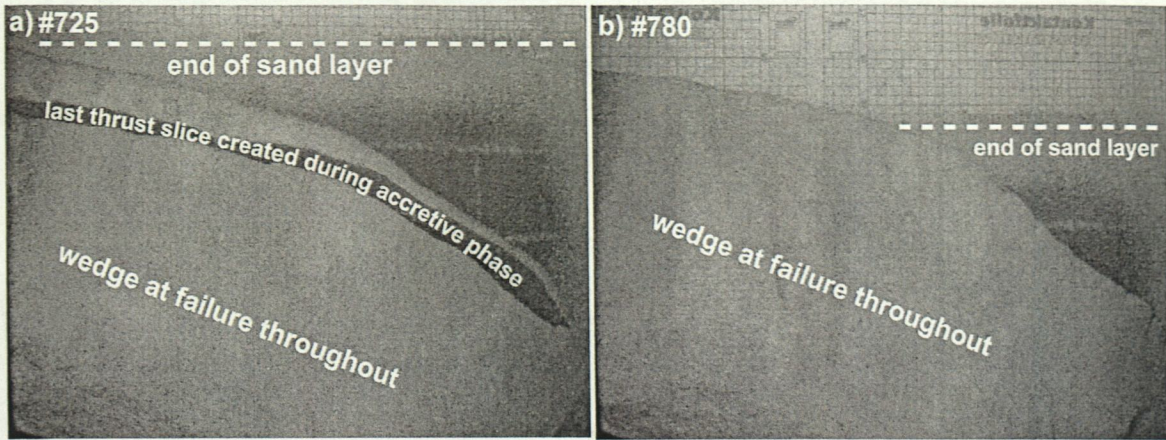
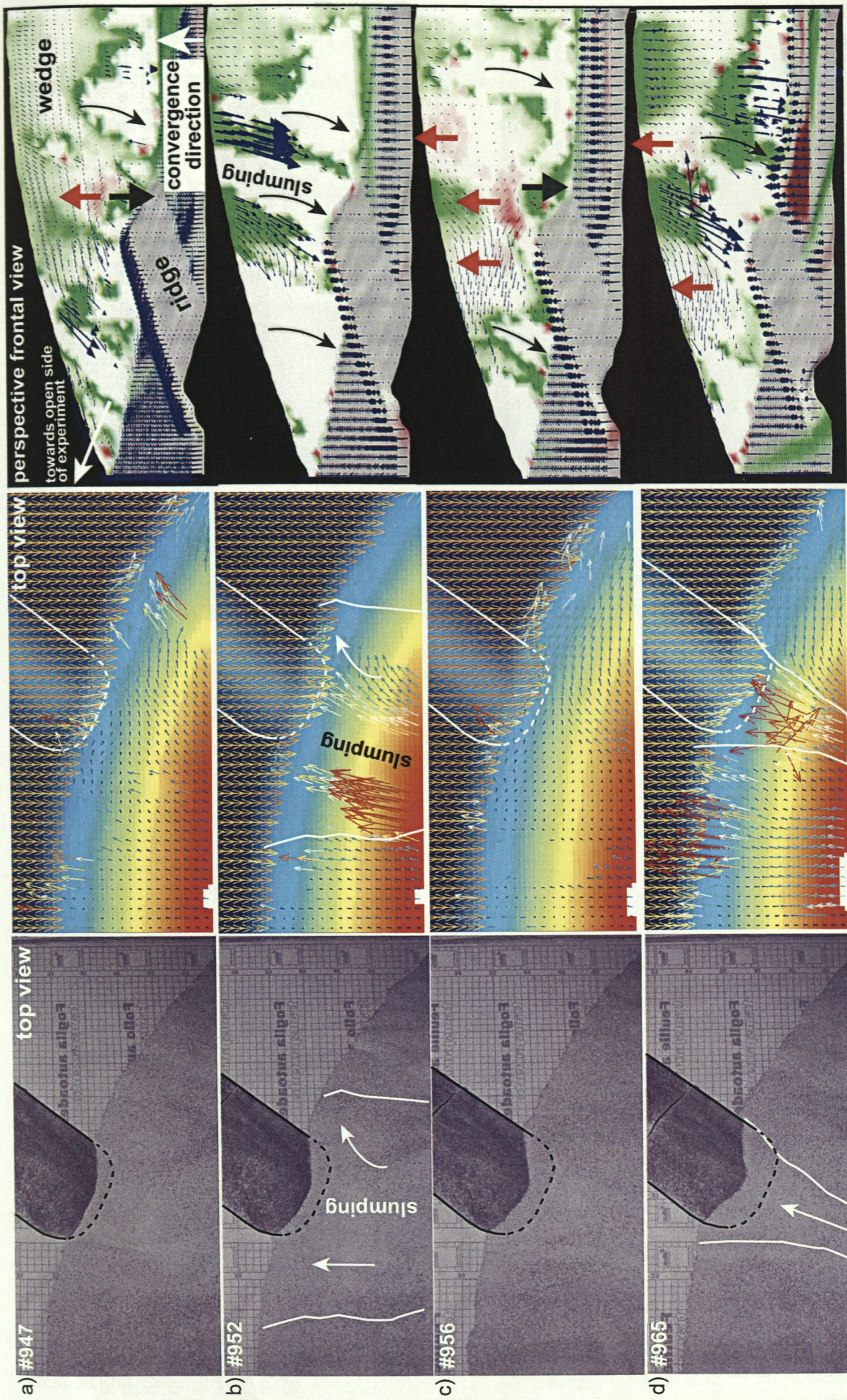


Figure 4.9: Images of the first experiment with pure dry sand (top view): a) End of the accretive phase. The wedge has reached and locally exceeds its critical taper. b) Onset of erosive phase. The slope of the wedge over-steepens and is at failure throughout leading to intense slumping.

migration (Figure 4.10, right column). Faulting in the wedge due to the underthrusting ridge is not observed. The ridge further steepens the slope of the wedge and triggers additional slumping, which is seen in the perspective view (Figures 4.10b). The sliding masses often diverge above the crest of the ridge (Figure 4.10b, d, f, right column).

During further subduction and lateral migration of the ridge, uplift of the wedge occurs at three different areas relative to the ridge. First, with the highest uplift rates of ~ 0.02 cm/s, above the ridge crest (Figure 4.10a, right column), second, in the prolongation of the ridge in the upper parts of the wedge (Figure 4.10c, d, e, right column) and third, above its leading flank (Figure 4.10c-f, right column). The maximum amount of uplift maintainable by the wedge above the ridge is small (~ 1 cm), because the uplifted material quickly adjusts by failure to the over-critical surface slope. The PIV image sequence shown in Figure 4.10 documents that the areas that experience uplift shift laterally in the movement direction of the ridge. In the wake of the ridge, the wedge subsides again (Figure 4.10a, c, e, right column), accompanied by frequently sliding of the sand. As a consequence, the effects of the ridge passage are not preserved in the morphology of the slope.

The monitoring of the slump events illustrates that the PIV system is capable to trace sand particles with velocities higher than of 0.15 cm/s. However, the frequent slumping interferes with the continuous monitoring of potential small-scale or long-lived effects caused by the subducting ridge. Nevertheless, a basic pattern in the mass transfer during ridge subduction with uplift along the ridge crest and above its leading flank and subsidence above its trailing edge can be extracted from the PIV results.



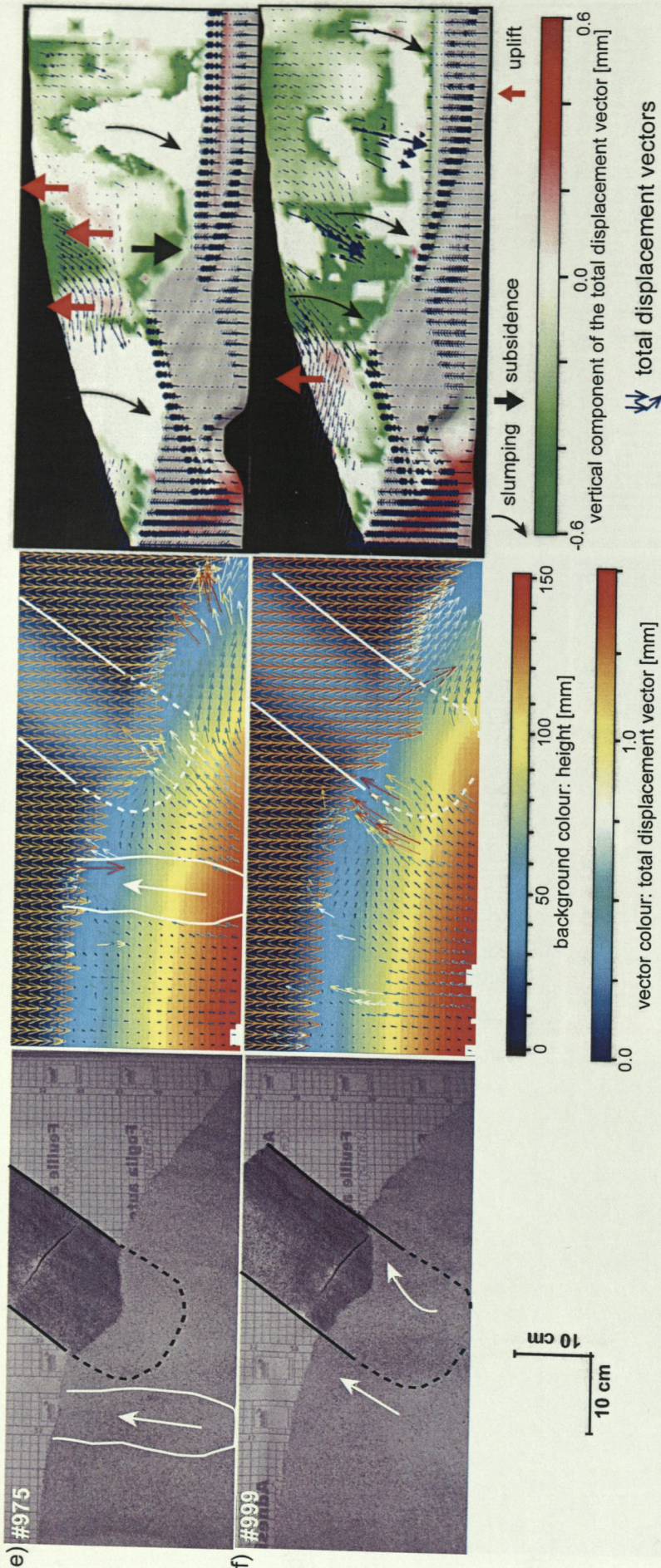


Figure 4.10: Image sequence of the first experiment with pure sand showing the collision and lateral migration of the model ridge (left column) and the displacement field derived from PIV analysis in top and perspective views (middle and right columns, respectively). The arrows in all PIV images represent the total displacement vectors. In the middle column, the displacement vectors are colour-coded, while in the right column the vectors are shown by blue arrows (length of vectors is 20 times the displacement; note that in the map view, the projection reduces the true length of the vectors proportional to their inclination). The total displacement vectors are overlain on the height of the experiment (middle column; background colour code) and the vertical component of the displacement vector (right column; colour-code on model topography). Thick red and green arrows mark areas uplifted or subsiding, respectively, during the passage of the ridge, while thin green arrows mark the parts of the slope that fail due to over-steepening (right column). The displacement vectors are calculated from two successive images. In the areas with no vectors, the particles moved faster than the PIV system could trace them. The total convergence between images #947 and #999 is ~16 cm.

In the second experiment, the 1:1 sand-mortar mixture is used as the analogue material to increase the slope stability by a higher internal friction of the wedge material. In addition, the smaller grain size of the material mixture was used to achieve a much higher spatial resolution. This strategy proved very successful, as structures of smaller scale were made visible and slumping was considerably reduced. Analogous to the first experiment, the model goes through an accretive phase during the first 120 cm of convergence, in which the successive formation of thrust slices leads to the formation of a wedge (Figure 4.11).



Figure 4.11: The formation of thrust slices during the accretive phase of the second experiment with the sand-mortar mixture (top view). Note that the structures are extremely well preserved due to the higher frictional strength of the material and the absence of slumping.

Towards the end of the accretive phase, the wedge approaches its critical taper, but does not become over-critical (Figure 4.12), as in the experiment with pure sand. During the transition from the accretive to the erosive regime, the lower part of the slope steepens and minor slumping occurs. In contrast to the first experiment, the morphology of the wedge, which developed during the accretive phase, is preserved.

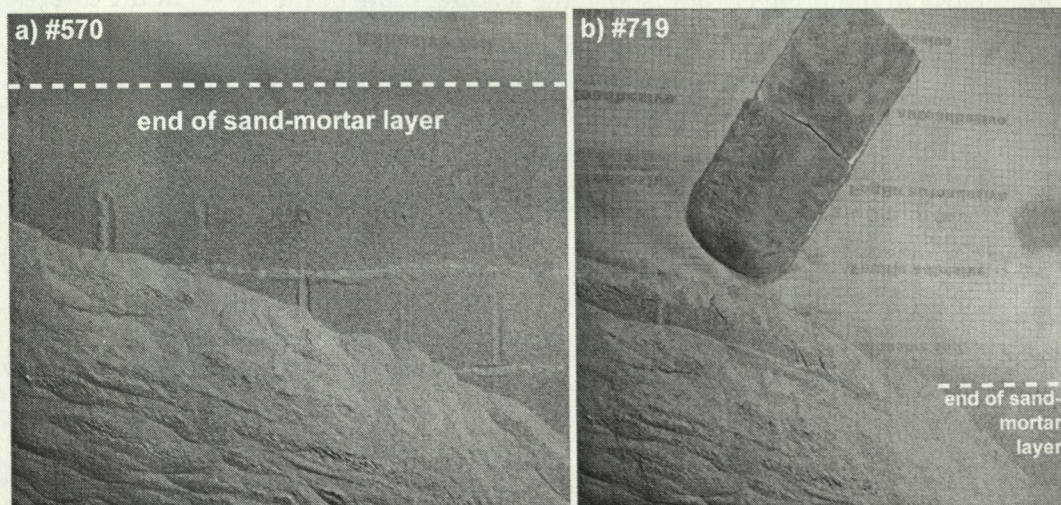
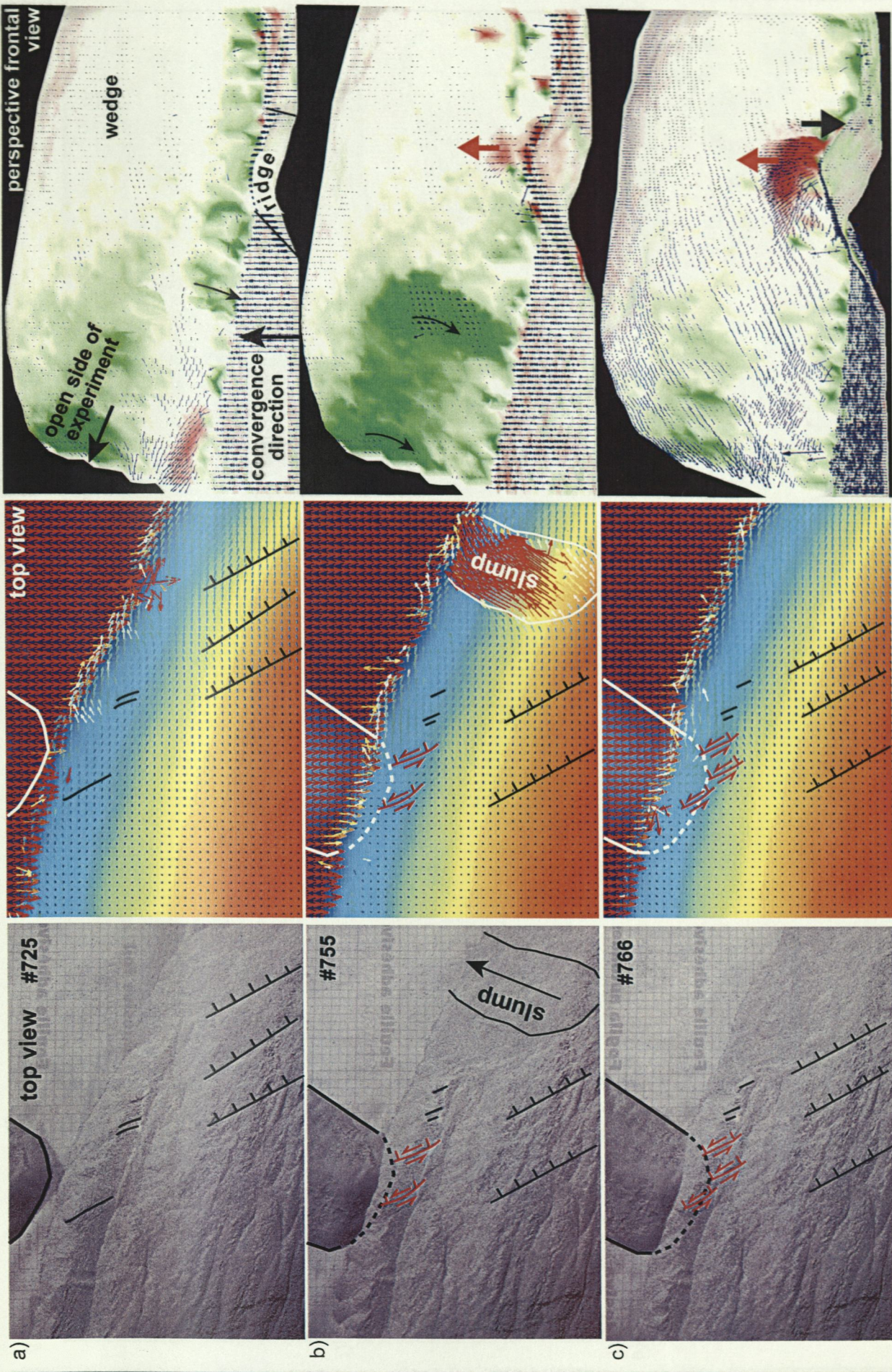


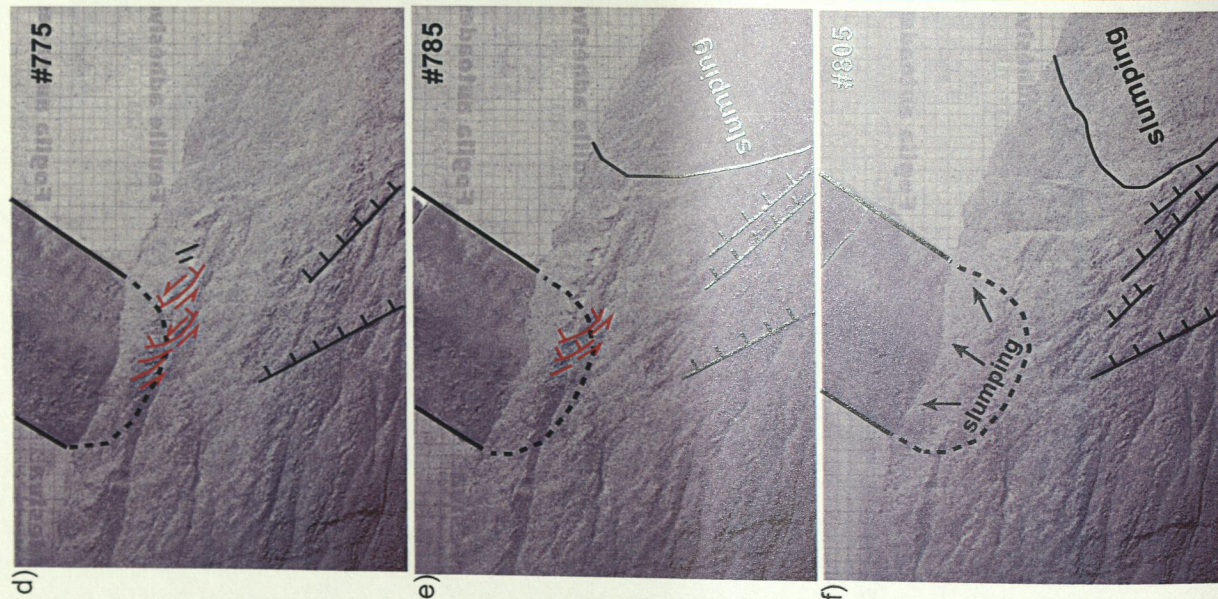
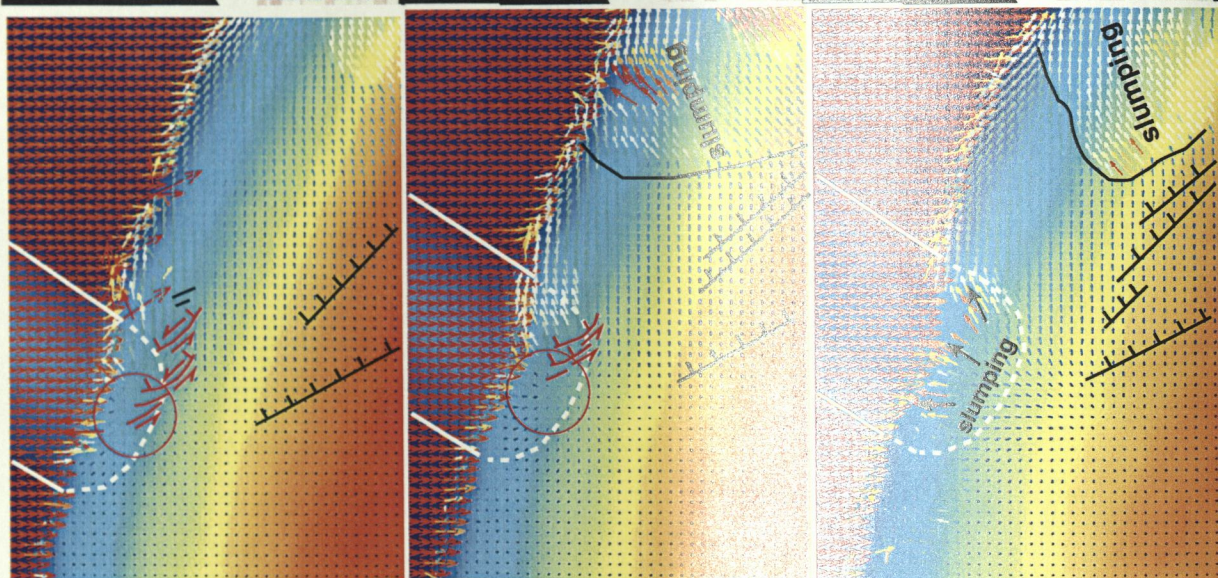
Figure 4.12: The second experiment with the sand-mortar mixture (top view): a) End of the accretive phase. In contrast to the experiment with pure sand, the wedge does not exceed its critical taper and thus, its slope remains stable. b) Erosive phase with approaching model ridge. As the material input ceases, the lower slope of the wedge becomes locally over-steep, resulting in small-scale slumping.

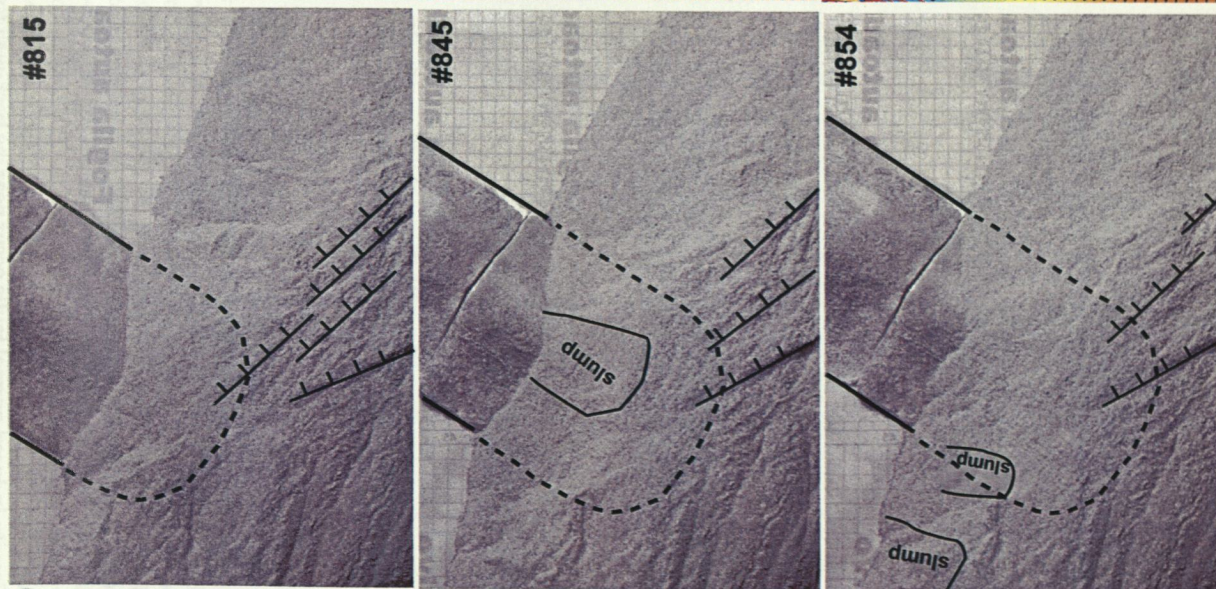
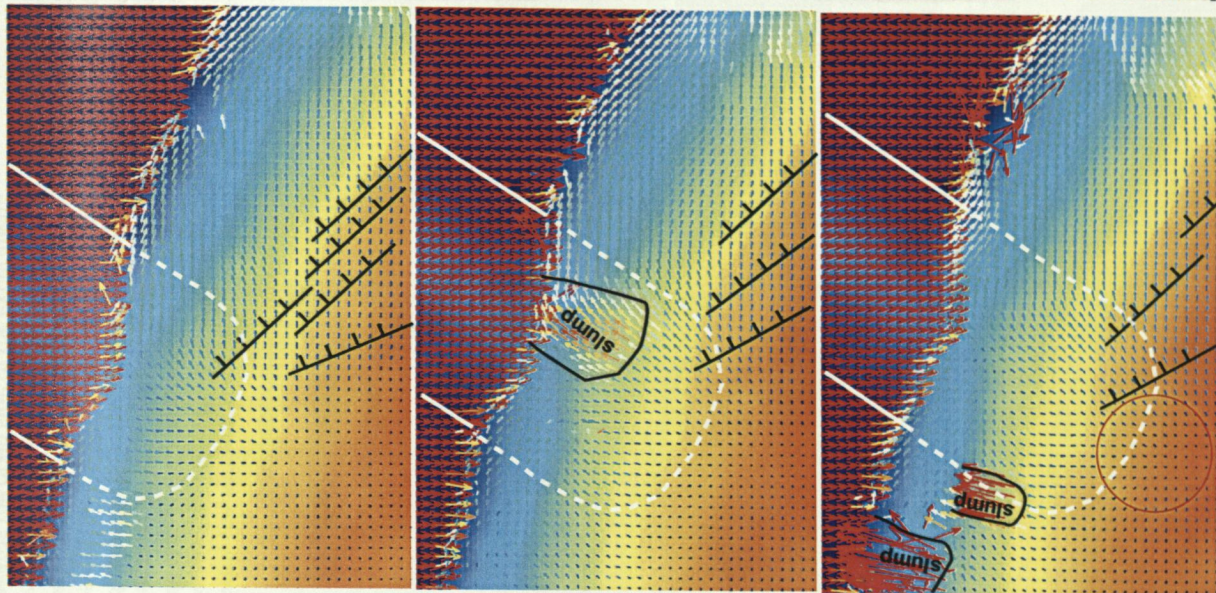
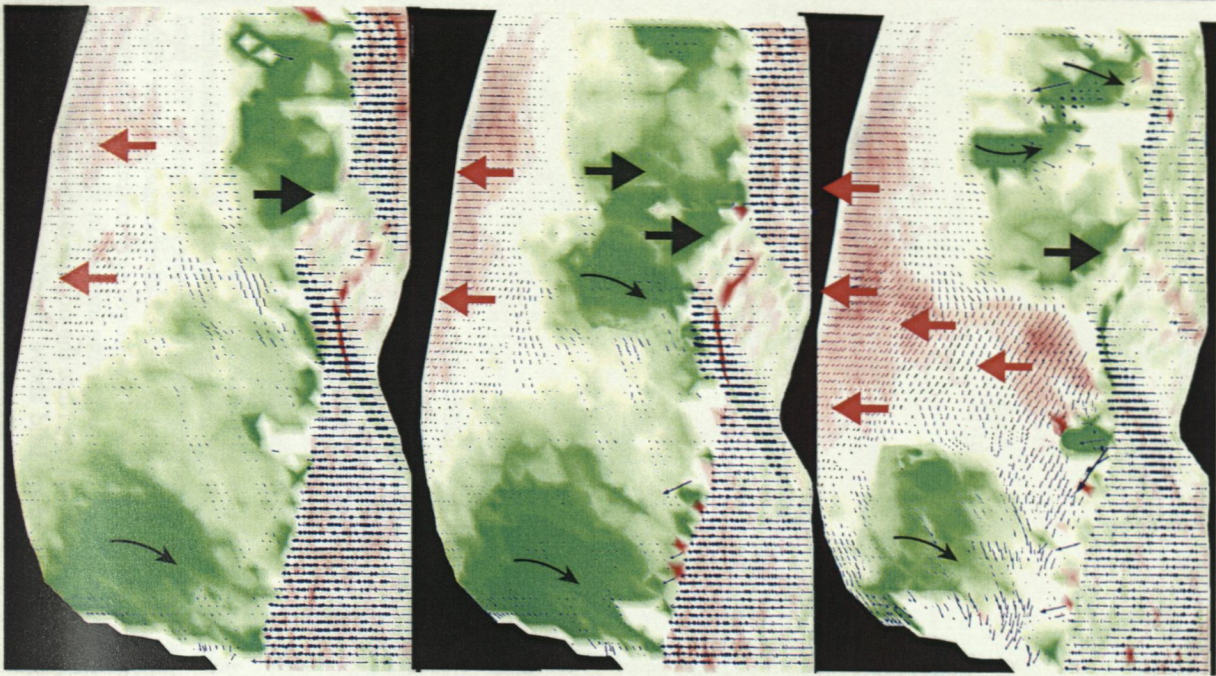
During the subduction of the model ridge, and in particular during the first ~10 cm of convergence, the wedge adjacent to the ridge remains largely stable and thus, allows to continuously monitor the displacement of the particles in great detail (Figures 4.13). At the beginning of the collision, the ridge underthrusts the wedge, however, in contrast to the first experiment, only slightly indents it (Figure 4.13a-f). The material of the lower slope is pushed aside by the leading flank of the ridge, in the direction of its lateral motion (Figure 4.13b-f, middle column). Simultaneously, the material above the ridge crest is uplifted at a rate of ~0.05 cm/s (Figure 4.13a, b, right column). The lowermost thrust slice of the wedge, which becomes narrower due to the frontal erosion induced by the cessation of the material input, is additionally shortened and pushed upward where the ridge subducts (cf. Figure 4.13b and g). Above the buried ridge, the thrust slice breaks open and oblique normal faults develop, accommodating the sideward pushing of the material by the ridge (Figure 4.13a-g, left column). These faults also show a normal component, indicating a tension. The developing fault network is asymmetric with respect to the colliding ridge. In the wake of the ridge, above its trailing flank, material starts to subside (Figure 4.13d-h, right column).

As the ridge is dragged deeper underneath the wedge, the amount of uplift increases to a maximum of ~2.5 cm (Figure 4.13f, middle column), while the uplift of the wedge gradually extends towards the backwall (Figure 4.13d-f, right column). The uplift of the wedge leads to over-steepening of its slope and thus, the first ridge-induced slump events occur at the lower slope, above the leading flank of the ridge (Figure 4.13d, right column). Above the ridge, a radial pattern of the displacement vectors is recognizable in some of the images (Figure 4.13d,e).

During ongoing lateral migration of the ridge, the location of the maximum uplift shifts from close to the ridge crest to above the leading flank of the ridge, in the direction of its motion (Figure 4.13d-k, right column). Therefore, slumping triggered by the ridge passage originates mainly above the buried leading edge of the ridge, gradually affecting higher parts of the slope (Figure 4.13g-k, right column). Furthermore, the ridge crest causes a gradually increasing indentation of the wedge, resulting in a less than 1 cm deep re-entrant towards the end of the experiment (Figure 4.13g-n, left column). (Figures 4.13g-h). Above the trailing flank of the ridge, the material of the lower and mid-slope subsides by ~2.5 cm at a rate of ~0.06 cm/s (Figure 4.13j-n, right column), however, slumping occurs less often (Figure 4.13k, l, right column).







g)

h)

i)

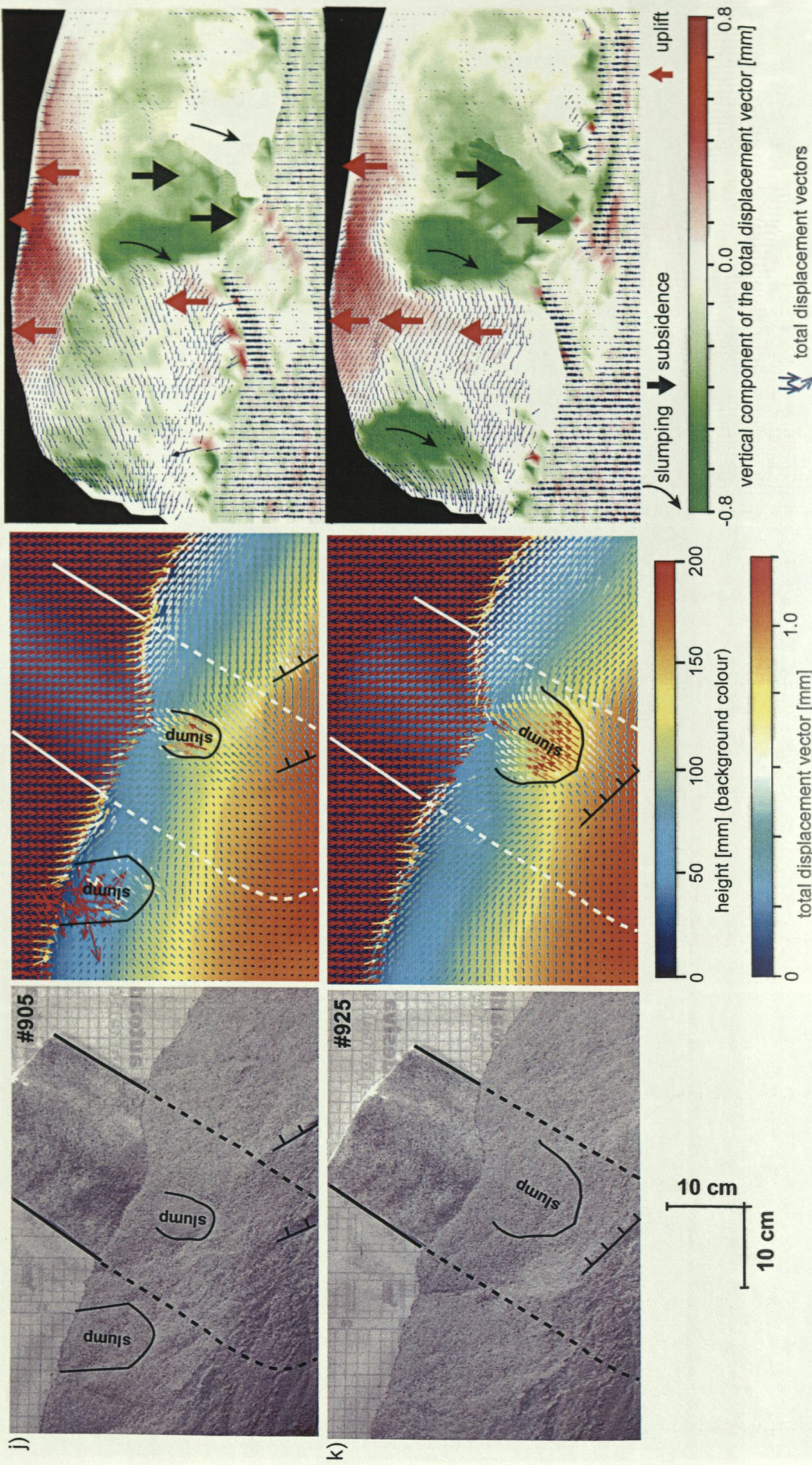


Figure 4.13: Image sequence of the second experiment with the sand-mortar mixture showing the collision and lateral migration of the model ridge (left column) and the displacement field derived from PIV analysis in top and perspective views (middle and right columns, respectively). The arrows in all PIV images represent the total displacement vectors (length of vectors is 15 times the displacement; note that in the map view, the projection reduces the true length of the vectors proportional to their inclination). The total displacement vectors are overlain on the height of the experiment (middle column; background colour code) and on the vertical component of the total displacement vector (right column; colour-code on model topography). Thick red and green arrows mark areas uplifted or subsiding, respectively, during the passage of the ridge (right column). Thin green arrows mark the parts of the slope that fail due to over-steepening (right column). The displacement vectors are calculated from two successive images. In the areas with no vectors, the particles moved faster than the PIV system could trace them. The total convergence between images #725 and #925 is ~40 cm. Note the normal faults with strike-slip component in the lowermost slope due to the collision with the ridge (b-e; marked in red), and a radial pattern in the displacement field above the ridge (d, e, i; red circles). Gravity-induced normal faults occur near the back-wall towards the open side of the experiment.

4.1.6 Discussion

The two 3D sandbox experiments designed to gain further insight into the subduction of the Nazca Ridge at the erosive Peruvian margin have successfully provided information about the temporal sequence of the effects induced by the passage of the ridge. While the first experiment with pure sand revealed the basic mass transfer modes, which were, however, frequently overprinted by slump events, the second model with a material of higher frictional strength achieved a much better preservation of structures and a higher spatial resolution due to a smaller grain size. The ratio of the internal to basal friction, however, was small enough in both experiments to maintain an erosive regime. For both experiments, the monitoring and analysis with the image correlation system PIV significantly improved the detection and identification of ridge-related effects compared to the observation by naked eye, photo or video camera. Especially for the experiment with the sand-mortar mixture, PIV yielded excellent high-resolution image sequences of the 3D displacement field of the deforming wedge surface and its temporal evolution during ridge subduction.

Table 4.2: Comparison of the phenomena observed in the 3D sandbox models and in the South Peruvian forearc.

sandbox experiment with sand-mortar*	South Peruvian forearc	
subduction of 3 cm (3 km) high model ridge	subduction of the 1.5 km high Nazca Ridge	(chapter 3)
~1 cm (1 km) deep re-entrant	minor re-entrant (< 2 km)	(chapter 3)
asymmetric distribution of uplift with maximum above leading ridge flank; maximum uplift: ~2.5 cm (2.5 km) uplift rate: 0.05 cm/s (1.8 km/Ma)	maximum uplift of marine terraces occurs south of the inland projection of the crest of the Nazca Ridge (cf. Figure 4.14); maximum uplift : 0.8-1 km uplift rate: 0.5-0.7 km/Ma	[Hsu, 1992; Macharé and Ortlieb, 1992]
oblique normal faults	faults and fractures (side-scan sonar data) normal faults at the coast, radial extension	[Hagen and Moberly, 1994] [Sébrier et al., 1985, 1988]
over-steepening of the slope, slumping; slumping more frequently above leading than trailing ridge flank	steepest lower slope (9-10°) observed off Peru; Quaternary slumping inferred from drilling; no data on frequency and distribution of slumping	[Bialas and Kukowski, 2000; Kulm et al., 1974]

*values in parentheses represent equivalent values in nature

The PIV analysis of both experiments shows that the subducting ridge causes uplift of the wedge above its crest and leading flank (Figure 4.14a; Table 4.2). At the onset of the collision, the material of the wedge is pushed upward and then towards the motion direction of the ridge. The maximum amount of the uplift occurs above the leading flank close to the ridge crest. The lower slope becomes over-steepened in this area and surface erosion sets in, with

material sliding downslope towards the leading edge of the ridge. In the wake of the ridge, the wedge subsides again, without major slumping, by an amount similar to the previous uplift. The second experiment with the mechanically stronger material revealed in its first stages that deformation in the material above the ridge crest leads to the development of normal faults that have a strike-slip component. At a later stage, the area of strongest uplift shifts in the motion direction of the ridge and thus, occurs above the leading flank of the ridge, while uplift continues to affect the wedge in continuation of the ridge. The material above the trailing edge moves downward, thereby maintaining a stable slope.

With respect to the indentation of the wedge by the ridge, the experiments reveal considerable differences. While the pure sand wedge is indented from the beginning of the collision resulting in a final ~3 cm deep re-entrant, the wedge of the sand-mortar mixture is only slightly indented at the onset of the collision and, later in the experiment, by less than 1 cm (cf. Figures 4.10 and 4.13). Since the latter material has a higher internal friction, this suggests that both, the depth and temporal evolution of a ridge-induced re-entrant depend on the mechanical strength of the wedge.

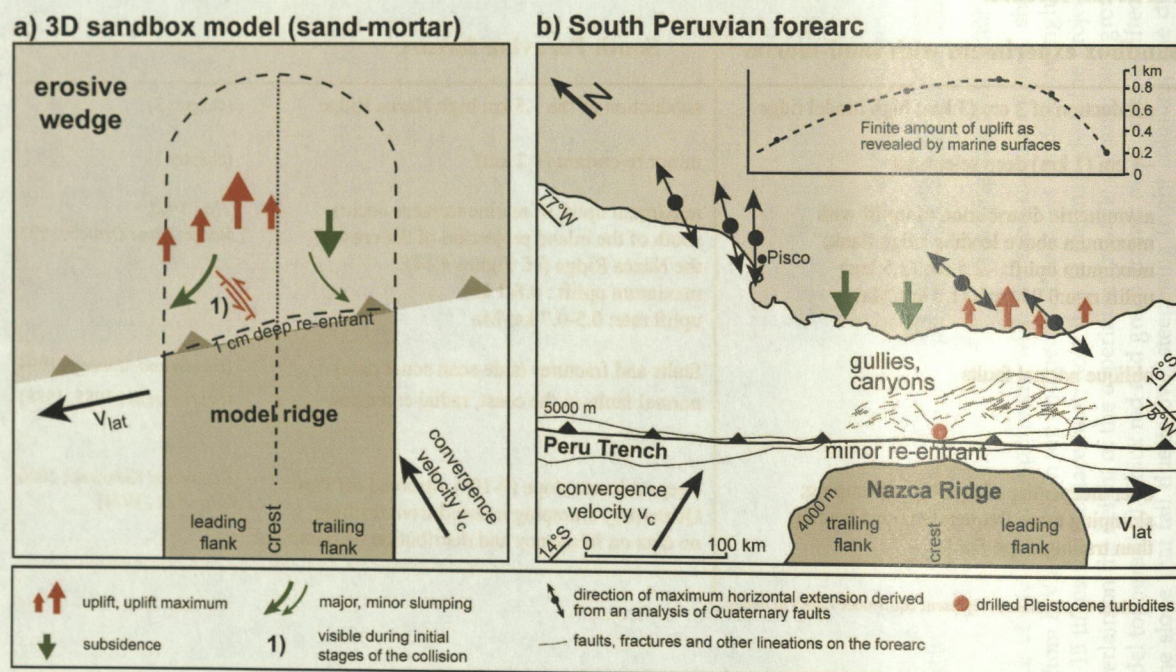


Figure 4.14: a) Schematic sketch illustrating the spatial-temporal sequence of effects caused by the model ridge in the 3D sandbox experiments (top view). b) Map of the collision zone of the Nazca Ridge and the South Peruvian forearc with elevation of coastal marine terraces (inset) (after Macharé and Ortlieb [1994]). Note that the model ridge moves to the left (a), while the Nazca Ridge moves to the right (b). The direction of horizontal extension onshore has been derived from Quaternary faults [Sébrier *et al.*, 1988]. Lineations in the submarine part of the forearc have been inferred from side-scan sonar data [Hagen and Moberly, 1994]. Drilled Pleistocene turbidites suggest slumping events during the passage of the ridge [Kulm *et al.*, 1974]. Surficial mass wasting is indicated by gullies and canyons observed in bathymetric and side-scan sonar data [Hagen and Moberly, 1994; chapter 3].

The temporal sequence of uplift and subsidence of the wedge during the subduction of the model ridge, with the maximum uplift being offset relative to the crest towards the motion direction of the ridge, is in excellent agreement with the observations at the collision zone (Figure 4.14b; Table 4.2). Where the Nazca Ridge subducts, a set of marine terraces reveals strong uplift above the southeastern flank of the ridge, while the coast above and north of the ridge crest experiences moderate uplift and net subsidence, respectively [Hsu, 1992; Macharé and Ortlieb, 1992]. As in the experiments, the maximum amount of uplift occurs south of the inland projection of the ridge crest, i.e. above its leading edge. The non-coincidence between the location of the uplift maximum and the highest point of the ridge has been attributed to the oblique subduction of the ridge [Hsu, 1992; Macharé and Ortlieb, 1992]. The analogue models support this explanation and additionally suggest that, at the onset of collision, the highest uplift occurs close to the ridge crest and later shifts away from the crest. This leads to an increasing asymmetry in the distribution of the uplifted areas with respect to the ridge axis (Figure 4.13). A close relationship between the spatial distribution of uplift and the obliquity of the ridge subduction is supported by a comparison between subducting ridges that have different orientations with respect to the convergence direction. Bathymetric data of the Louisville Ridge, which migrates southward along the erosive Tonga-Kermadec margin (Figure 4.15a), as well as the Gagua Ridge, which subducts obliquely at the accretive Ryukyu margin (Figure 4.16a), show that the highest forearc uplift occurs above the leading flank of both ridges [Ballance et al., 1989; Schnuerle et al., 1998; Dominguez et al., 1998].

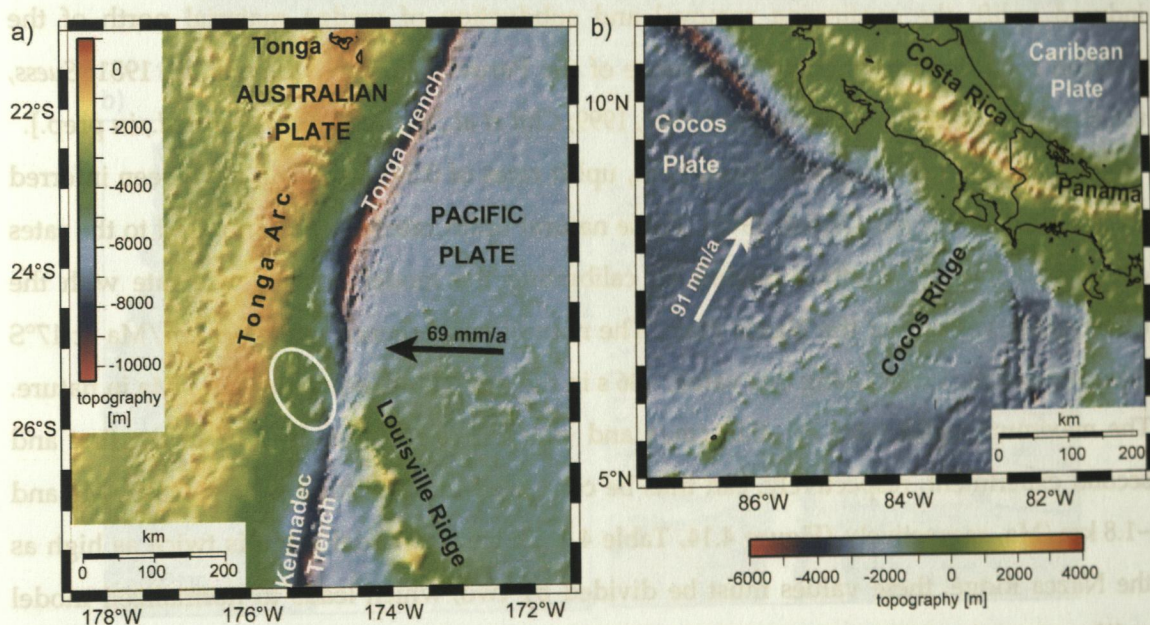


Figure 4.15: Topographic maps of a) the Louisville Ridge migrating southward along the Tonga-Kermadec margin and b) the Cocos Ridge subducting beneath Costa Rica-Panama [topography: Smith and Sandwell, 1997a; relative plate motions: DeMets et al., 1990]. White ellipse (a) shows that the maximum amount of uplift occurs above the leading edge of the Louisville Ridge.

In contrast, a comparison with the Cocos Ridge, which is parallel to the convergence direction of the Cocos Plate and does not migrate along the Panama-Costa-Rican margin (Figure 4.15b), shows that the uplift is related to the incoming relief of the ridge and almost symmetric with respect to its crest [Gardner *et al.*, 1992; Corrigan *et al.*, 1990].

The amount of uplift recorded in the analogue experiments will now be compared to the uplift observed in the natural system off Peru. Note that the height of the model ridge is 3 cm, which is equivalent to 3 km in nature, i.e. the model ridge is twice as high as the Nazca Ridge. The 1.5 km high Nazca Ridge has induced 800-900 m of uplift at the South Peruvian coast [Hsu, 1992; Macharé and Ortlieb, 1992], while the model ridge has caused ~1 cm and ~2.5 cm of uplift in the first and second experiment, respectively. The amount of uplift in the second experiment using the mechanically stronger material is considerably larger than in the first one and nearly equivalent to the height of the model ridge. Thus, the ratio of uplift to ridge height in the second experiment is similar to the ratio of natural uplift and height of the Nazca Ridge (Figure 4.14). The experiment using pure sand yielded a much lower ratio of uplift to ridge height, which suggests that the mechanically stronger sand-mortar mixture is more appropriate to model the rocks of the South Peruvian forearc. This is in agreement with results derived from geophysical data off Peru (chapter 3), which indicate that crystalline rocks with high seismic velocities and densities occur in the forearc. Above the trailing flank of the model ridge the amount of net subsidence is of the same order as the amount observed at the South Peruvian coastline [Hsu, 1992; Macharé and Ortlieb, 1992]. However, while the closed set-up of the experiment does not allow subsidence of the wedge to exceed the ridge-induced uplift, the continuing removal and subduction of wedge material north of the collision zone leads to ongoing subsidence of the Peruvian forearc [Kulm *et al.*, 1981; Suess, von Huene *et al.*, 1988; von Huene and Pecher, 1999; Clift *et al.*, in press; Kukowski *et al.*, in prep.].

For the marine terraces in South Peru, uplift rates of 0.5-0.7 km/Ma have been inferred [Hsu, 1992; Macharé and Ortlieb, 1992]. These natural uplift rates can be compared to the rates determined in both sandbox models by calibrating the model convergence rate with the convergence velocity of the Nazca Plate. The natural convergence rate is 68 km/Ma at 17°S [Norabuena *et al.*, 1998]. Using this value, ~36 s in the models are equivalent to 1 Ma in nature. The maximum uplift rates of ~0.02 cm/s and ~0.05 cm/s recorded by PIV in the first and second experiment, respectively, can thus be converted into uplift rates of ~0.7 km/Ma and ~1.8 km/Ma, respectively (Figure 4.14, Table 4.2). Since the model ridge is twice as high as the Nazca Ridge, these values must be divided by two, which leads to normalized model uplift rates of ~0.35 km/Ma and ~0.9 km/Ma. The higher uplift rate of the second experiment compares favourably with the natural uplift rate of ~0.7 km/Ma [Macharé and Ortlieb, 1992] (Figure 4.14).

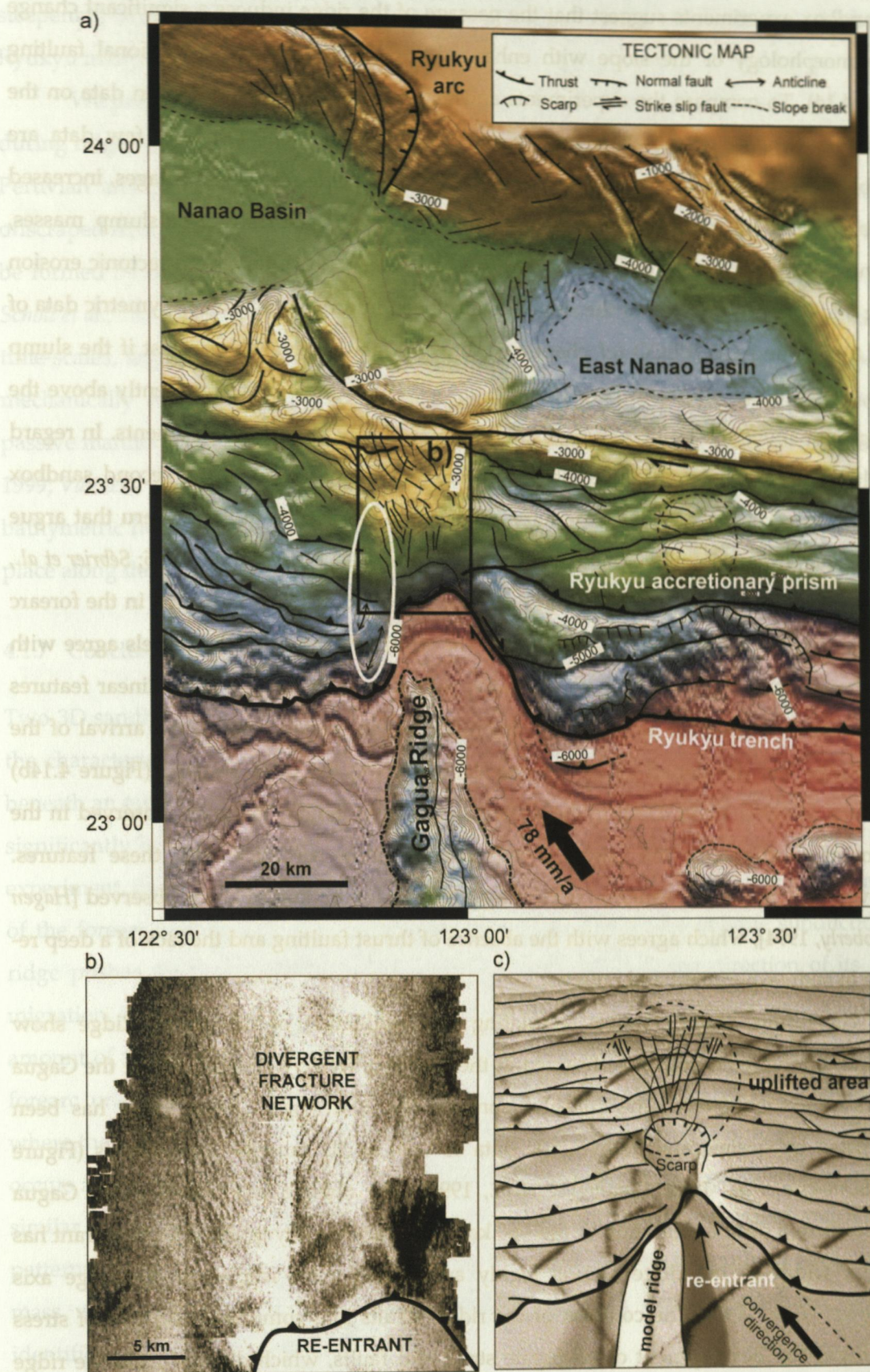


Figure 4.16: a) Bathymetric map with tectonic interpretation of the collision zone of the Ryukyu margin and the Gagua Ridge. White ellipse marks location of maximum uplift above leading flank. b) Detail map of the divergent fracture network in front of the re-entrant (see a) for location). c) 3D accretive sandbox model with subduction of a model ridge (redrawn from Domínguez et al. [1998]).

The sandbox experiments suggest that the passage of the ridge induces a significant change in the morphology of the slope with enhanced surface erosion and extensional faulting (Figure 4.14). To compare the experiments and nature in detail, high-resolution data on the surface morphology of the Peruvian forearc would be desirable, but only few data are available (Figure 4.14b; cf. chapter 3). From SEAMARC II side-scan sonar images, increased surface erosion due to the ridge has been inferred from the presence of slump masses, canyons and gullies [Hagen and Moberly, 1994; Li and Clark, 1994]. Enhanced tectonic erosion during and after the passage of the ridge has also been inferred from the bathymetric data of SEAMARC II and GEOPECO (cf. chapter 3), but no data are available to test if the slump events, which occur off South Peru [Kulm *et al.*, 1974], originate more frequently above the leading than above the trailing flank of the ridge, as observed in the experiments. In regard of faulting, the normal faults with strike-slip component observed in the second sandbox model are in accordance with Quaternary normal faults observed in South Peru that argue for horizontal extension above the Nazca Ridge (Figure 4.14) [Sébrier *et al.*, 1985; Sébrier *et al.*, 1988]. Furthermore, Sébrier *et al.* [1988] noted that radial extension is indicated in the forearc above the leading flank of the Nazca Ridge. The results of the sandbox models agree with these observations (Figure 4.13, b-e). Offshore, side-scan sonar images show linear features that have been interpreted as faults and fractures, which existed prior to the arrival of the Nazca Ridge and developed strike-slip extensions during the ridge passage (Figure 4.14b) [Hagen and Moberly, 1994]. Despite the differences in their length, the faults observed in the experiment shortly after the onset of the collision show affinities with these features. Moreover, only minor deformation indicating compression in South Peru is observed [Hagen and Moberly, 1994], which agrees with the absence of thrust faulting and the lack of a deep re-entrant in both, experiment and nature.

The results of the models simulating the subduction of the Nazca Ridge show profound differences to features observed at the accretive Ryukyu margin, where the Gagua Ridge subducts obliquely. The collision zone of the 2 km high Gagua Ridge has been investigated by seismic and bathymetric data as well as 3D sandbox experiments (Figure 4.16) [Schnuerle *et al.*, 1998; Dominguez *et al.*, 1998]. The oblique subduction of the Gagua Ridge leads to a deep indentation of the ~60 km wide accretionary prism. The re-entrant has a similar width as the ridge and is highly asymmetric with respect to the ridge axis [Dominguez *et al.*, 1998]. The collision of the ridge results in a compressional state of stress that induces the development of conjugate strike-slip faults, which diverge from the ridge crest to the NW and NE (Figure 4.16b). This divergent fault network, has been recognized in both, bathymetric data and sandbox models [Dominguez *et al.*, 1998], and differs significantly from the one inferred for the South Peruvian forearc (cf. Figures 4.14, 4.16). Despite

steepening of the slope due to the ridge, no large slump events have been identified at the Ryukyu margin [Schnuerle *et al.*, 1998].

We propose that these fundamental differences in the deformation of the upper plate during ridge collision arise from the different mass transfer regimes that have acted upon the Peruvian and Ryukyu margins. At accretive margins, mechanically weak sediments are offscraped from the oceanic plate and accreted against a less deformable buttress, which may be formed by older accreted material, arc-derived intrusives, or older basement rocks [e.g. Scholl *et al.*, 1980; von Huene and Scholl, 1991]. In contrast, tectonic erosion removes, over long time-scales, any weak sediments that might have been accreted earlier. As a consequence, mechanically strong crystalline rocks are gradually transferred toward the trench in a passive manner [von Huene and Lallemand, 1990; von Huene and Scholl, 1991; Clift and MacLeod, 1999; Vanneste and Larter, 2002]. Thus, the strength of a forearc and its response to a colliding bathymetric high will depend on whether long-term accretion or tectonic erosion has taken place along the margin in the past.

4.1.7 Conclusions of the analogue modelling

Two 3D sandbox models with analogue materials of different frictional properties revealed the characteristic morphology and mass transfer modes during the subduction of a ridge beneath an erosive margin. The experiment using the material of higher strength achieved a significantly better agreement with the observations at the South Peruvian margin. In this experiment, the ridge does not significantly deflect the lower part of the wedge and the uplift of the forearc is equivalent to the height of the ridge. Due to the oblique subduction, the ridge pushes the wedge material upwards and to the side in the direction of its lateral migration. Oblique normal faults develop in the wedge. Later in the experiment, the highest amount of uplift shifts towards the leading flank of the ridge. In the wake of the ridge, the forearc undergoes net subsidence. Slumping mainly originates above the leading flank, where the amount of uplift and thus the slope angles are largest, while only minor slumping occurs above the trailing flank. The temporal sequence of uplift and subsidence by amounts similar to the vertical relief of the model ridge, agree well with the spatial and temporal patterns of uplift and subsidence, inferred for the collision zone in southern Peru. Surficial mass wasting and horizontal extension observed in both experiments have also been identified in South Peru.

The sandbox models and their comparison with other margins indicates that, in contrast to accretive margins, erosive margins undergoing ridge subduction are generally characterized by a minor re-entrant, an observation that may be explained by a mechanically

strong frontal wedge. The presence of mechanically strong rocks in the frontal wedge can be explained by long-term tectonic erosion, a process that causes continental basement to shift passively towards the trench. At erosive margins, the main response to ridge subduction is inferred to be forearc uplift accompanied by frequent slumping and horizontal extension, while at accretive margins, deformation caused by horizontal shortening prevails. Independent of the mass transfer regime, however, the natural examples as well as the 3D sandbox models show that the highest uplift rates occur above the leading flank of the ridge in case of oblique subduction, and thus, do not need to coincide with the ridge crest.

4.2 Numerical modelling

4.2.1 Principles of numerical modelling and application to subduction zones

Physical systems are governed by (1) laws of conservation, which apply to matter, kinetic, thermal, and potential energy, (2) equations of continuity concerning system-specific variables, and (3) constitutive relationships between these variables. A mathematical formulation of a physical system must accomplish these requirements. Thereby, the systems may be classified as equilibrium problems of steady-state systems and diffusion or inertial problems of transient systems, governed by velocity or acceleration laws, respectively [Mohr, 1992]. Typically, the mathematical formulation consists of a set of linear or non-linear ordinary and partial differential equations. The solution for these equations is sought within initial and boundary conditions that have to be specified. For simple problems, solution of the constitutive equations may be found analytically, to solve more complex problems, however, numerical approximation techniques need to be applied [e.g. Zienkiewicz and Taylor, 1987; Fagan, 1992; Mohr, 1992; Carr, 1995].

The inherent complexity of geologic systems generally requires to solve their governing equations by numerical modelling techniques, among which the Finite-Difference and the Finite-Element methods are the most widespread [e.g. Toksoez *et al.*, 1971; Richardson, 1978; Zoback and Zoback, 1980; Fleitout and Froidevaux, 1983; Thomas, 1984]. Numerical models can help to identify the main driving forces and parameters influencing a specific geologic system. Such models are particularly useful if the geologic processes are not directly observable, either due to the long time-scale of their evolution or their location at an inaccessible depth.

Against this background, the different processes occurring in subduction zones have been the subject of numerous numerical modelling studies, which aimed at a better understanding of the mechanical or thermal states of the downgoing and the upper plate and their evolution during the subduction process [e.g. *van den Beukel and Wortel, 1987; Richards and Davies, 1989; Peacock, 1990; Yoshioka and Wortel, 1995; Cattin et al., 1997; Hassani et al., 1997; Houseman and Gubbins, 1997; Conrad and Hager, 1999; Davies, 1999; Ranalli et al., 2000; Winder and Peacock, 2001*]. Particular aspects of the frontal parts of subduction zones studied by numerical models include the flexure of the downgoing plate [e.g. *Turcotte et al., 1978; Royden, 1993; Zhong and Gurnis, 1994; Buiter et al., 2001*] and the mechanics of the frontal wedge [e.g. *Liu and Ranalli, 1992; Maekel and Walters, 1993; Hardy et al., 1998; Huhn, 2002*]. In regard of the latter, models have been designed to decipher the particle paths in frontal wedges resulting from different mass transfer modes, i.e. from complete sediment subduction to complete accretion [*Beaumont et al., 1999; Ellis et al., 1999*]. Furthermore, numerical models helped to better understand the transport of fluids and heat within accretionary prisms [e.g. *Screaton et al., 1990; Wang, 1994; Kukowski and Pecher, 1999*].

4.2.2 Principles of the Finite-Element method and realization in ABAQUS

The Finite-Element method belongs to the continuum methods, in which the body under consideration is divided into discrete parts, i.e. the finite elements [*Zienkiewicz and Taylor, 1987; Fagan, 1992*]. Neighbouring elements are connected by common knots, and all elements and nodes together form the mesh that approximates the body to be studied. The Finite-Element analysis starts with determining the governing equations of each element. These equations can always be transferred into the general formulation

$$\{u\} = [N] \{u_n\}$$

where $\{u\}$ is the vector of applied nodal forces, $\{u_n\}$ the vector of the sought displacements at the n nodes of the element and $[N]$ the so-called element stiffness matrix, which always has a square form. The element equations can either be assembled in a Lagrangian or Eulerian formulation. In the Lagrangian formulation, the mesh is bound to the material and therefore follows its changes in shape during deformation. The Lagrangian description may also be used in analyses that consider the field of a physical quantity, for instance of temperature. In the Eulerian formulation, the mesh remains undeformed and the material or the field of a physical quantity shifts through the mesh.

The equation sets of all elements are added and yield the system equation set for the whole body, which can be written as

$$u(x) = \sum_{k=1}^n N_k(x) u_k$$

where N_k is the global stiffness matrix. After inserting the initial and boundary conditions, the equation system describing the whole body is solved by inversion of the global stiffness matrix. Since this matrix can become very large, its inversion often is not trivial. Thus, many sophisticated inversion techniques have been developed, taking advantage of the symmetry of the matrix and the presence of entries with value zero [Zienkiewicz and Taylor, 1987; Fagan, 1992]. The solution to the inversion problem is generally found iteratively, by using a type of extremum method, which is applicable for most continuum problems. For example, displacements of the nodes are determined by minimizing the total potential energy. An iteration may consist of an implicit or explicit search for the solution: Implicit techniques calculate the global solution for the unknown variables by sub-iterations of arbitrary length, while explicit methods solve the equation element-wise in many short sub-iterations. The total number of iterations increases significantly, if non-linearities are involved, which can arise from the boundary conditions, a specific geometry or due to the rheology of the materials. The final solution exists both at the nodes and within the finite elements. To transfer the results to nature, no scaling factor is needed, since the dimensions of the model and the magnitude of the parameters can be chosen according to the modelled system.

The Finite-Element technique is realized in the commercial software package ABAQUS [Hibbitt *et al.*, 2002], which offers several, optionally available modules: ABAQUS/Standard applies an implicit solution technique and the Lagrangian formulation, while ABAQUS/Explicit uses the explicit solution method and enables the Eulerian formulation. Apart from that, additional modules are available for specific physical problems (e.g. ABAQUS/AQUA). To construct and mesh the models, the software package includes the graphical user interface ABAQUS/CAE.

ABAQUS was originally designed as engineering Finite-Element software, but has, over the last years, increasingly been used to model geodynamic problems. ABAQUS has been used to simulate post-glacial isostatic adjustments of the Earth [Wu, 1999; Wu, 2001], crustal thickening during continental collision [Gerbault *et al.*, 2002], mountain building, and histories of sedimentary basins [Gabriel *et al.*, 1997; Hansen *et al.*, 2000; Fischer, 2001]. With respect to subduction zones, ABAQUS has been applied to investigate the evolution of subducting slabs [Ranalli *et al.*, 2000], the coupling along the interface between the upper and downgoing plate [Dmowska *et al.*, 1996], and the initiation of subduction due to failure of passive margins [Branlund *et al.*, 2000; Regenauer-Lieb and Yuen, 2000; Branlund *et al.*, 2001; Regenauer-Lieb *et al.*, 2001].

To perform the models of this study, the module ABAQUS/Standard has been available. ABAQUS/Standard offers various types of elements in different formulations, of which continuum elements are the most important for the modelling aims of this study. The elements may be linear or quadratic: Linear elements have nodes at the corners of the element, whereas quadratic elements have additional nodes along the edges between the corners and possess more integration points within the element than linear ones. If contact interfaces are present between model parts, the use of linear elements is recommended [Hibbitt *et al.*, 2002]. However, linear elements tend to show shear-locking, i.e. their edges are, in contrast to natural materials, incapable to bend, which leads to unrealistic shear stresses. In order to overcome this problem, ABAQUS offers a so-called incompatible mode formulation [Hibbitt *et al.*, 2002]. A hybrid formulation of the elements is used if a linear increase of pressure within almost incompressible elements is needed. The 2D models use plain strain elements, i.e. no strain across the model plane. Nevertheless, the out-of plane stress does not need to be zero. The 3D model involved linear, brick-shaped hexahedral stress elements.

In ABAQUS/Standard, as in most Finite-Element codes, the units of physical quantities are not pre-defined. As a first step, a consistent unit system for mass, time and length using kilogram, second and kilometer, respectively, has been defined. The use of the non-SI unit kilometer was necessary, because ABAQUS/Standard limits the model size to 200 000 length units, whereas the models of this study required lengths of up to 1000 km. The units of all other physical quantities have been transverted accordingly. Note that, unlike the geological convention, ABAQUS assigns a negative sign to compressional stresses, while tension has positive values. To facilitate the comparison with stress fields derived from geological studies, the signs of the stresses values yielded by ABAQUS have been inverted in the figures of the following sections.

4.2.3 Isostatic uplift of the Peruvian forearc caused by the Nazca Ridge

The goal of this 2D model is to assess the amount of isostatic uplift that is to be expected in the Peruvian forearc from the subduction of the thick, buoyant crust of the Nazca Ridge. In general, the amount of isostatic uplift induced by replacing oceanic crust of normal thickness by the thicker crust of an aseismic ridge can be estimated by applying Archimedes' principle for a 1-dimensional column model (Figure 4.17) [Corrigan *et al.*, 1990; Turcotte and Schubert, 2002]. The variation in crustal thickness and density is assumed to be compensated at some arbitrary depth. Prior to ridge subduction, a column consists of the water above, the continental crust of the forearc, the subducting oceanic crust and the mantle. During ridge

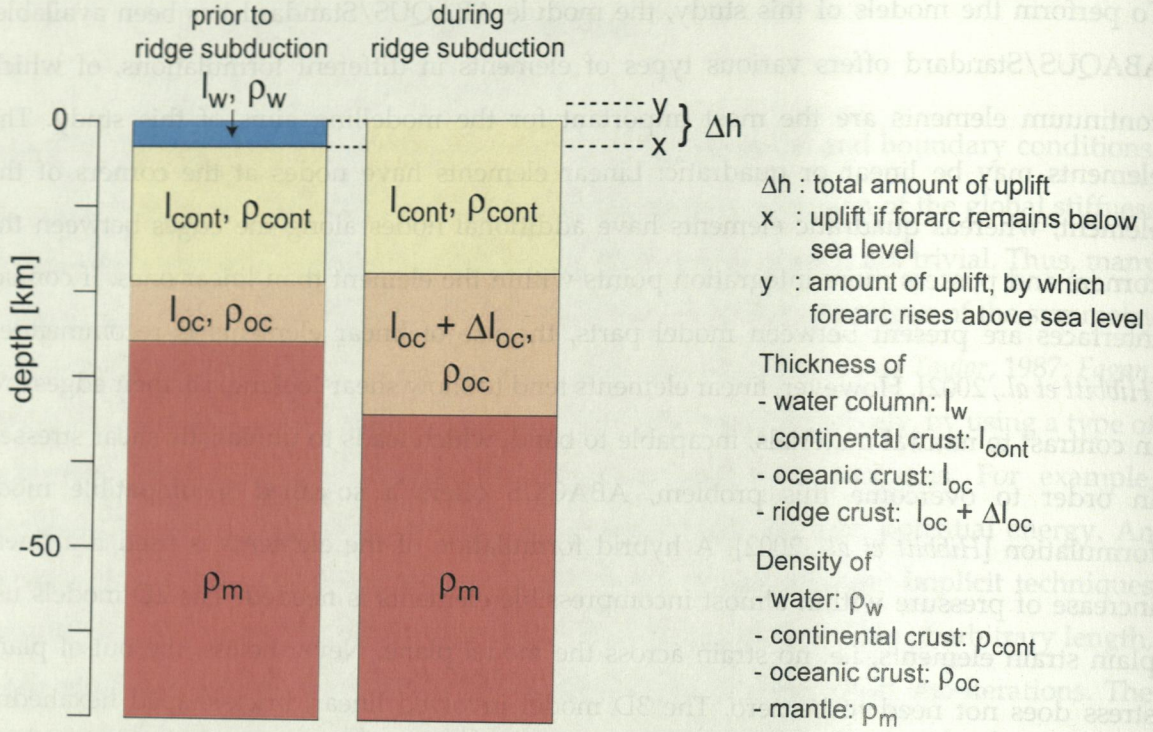


Figure 4.17: Lithospheric columns illustrating the isostatic uplift induced by replacing oceanic crust of normal thickness by a thicker ridge crust (modified after Corrigan *et al.* [1990]).

subduction, the oceanic crust of normal thickness l_{oc} is replaced by the thicker ridge crust $l_{oc} + \Delta l_{oc}$ (Figure 4.17). The resulting buoyancy forces raise the lithospheric column by an amount Δh . Depending on whether the top of the crustal column remains below sea level or rises above sea level, two cases may occur (Figure 4.17):

$$\Delta h = \{x : x < l_w\} \quad x = \frac{\Delta l_{oc} (\rho_m - \rho_{oc})}{\rho_m - \rho_w}$$

$$\{l_w + y : x > l_w\} \quad y = \frac{\Delta l_{oc} (\rho_m - \rho_{oc}) - l_w (\rho_m - \rho_w)}{\rho_m}$$

In the first case, in which the total amount of uplift does not exceed the water depth l_w ($\Delta h = x$; $x < l_w$), the amount of uplift Δh equals x and is constant along the entire submarine forearc. This implies that the coastline above the ridge axis represents the location, where the paleo-water depth before ridge subduction was equal to the amount of uplift induced by the ridge, assuming that the forearc is isostatically compensated. In the second case, the buoyancy forces raise the forearc above sea level ($\Delta h = l_w + y$; $x > l_w$) and the amount of uplift decreases with decreasing paleo-water depth before ridge subduction. If the forearc is subaerial at the onset of uplift ($l_w = 0$), the amount of uplift equals y and remains unchanged for the entire subaerial forearc, analogous to the setting in which the forearc remains

completely submarine. Note that the amount of uplift does not depend on the thickness of the continental crust.

The amount of forearc uplift induced by the Nazca Ridge can be calculated by inserting the crustal thicknesses of the ridge and the adjacent oceanic crust into the above relationship. As derived from seismic velocity models, the Nazca Ridge is ~17 km thick (chapter 3; Figure 3.14), while the normal oceanic crust off Central Peru is ~7 km thick [Bialas and Kukowski, 2000; Krabbenhoef *et al.*, in prep.], i.e. the difference in thickness Δl_{oc} is 10 km. Densities of 2900 kg/m³ and 3300 kg/m³ are assigned to oceanic/ridge crust and upper mantle, respectively [Corrigan *et al.*, 1990]. Using this values, the amount of isostatic uplift of the South Peruvian forearc is 1.7 km, if it remains submarine. Consequently, in places where the paleo-water depth has been less than 1.7 km, the forearc rises above sea level. A completely subaerial forearc is raised by 1.2 km.

Analogous to the above-mentioned crustal columns, 2D-Finite-Element models have been used to simulate the isostatic uplift of the Nazca Ridge at different distances from the trench. The concept involves an initial model of three layers representing continental crust, oceanic crust and mantle, respectively. Under influence of gravity, the column is in isostatic equilibrium. Replacing the upper part of the mantle by ridge crust induces buoyancy forces and uplift.

In the first step, a procedure to achieve the isostatic equilibrium of such a lithospheric column by applying gravity and respective counteracting forces is tested with a 200 km long model, representing 70 km thick oceanic lithosphere (Figure 4.18). The oceanic crust and the lithospheric mantle have densities of 2900 kg/m³ and 3300 kg/m³, respectively. For the implementation in ABAQUS, a strategy introduced by Fischer [2001] has been adopted. The force acting against gravity is the buoyancy force resulting from the density contrast between lithosphere and asthenosphere. The buoyancy force F_b is created by an elastic, so-called Winkler foundation at the bottom of the model and is computed by

$$F_b = -k \Delta z,$$

where Δz is the vertical displacement at the bottom of the model. The value of k the proportionality factor is calculated by

$$k = \rho_{asth} g A,$$

where ρ_{asth} is the density of the asthenosphere, g is the gravitational acceleration and A is the area of the element. The density of the asthenosphere is 3500 kg/m³ [Kennett, 1991].

To avoid a compression of the model due to its own weight, the lithostatic stresses σ_{yy} of the model layers are calculated by

$$\sigma_{zz} = \rho g z,$$

where ρ is the density of the layer and z the depth, and inserted as initial condition into the model file. At the bottom of the model, a lithostatic pressure corresponding to the respective depth is applied (Figure 4.18) [Fischer, 2001]. From these initial and boundary conditions, the

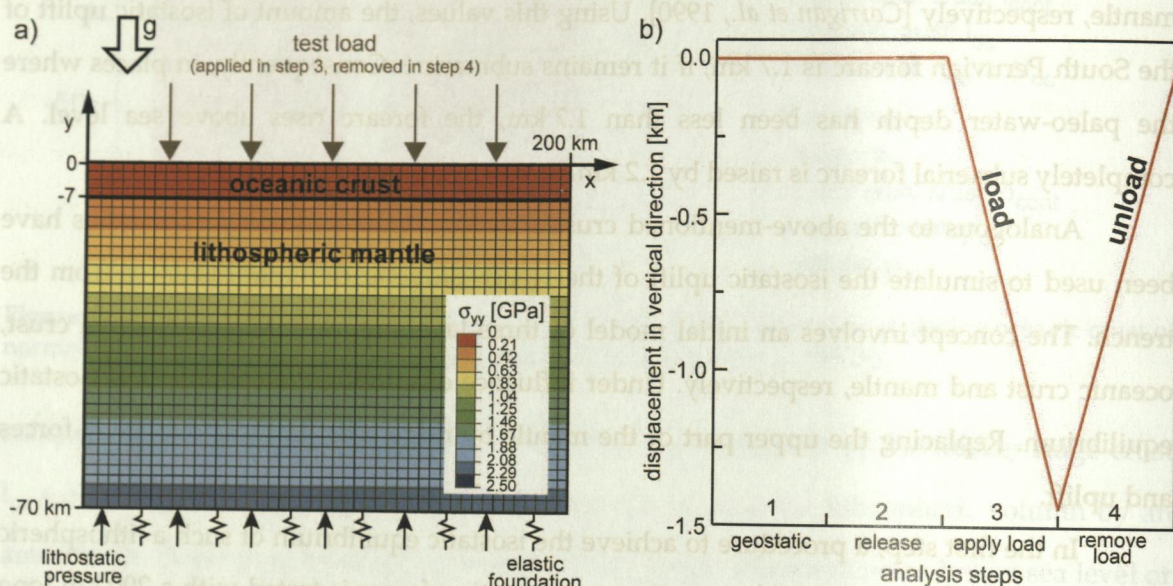


Figure 4.18: Test of the isostatic compensation, implemented as described by Fischer [2001], in a model representing oceanic lithosphere. a) Lithostatic stress field of the oceanic lithosphere under gravity. The gravity force is counteracted by a lithostatic pressure and elastic foundation at the base of the model (see text for details). b) Step 1: The lithostatic stress field of the fixed model is computed on the base of a manually calculated initial stress field. Step 2: After releasing the model, negligible vertical motion (not seen in plot) occurs indicating that the initial stress field was accurate. Step 3: On top of the model that is in isostatic equilibrium a test load is applied leading to subsidence until the new equilibrium position is reached. Step 4: After removing the test load, the model returns to its initial position.

stress field is calculated in a geostatic analysis, using the manually calculated lithostatic stresses as starting values [Fischer, 2001]. During this step, all elements are kept fixed in all directions and released afterwards, except for the sides that cannot move in horizontal direction. After the release, the model may, depending on the accuracy of the manually inserted stress field, adjust by small vertical motion until compensation by the buoyancy forces is achieved. The model then is balanced in isostatic equilibrium. The application of a load on top or the removal of elements from the surface would now lead to uplift or subsidence of the model [Fischer, 2001].

The results for the oceanic lithosphere model (Figure 4.18) show that after calculating the lithostatic stress field and releasing the model only negligible vertical motion occurs, indicating that the manually calculated stress field was accurate (Figure 4.18b; analysis steps 1-2). The application of a test load leads to a downward motion of the column to a new equilibrium position. After removal of the load, the initial position of the model is restored (Figure 4.18b, analysis steps 3-4).

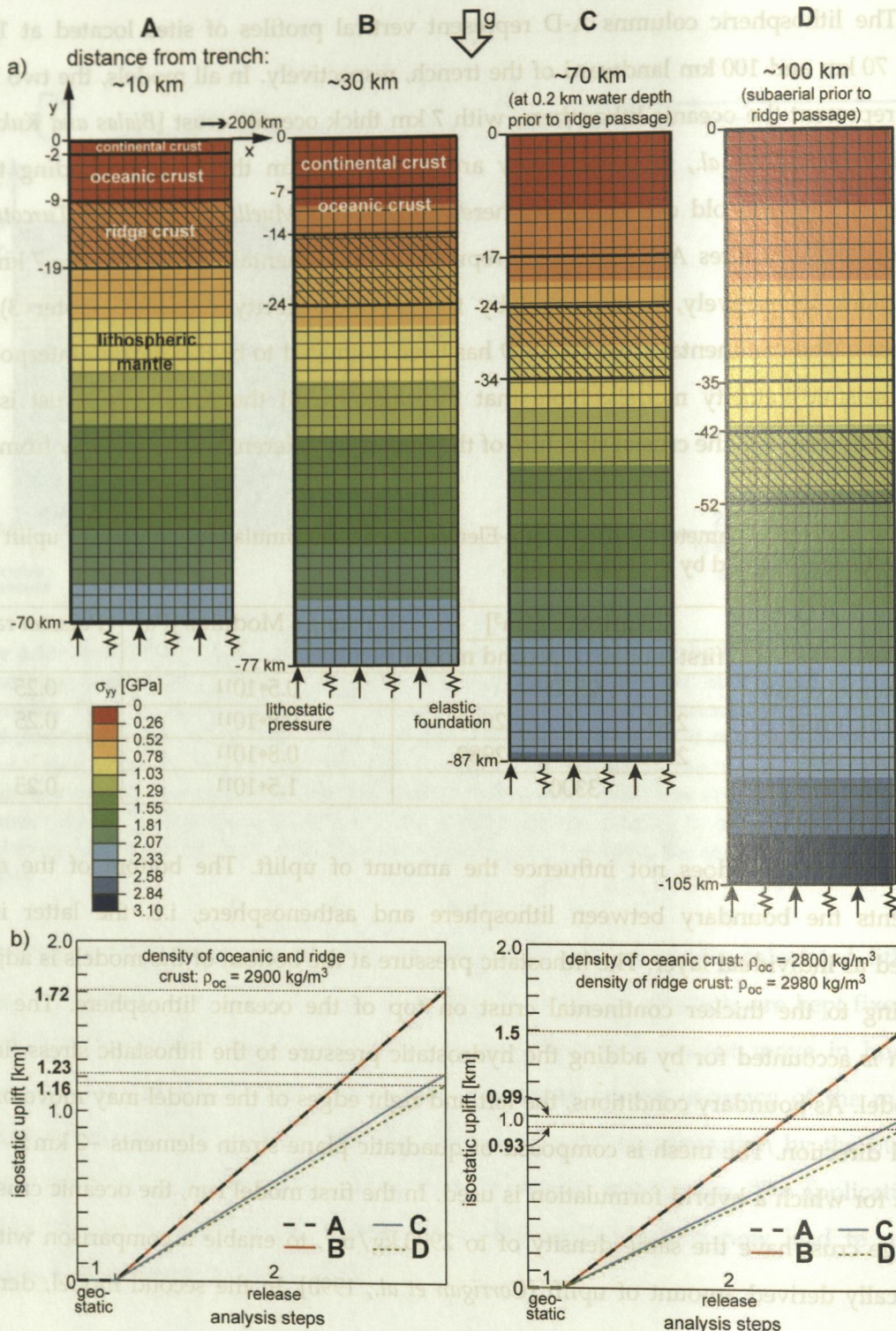
The same approach is applied to a set of four different three-layer models (Figure 4.19). The lithospheric columns A-D represent vertical profiles of sites located at 10 km, 30 km, 70 km and 100 km landward of the trench, respectively. In all models, the two lower layers represent the oceanic lithosphere, with 7 km thick oceanic crust [Bialas and Kukowski, 2000; Krabbenhoft *et al.*, in prep.]. They are together 70 km thick, corresponding to the thickness of ~40 Ma old oceanic lithosphere, as off Peru [Mueller *et al.*, 1995; Turcotte and Schubert, 2002]. At sites A-C, the layers representing continental crust are 2 km, 7 km and 17 km thick respectively, as indicated by the seismic velocity models (chapter 3). The thickness of the continental crust at site D has been estimated to be 35 km from interpolation of the seismic velocity models. Note that the thickness of the continental crust is only included to resemble the crustal structure of the forearc at different distances away from the

Table 4.3: Material parameters for the Finite-Element model set simulating the isostatic uplift of the Peruvian forearc induced by the Nazca Ridge.

	density [kg/m ³]		Young's Modulus [Pa]	Poisson ratio
	first model	second model		
continental crust	2500		0.5*10 ¹¹	0.25
oceanic crust	2900	2800	0.8*10 ¹¹	0.25
ridge crust	2900	2980	0.8*10 ¹¹	-
oceanic mantle	3300		1.5*10 ¹¹	0.25

trench, however, it does not influence the amount of uplift. The bottom of the model represents the boundary between lithosphere and asthenosphere, i.e. the latter is not included as individual layer. The lithostatic pressure at the bottom of the models is adjusted according to the thicker continental crust on top of the oceanic lithosphere. The water column is accounted for by adding the hydrostatic pressure to the lithostatic stress field of the model. As boundary conditions, the left and right edges of the model may move only in vertical direction. The mesh is composed of quadratic plane strain elements ~2 km x ~2 km in size, for which a hybrid formulation is used. In the first model run, the oceanic crust and the ridge crust have the same density of to 2900 kg/m³, to enable a comparison with the analytically derived amount of uplift [Corrigan *et al.*, 1990]. In the second model, densities

from 2800 kg/m^3 and 2980 kg/m^3 are assigned to oceanic and ridge crust, respectively, as inferred from the GEOPECO gravity data [Heinbockel, 2003]. The elastic material parameters of the model layers are listed in Table 4.3 [Turcotte and Schubert, 2002; Huhn, 2002]. After the columns have reached their isostatic equilibrium, the crust of the Nazca Ridge is incorporated by decreasing the density in the upper 10 km of the lithospheric mantle. Thereby, the initial stress field and the boundary conditions are kept constant.



The results show that the first model agrees with the analytically derived isostatic uplift (Figure 4.17; cf. Figure 4.19) and thus, shows the accuracy of the numerical models. Where the amount of uplift does not exceed the water depth, the forearc rises by 1.72 km (A, B), while the forearc that has been subaerial prior to ridge subduction (D) is uplifted by 1.16 km (Figure 4.19b). For a paleo-water depth of 0.2 km, the amount of uplift is 1.23 km. In the second model run, using the refined density distribution, the submarine and subaerial endmember models (A, B, D) experience uplift of 1.5 km and 0.93 km, respectively. Site C at a paleo-water depth of 0.2 km rises by 0.99 km.

4.2.4 Deformation of the upper plate caused by oblique ridge subduction

While the Nazca Ridge moves along the Peruvian margin, it induces a propagating wave of uplift and subsidence on the forearc, as illustrated by the marine terraces along the South Peruvian coast [Hsu, 1992; Macharé and Ortlieb, 1992] and the analogue models (section 4.1). Three 2D models have been carried out to investigate the stress field in the upper plate induced by the laterally migrating ridge and friction along the plate interface. They are complemented by a 3D model that accounts for the obliquity of ridge subduction.

The 2D models consist of a continental block representing a 500 km long section of the continental crust along the Peruvian coast (Figure 4.20). The thickness and the density of the continental block along the coast are estimated to be 17 km and 2700 kg/m^3 , respectively, from the seismic velocity and density models [chapter 3; Bialas and Kukowski, 2000; Heinbockel, 2003; Krabbenhoft *et al.*, in prep.]; self-gravitation is not included into the model. The continental crust rests on the right half of a 1000 km-long oceanic plate, which carries a 1.5 km high ridge 200 km width on the left side. The friction at the interface between upper and lower plate is varied from $\mu_b = 0$ to $\mu_b = 0.6$. The latter value corresponds to the basal friction inferred for Peru from a critical taper analysis [Davis *et al.*, 1983] and has also been used in the 3D sandbox experiments (section 4.1). During the model run, the oceanic plate,

←

Figure 4.19: a) Sections of the models used to calculate the isostatic uplift caused by the thick buoyant Nazca Ridge at sites A, B, C, D located 10 km, 30 km, 70 km and 100 km landward of the trench, respectively. Crustal thicknesses of A-C are taken from the seismic velocity models (chapter 3). Thickness of the continental crust at site D in the Coastal Cordillera has been estimated. Colour code refers to the internal stress field of the columns. b) Left plot: Using a density of 2900 kg/m^3 for both, oceanic and ridge crust, leads to isostatic uplift of 1.72 km if the forearc remains submarine (A, B). A previously subaerial forearc rises by 1.16 km (D). A forearc covered by water column of 0.2 km experiences uplift of 1.23 km. Right plot: Assigning densities of 2800 kg/m^3 to the oceanic crust and 2980 kg/m^3 to the ridge crust as indicated by the GEOPECO gravity data [Heinbockel, 2003] reduces the amounts of uplift by ~ 0.2 km.

for which vertical motion is prohibited, is displaced by 500 km to the right. In order to prevent unintended motion of the upper plate, which would otherwise be induced by the drag of the lower plate, the continental crust is fixed at its upper corners.

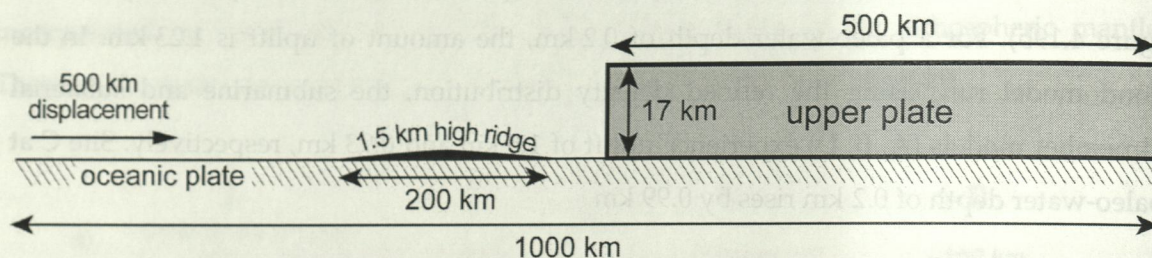


Figure 4.20: Geometry of three 2D models that have been carried out to determine the stress field in the upper plate induced by the laterally migrating ridge and a frictional interface between upper and lower plate. The oceanic plate is treated as a rigid body. The continental block, which is fixed in horizontal direction at its upper corners, is meshed with 0.5 km x 0.5 km large elements.

Several simplifications are necessary to facilitate the computation of the frictional contact between the upper and lower plate in order to ensure convergence of the analysis [Hibbitt *et al.*, 2002]. First, the oceanic plate and ridge are treated as rigid bodies, i.e. they may not deform. Second, to prevent opening of the contact between the two model parts during the motion of the lower one, the ridge has a smooth topography and the upper plate has a fine mesh of 0.5 km x 0.5 km large elements. Plane strain elements with a linear formulation and of incompatible mode are used, as recommended by Hibbitt *et al.* [2002]. Third, a purely elastic rheology is chosen. The elastic modulus of the continental crust is set to 0.5×10^{11} Pa. Test runs have also been performed using a Mohr-Coulomb rheology, with the goal to enable a closer comparison with the sandbox models, however, due to an immensely increased computational effort exceeding the available computer memory, the analyses aborted as soon as the ridge flank began to underthrust the continental block.

The results of the three 2D models after 400 km of convergence show that the displacement fields of all three models mirror the topography of the underthrusting ridge (Figure 4.21a), while the stress field changes significantly with increasing friction along the interface between continental block and oceanic plate. In the first model, the plate interface is frictionless (Figure 4.21b). In this case, the stress field above the laterally moving ridge remains symmetric throughout the model run. The maximum and minimum principal stresses indicate that the upper part of the continental plate located above the ridge experiences tension (Figure 4.21b). Low compressional stress is observed in the lower half of the continental block and above the flanks of the ridge. In the second and third model, the presence of intermediate and high basal friction, respectively, results in an increasing asym-

metry of the stress field (Figure 4.21c-d). The tensional stress in the upper continental crust increases, as indicated by increasing minimum principal stress, compared to the frictionless model (Figure 4.21b-d). Moreover, the presence of a frictional interface leads to compression in the upper plate in front of the leading ridge flank, while tension prevails above the trailing flank. The stress maxima above the edges of the ridge in all three models are caused by the rise in the topography of the oceanic plate and must be interpreted with caution.

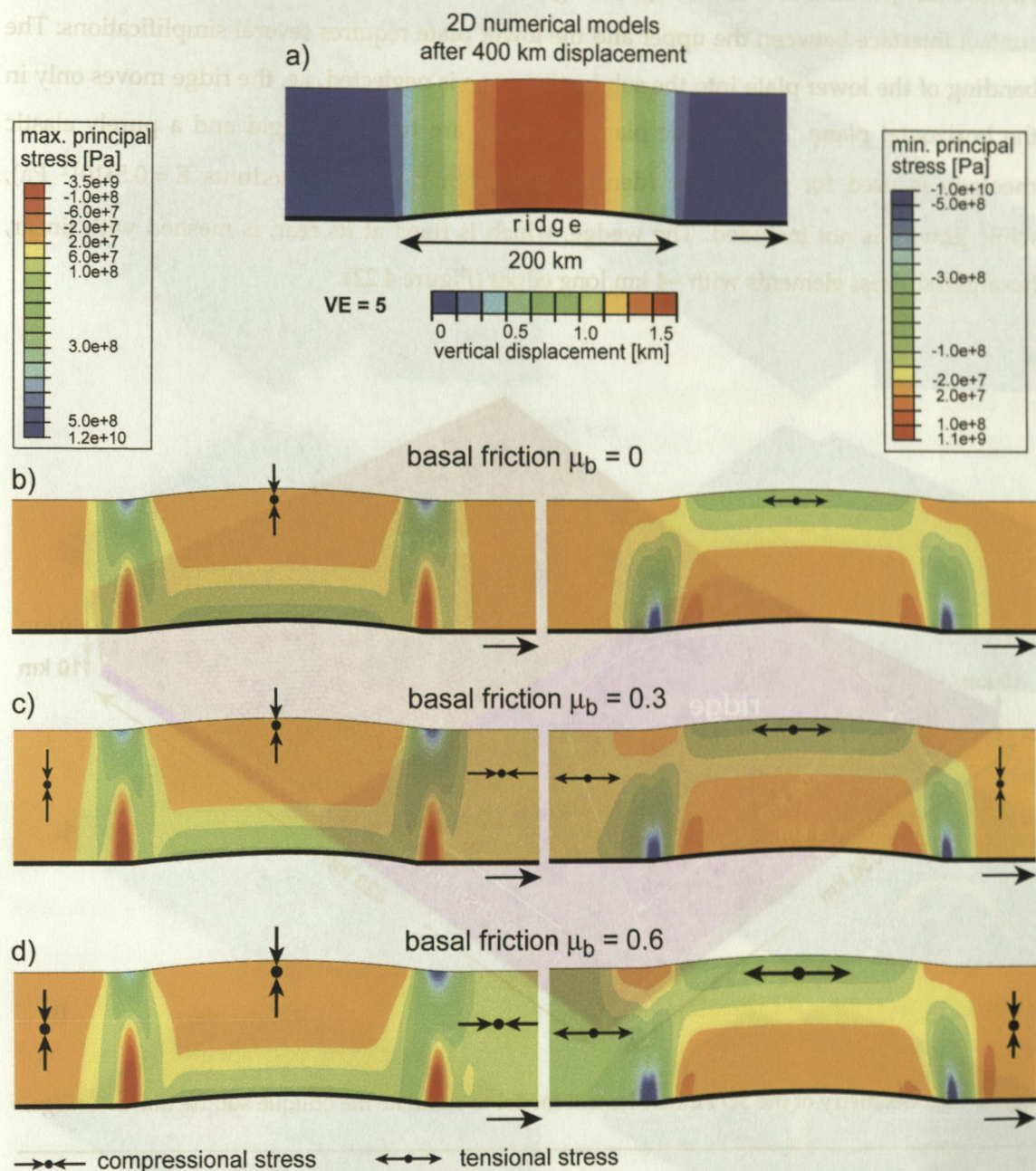


Figure 4.21: Results of the 2D models showing the displacement and stress fields in the upper plate after 400 km lateral displacement of the ridge for different friction coefficients at the interface between the upper and lower plates (vertical exaggeration VE = 5). a) The displacement fields in all three models mirror the topography of the underthrusting ridge. The friction on the interface is b) zero, c) intermediate, and d) high. Note the tension in the upper plate above the ridge and the increasing asymmetry in the stress fields with increasing friction.

The 3D model has been designed to account for effects caused by the obliquity of ridge subduction. The model consists of a wedge-shaped upper plate, beneath which an oceanic plate subducts, carrying a 1.5 km high ridge of smooth topography (Figure 4.22). In the model, the ridge is at an angle of 35° to the convergence direction of the plate, equivalent to the Nazca Ridge off Peru. The amount of convergence during the model run is 170 km, which translates into 2.5 Ma using the convergence velocity of 68 mm/a at 17°S for the Nazca Plate [Norabuena *et al.*, 1998]. Analogous to the 2D models, the implementation of the contact interface between the upper and the lower plate requires several simplifications: The bending of the lower plate into the subduction zone is neglected, i.e. the ridge moves only in the horizontal plane. The oceanic plate and ridge are treated as rigid and a purely elastic rheology is used for the wedge (density 2700 kg/m^3 ; Young's modulus $E = 0.5 \cdot 10^{11} \text{ Pa}$), while gravity is not included. The wedge, which is fixed at its rear, is meshed with linear, hexahedral stress elements with $\sim 4 \text{ km}$ long edges (Figure 4.22).

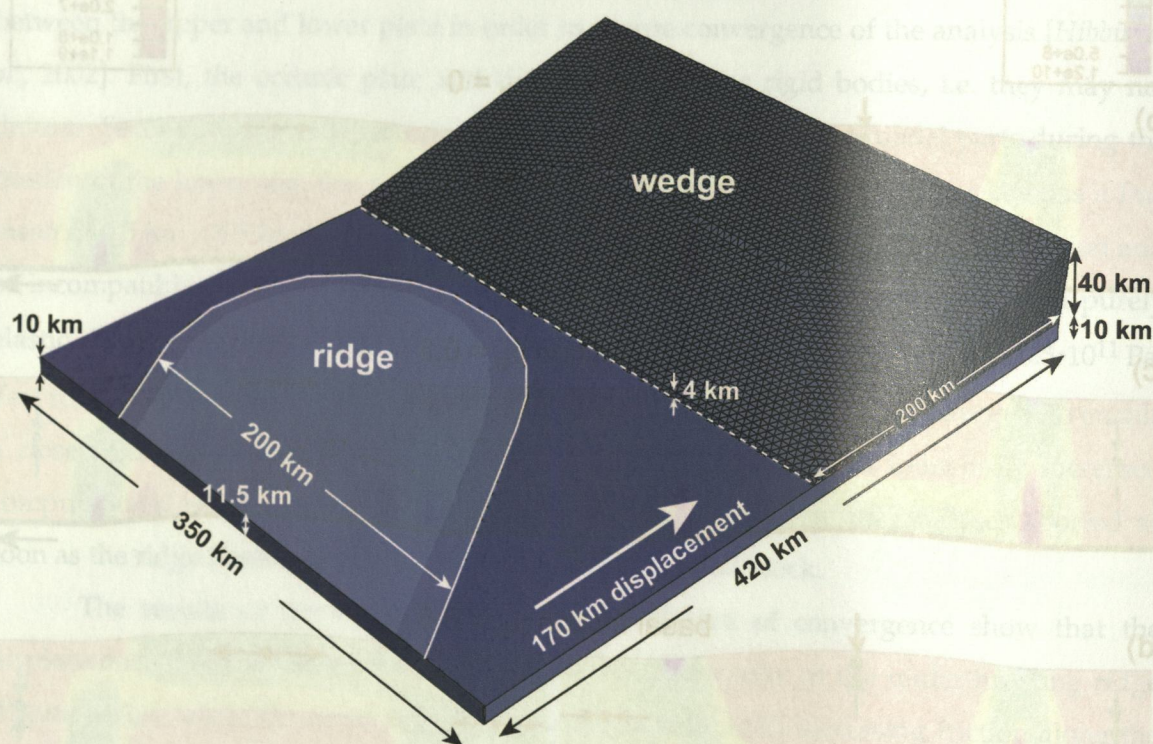
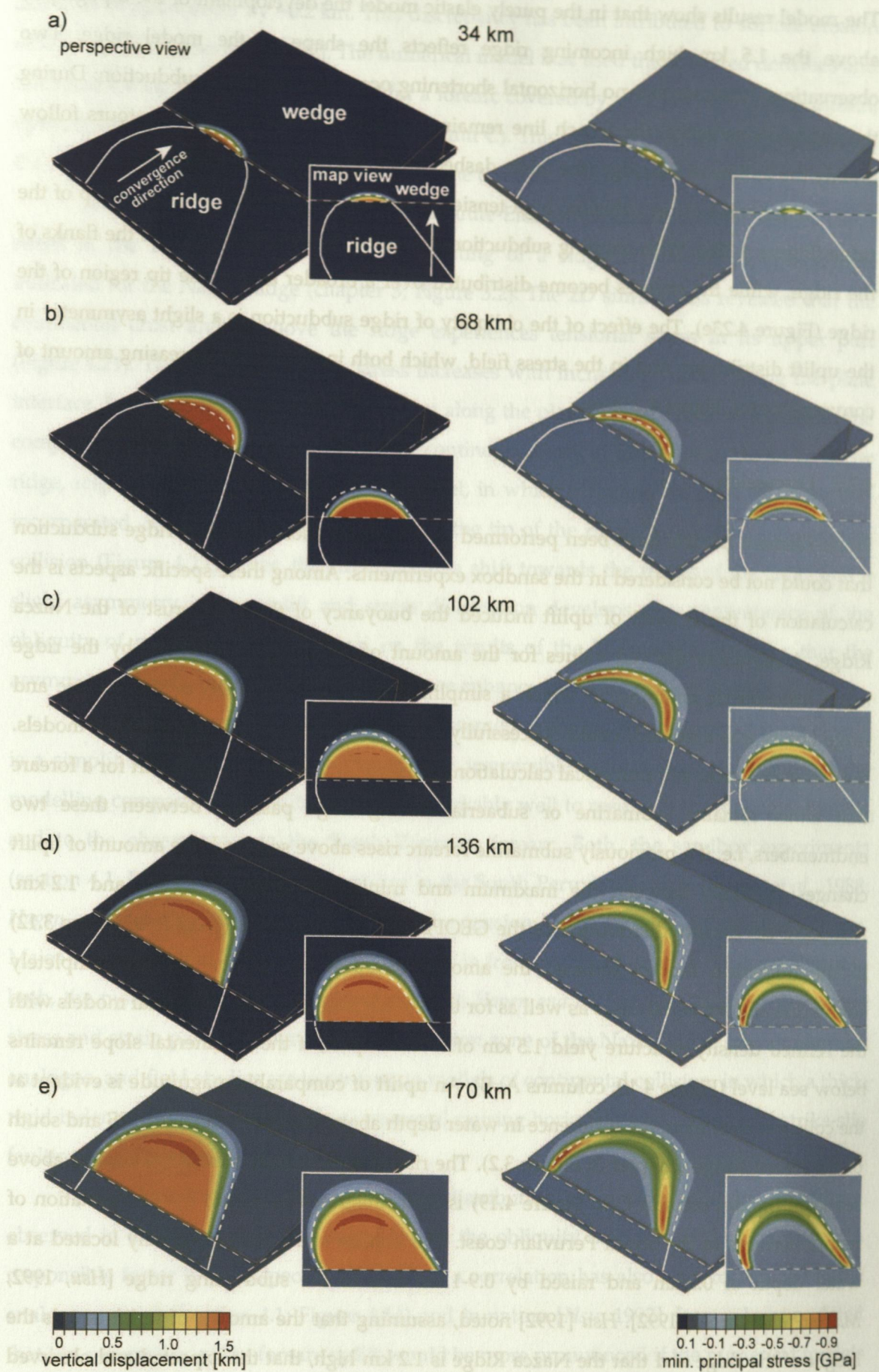


Figure 4.22: Geometry of the 3D Finite-Element model to simulate the oblique subduction of a ridge.

Figure 4.23: Results of the 3D model without friction on the interface between oceanic plate and wedge. The model is shown at 5 stages up to 170 km of convergence. The left column shows the vertical displacement of the upper plate due to underthrusting of the ridge. The right column exhibits the minimum principal stress. The wedge experiences extension at the tip and above the flanks of the ridge. Note that stress maxima at the edges of the wedge are caused by the rise in topography on the oceanic plate and must be interpreted with caution.



The model results show that in the purely elastic model the development of the topography above the 1.5 km high incoming ridge reflects the shape of the model ridge. Two observations illustrate that no horizontal shortening occurs during ridge subduction: During the entire convergence, the trench line remains straight and the elevation contours follow exactly the outline of the ridge (the white dashed line in Figure 4.23 left column).

After onset of the collision, high tensional stresses occur around the curved tip of the ridge (Figure 4.23a). With ongoing subduction, the stress maxima shift towards the flanks of the ridge, while the stresses become distributed over a broader area at the tip region of the ridge (Figure 4.23e). The effect of the obliquity of ridge subduction is a slight asymmetry in the uplift distribution and in the stress field, which both increase with increasing amount of convergence (cf. Figure 4.23b-e).

4.2.5 Discussion

Finite-Element models have been performed to investigate those effects of ridge subduction that could not be considered in the sandbox experiments. Among these specific aspects is the calculation of the amount of uplift induced the buoyancy of the thick crust of the Nazca Ridge. Analytically derived values for the amount of forearc uplift induced by the ridge using lithospheric columns, in which a simplified density distribution of the oceanic and ridge crusts was assumed, could successfully be reproduced by the Finite-Element models. Both, the analytical and numerical calculations indicate 1.7 km and 1.2 km uplift for a forearc that either remains submarine or subaerial during ridge passage. Between these two endmembers, i.e. if a previously submarine forearc rises above sea level, the amount of uplift changes gradually between the maximum and minimum values of 1.7 km and 1.2 km. Adopting the density distribution of the GEOPECO density models (chapter 3; Figure 3.12) in the numerical models reduced the amount of uplift by ~0.2 km for the completely submarine and subaerial cases as well as for the transitional case. The numerical models with the refined density structure yield 1.5 km of forearc uplift, if the continental slope remains below sea level (Figure 4.19, columns A, B). An uplift of comparable magnitude is evident at the collision zone from the difference in water depth above the lower slope at 15°S and south of the Nazca Ridge (chapter 3; Figure 3.2). The rise of a previously submarine forearc above sea level (model column C in Figure 4.19) is well illustrated in nature by the formation of marine terraces at the South Peruvian coast. The marine strata were originally located at a water depth of 0.2 km and raised by 0.9-1 km due to the subducting ridge [Hsu, 1992; Macharé and Ortlieb, 1992]. Hsu [1992] noted, assuming that the amount of uplift equals the height of the ridge and that the Nazca Ridge is 1.2 km high, that the expected and observed

amounts of uplift differ by ~ 0.2 km. This discrepancy has been attributed to surface erosion of the marine terraces [Hsu, 1992]. The numerical model that used the observed densities and thickness for the ridge crust shows that for a forearc covered by a 0.2 km high water column, uplift of 0.99 km is expected (Figure 4.19, column C). This amount of uplift agrees well with the observed elevations of 0.9–1 km of the marine terraces.

A different set of three 2D and one 3D Finite-Element models investigated the state of stress in the upper plate during underthrusting of a ridge of smooth topography, as indicated for the Nazca Ridge (chapter 3; Figure 3.2). The 2D simulations revealed that the continental crust arched above the ridge experiences tensional stress in its upper part (Figure 4.21). The magnitude of the stress increases with increasing friction along the plate interface. Furthermore, an increase in friction along the plate interface results in a rise of the compressional and tensional stresses in the continental block in front and in the wake of the ridge, respectively. According to the 3D model, in which a frictionless plate interface was incorporated, tensional stresses occur around the tip of the ridge during the first stages of collision (Figure 4.23). Later, the stress maxima shift towards the flanks of the ridge and a slight asymmetry in the uplift and stress distribution develops as a consequence of the obliquity of ridge subduction. Based on the results of the 2D models, it seems that the asymmetry in both, uplift and stress pattern are enhanced with increasing friction.

Although the purely elastic rheology assigned to the continental model plate clearly is a simplification and inherently prevents an irreversible deformation, the results of the modelling compare, in a qualitative way, remarkably well to results of the analogue models and to the observations in the South Peruvian forearc. Both, the sandbox experiments (section 4.1; Figure 4.14) and field studies in the South Peruvian forearc [Sébrier *et al.*, 1988; Hagen and Moberly, 1994] indicate horizontal extension in the forearc of the collision zone. Major compression-induced structures above or in front of the subducting ridge are absent in both, the models and nature [Sébrier *et al.*, 1988; Hagen and Moberly, 1994]. These consistent stress and strain patterns inferred for the collision zone of the Nazca Ridge from numerical, analogue, and field studies are in contrast to models of continental collision, in which a thick, rigid indenter is pushed into a plastic material causing horizontal shortening and strike-slip faulting [e.g. Tapponnier and Molnar, 1976].

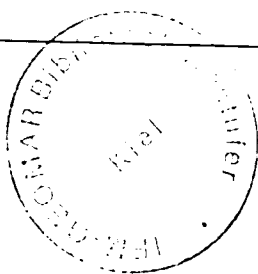
A tendency towards an asymmetric distribution of forearc uplift has only been observed in the 3D model. This suggests that the obliquity of ridge subduction may be a responsible factor for this specific effect. Such a correlation has also been recognized in the analogue models (section 4.1; Figure 4.14) and in nature [Hsu, 1992]. It may be speculated that the asymmetry of the forearc uplift would be more pronounced if the numerical models

were calculated with a rheology accounting for plastic irreversible deformation. A comparison with the 2D model suggests that the incorporation of friction along the plate interface into the 3D model might lead to compressional stresses in the upper plate in front of the leading ridge flank. Such a state of stress could promote the localisation of maximum uplift above the leading ridge flank (cf. Figures 4.21, 4.23). In nature, a high basal friction between the South American and Nazca plates is indicated by the repeated occurrence of strong earthquakes with hypocenters located above the Nazca Ridge [Spence *et al.*, 1999; Swenson and Beck, 1999].

4.2.6 Conclusions of the numerical modelling

Finite-Element modelling has allowed to quantify the amount and spatial distribution of uplift and to investigate the stress field induced by the oblique subduction of the Nazca Ridge in South Peru. The numerical models, in which the density distribution is constrained by gravity data, predict that those parts of the forearc that remain submarine or subaerial rise by 1.5 km and 0.93 km, respectively. A forearc covered by 0.2 km water prior to the ridge passage experiences 0.99 km of uplift. These results compare favourably with the amount of uplift observed off- and onshore in the South Peruvian forearc.

The main response of the elastic upper plate to underthrusting of the model ridge (with dimensions similar to the Nazca Ridge) is uplift and horizontal tension. The 2D models, designed to simulate the dynamic effects of lateral ridge motion along the Peruvian margin, demonstrate that with increasing friction on the interface between the two plates an increasingly asymmetric stress pattern develops in the upper plate: compression prevails above the leading ridge flank, while tension occurs above the trailing flank. The 3D model indicates that it is the obliquity of ridge subduction that is responsible for the asymmetric uplift and stress distributions. Although the elastic rheology applied in the numerical models does not take into account irreversible plastic deformation, the modelling results agree with the analogue models and field studies, both indicating an asymmetric uplift pattern and the predominance of extensional faulting in the forearc above the Nazca Ridge.



Südamerika ist krumm.

Johann August Galletti (1750-1828)

5 Conclusions

On timescales of tens of million years, mountain belts along convergent margins may evolve towards an equilibrium state, which may include flux-, topographic-, thermal-, or exhumational steady states [e.g. Willett and Brandon, 2002]. However, the subduction of obstacles, such as seamounts, oceanic plateaus, or aseismic ridges, causes the orogenic system to shift away from any equilibrium state it may have attained earlier. Understanding how such complex geodynamic systems behave under rapidly changing boundary conditions clearly requires a multidisciplinary approach.

Recently acquired geophysical data and a new reconstruction of the migration history of the Nazca Ridge using updated relative plate motions, GPS-, and ODP-data, has set the stage for such a multidisciplinary study in the collision zone of the Nazca Ridge with the Andean continental margin. By combining the geophysical data with 3D sandbox experiments and Finite-Element modelling, the factors controlling the mass-transfer regime, style of faulting, and distribution and amount of surface uplift, have been tightly constrained for the collision zone of the Nazca Ridge. It could be shown that the passage of the ridge causes enhanced tectonic erosion at the long-term erosive margin of South Peru. This erosive regime, which may have prevailed for tens of million years, led to the presence of mechanically strong crystalline rocks close to the trench, which have prevented a deep indentation of the frontal wedge by the Nazca Ridge. The important role of the mechanical strength of the frontal wedge has also been confirmed in two sandbox models by using analogue materials of different strength.

The oblique subduction of the ridge has induced a wave of transient uplift and intensified deformation propagating along the Peruvian forearc. The distribution of surface uplift above the ridge, as recorded by raised marine terraces, is asymmetric, with the maximum amount of uplift and the highest uplift rates being offset relative to the ridge crest. This dynamic behaviour of the system has also been highlighted in the sandbox experiments, owing to the powerful image correlation system PIV, which significantly increased the temporal and spatial resolution of the analogue models. The numerical model has shown that ridge subduction causes tension above the ridge, which is in agreement with the development of oblique normal faults that propagate from the collision zone in the sandbox models. A neotectonic study has indeed detected active normal faults in the Peruvian forearc above the Nazca Ridge [Sébrier *et al.*, 1988].

Important predictions of the analogue and numerical models remain to be tested in future investigations. The most crucial ones are the detailed style of deformation and surficial mass wasting in the upper plate during ridge subduction, and the separation of these ridge-induced effects from long-term processes. Offshore, this may be achieved by acquiring high-resolution bathymetric and seismic data at both, the present collision zone and the poorly known forearc south of the Nazca Ridge, which has not yet been affected by the ridge. To enable a correlation between the stratigraphy imaged in the seismic sections and geologic units, the forearc at and south of the collision zone should be drilled. Such data would complement the existing data sets of ODP Leg 112 and the GEOPECO project in a favourable way, and, all together, would help to resolve the spatial and temporal evolution of the forearc system before, during, and after ridge subduction.

The uplift of marine rocks above sea level and the presence of young active faults in South Peru illuminates that the impact of a subducting aseismic ridge on the forearc is reflected in the geomorphology, neotectonics, and exhumation patterns onshore. Valuable information is to be expected from deriving cooling and exhumation rates using apatite fission track and (U-Th)/He dating [cf. Wolf *et al.*, 1997; House *et al.*, 1998; Spikings *et al.*, 2001; Wipf *et al.*, 2001], quantifying the style and rates of Quaternary faulting [cf. Siame *et al.*, 1997], dating marine terraces [cf. Perg *et al.*, 2001], as well as studying the evolution of the landscape above the subducted part of the ridge [cf. Burbank *et al.*, 1999]. In particular, the development of drainage systems and the shape of river profiles may provide insight into the spatial distribution of uplift across active faults [cf. Kirby and Whipple, 2001]. Integrating off- and onshore data will lead to considerable improvements in assessing the complex problems posed by active margins.

An integrated off- and onshore data set would help to underpin and refine future analogue and numerical models. Since modelling implicitly requires simplification of the actual geological system, testing against field data is inevitable to achieve meaningful results. The potential of combining analogue and numerical modelling techniques is expected to increase significantly by fully linking them using digital monitoring systems. The capability of these particle imaging velocimetry systems to calculate the 3D displacement field in analogue models enables to derive the strain and velocity fields in three dimensions and directly compare them with the output of the numerical models. Thus, with increasing computer capacities, numerical modelling should be rigorously pursued in three dimensions, to calculate 3D stress fields and to take into account material movements out-of-section, which in general cannot be neglected. Apart from that, more realistic rock rheologies, temporally changing temperature fields, and friction along the interface between upper and downgoing plate should be implemented.

6 References

- Adam, J., J. Urai, B. Wienecke, O. Oncken, N. Kukowski, J. Lohrmann, S. Hoth, W. van der Zee, and J. Schmatz, High-resolution strain analysis in scaled sandbox experiments by optical image correlation (PIV): a first look, in prep.
- Adam, J., N. Kukowski, J. Lohrmann, and O. Oncken, Mass transfer patterns and kinematics of tectonic erosive convergent margins: quantitative results from analogue sandbox experiments and their implications for natural forearc systems, submitted.
- Adam, J., and C.-D. Reuther, Crustal dynamics and active fault mechanics during subduction erosion. Application of frictional wedge analysis on the North Chilean Forearc, *Tectonophysics*, 321, 297-325, 2000.
- Angermann, D., J. Klotz, and C. Reigber, Space-geodetic estimation of the Nazca-South America Euler vector, *Earth Planet. Sci. Lett.*, 171, 329-334, 1999.
- Ballance, P.F., D.W. Scholl, T.L. Vallier, A.J. Stevenson, H. Ryan, and R.H. Herzer, Subduction of a Late Cretaceous seamount of the Louisville Ridge at the Tonga Trench: A model of normal and accelerated tectonic erosion, *Tectonics*, 8, 5, 953-962, 1989.
- Barazangi, M., and B. Isacks, Spatial distribution of earthquakes and subduction of the Nazca plate beneath South America, *Geology*, 4, 686-692, 1976.
- Beaumont C., S. Ellis, and A. Pfiffner, Dynamics of sediment subduction-accretion at convergent margins: Short-term modes, long-term deformation, and tectonic implications, *J. Geophys. Res.*, 104, B8, 17573-17601, 1999.
- Bebout, G.E., D.W. Scholl, S.H. Kirby, and J.P. Platt, Subduction Top to Bottom, *AGU Geophys. Monogr.*, 96, 1996.
- Bialas, J., and N. Kukowski, Geophysical experiments at the Peruvian continental margin; investigations of tectonics, mechanics, gas hydrates and fluid transport, *Geomar Rpt. 96*, Geomar, Kiel, 2000.
- Bialas, J., and E. Flueh, Ocean Bottom Seismometers, *Sea Technology*, 40, 4, 41-46, 1999.
- Bouysse, P., and D. Westercamp, Subduction of Atlantic aseismic ridges and Late Cenozoic evolution of the Lesser Antilles island arc, *Tectonophysics*, 175, 349-380, 1990.
- Branlund, J.M., K. Regenauer-Lieb, and D.A. Yuen, Weak zone formation for initiating subduction from thermo-mechanical feedback of low-temperature plasticity, *Earth Planet. Sci. Lett.*, 190, 237-250, 2001.
- Branlund, J.M., K. Regenauer-Lieb, and D.A. Yuen, Fast ductile failure of passive margins from sediment loading, *Geophys. Res. Lett.*, 27, 1989-1993, 2000.
- Buiter, S.J.H., R. Govers, and M.J.R. Wortel, A modelling study of vertical surface displacements at convergent plate margins, *Geophys. J. Intern.*, 147, 415-427, 2001.
- Buiter, S.J.H., Surface deformation resulting from subduction and slab detachment, *Geologica Ultraiectina*, 191, 2000.

- Burbank, D.W., J.K. McLean, M. Bullen, K.Y. Abdrakhmatov, and M.M. Miller, Partitioning of intermontane basins by thrust-related folding, Tien Shan, Kyrgyzstan, *Basin Research*, 11, 75-92, 1999.
- Byerlee, J., Friction of rocks, *Pure Appl Geophys.*, 116, 615-626, 1978.
- Cande, S.C., and D.V. Kent, Revised calibration of the geomagnetic timescale for the Late Cretaceous and Cenozoic, *J. Geophys. Res.* 100, 6093-6095, 1995.
- Cande, S.C., and W.F. Haxby, Eocene propagating rifts in the Southwest Pacific and their conjugate features on the Nazca Plate, *J. Geophys. Res.*, 96, 19609-19622, 1991.
- Cande, S.C., J.L. LaBreque, R.L. Larson, and W.C. Pitman, Magnetic lineations of the world's ocean basins, Map with text, AAPG, Tulsa, Okl., 1989.
- Cande, S.C., Nazca-South American Plate interactions since 50mybp, in: D.M. Hussong, S.P. Dang, L.D. Kulm, R.W. Couch, T.W.C. Hilde (Eds), Peru continental margin, *Mar. Sci. Intern.*, Woods Hole, MA, 1985.
- Caress, D.W., and D.N. Chayes, New software for processing sidescan data from sidescan-capable multibeam sonars, *Proceedings of the IEEE Oceans 95 Conference*, 997-1000, 1995.
- Carr, J.R., Numerical Analysis for the Geological Sciences, *Prentice Hall*, 1995.
- Cattin, R., H. Lyon-Caen, and J.Chery, Quantification of interplate coupling in subduction zones and forearc topography, *Geophys. Res. Lett.*, 24, 13, 1563-1566, 1997.
- Chapple, W.M., Mechanics of thin-skinned fold-and-thrust belts, *Geol. Soc. Am. Bull.*, 89, 1189-1198, 1978.
- Chung, W.Y., and H. Kanamori, A mechanical model for plate deformation associated with aseismic ridge subduction in the New Hebrides Arc, *Tectonophysics*, 50, 1, 29-40, 1978.
- Clift, P.D., I. Pecher, N. Kukowski, and A. Hampel, Tectonic erosion of the Peruvian Forearc, Lima Basin, by subduction and Nazca Ridge collision, *Tectonics*, in press.
- Clift, P.D., and C.J. MacLeod, Slow rates of subduction erosion estimated from subsidence and tilting of the Tonga forearc, *Geology*, 27, 5, 411-414, 1999.
- Cloos, M., Lithospheric buoyancy and collisional orogenesis: Subduction of oceanic plateaus, continental margins, island arcs, spreading ridges and seamounts, *Geol. Soc. Am. Bull.*, 105, 715-737, 1993.
- Cloos, M., Thrust-type subduction-zone earthquakes and seamount asperities: a physical model for seismic rupture, *Geology*, 20, 7, 601-604, 1992.
- Cloos, M., and R.L. Shreve, Subduction-channel model of prism accretion, melange formation, sediment subduction, and subduction erosion at convergent plate margins; Part I, Background and description, *Pure Appl. Geophys.*, 128 (3-4), 455-500, 1988a.
- Cloos, M., and R.L. Shreve, Subduction-channel model of prism accretion, melange formation, sediment subduction, and subduction erosion at convergent plate margins; Part II, Implications and discussion, *Pure Appl. Geophys.*, 128 (3-4), 501-545, 1988b.
- Cobbold, P.R., S. Durand, and R. Mourgues, Sandbox modelling of thrust wedges with fluid-assisted detachments, *Tectonophysics*, 334, 245-258, 2001.

- Cobbold, P.R., and L. Castro, Fluid pressure and effective stress in sandbox models, *Tectonophysics*, 301, 1-19, 1999.
- Collot, J.-Y., and B. Davy, Forearc structures and tectonic regimes at the oblique subduction zone between the Hikurangi Plateau and the southern Kermadec margin, *J. Geophys. Res.*, 103, B1, 623-650, 1998.
- Collot, J.-Y., and M.A. Fisher, The collision zone between the North d'Entrecasteaux ridge and the New Hebrides island arc, 1. Sea Beam morphology and shallow structure, *J. Geophys. Res.*, 96, B3, 4479-4495, 1991.
- Collot, J. Y., and M.A. Fisher, Formation of forearc basins by collision between seamounts and accretionary wedges: an example from the New-Hebrides subduction zone, *Geology*, 17, 930-933, 1989.
- Conrad C.P., and B.H. Hager, Effects of plate bending and fault strength at subduction zones on plate dynamics, *J. Geophys. Res.*, 104, B8, 17551-17571, 1999.
- Corrigan, J., P. Mann, and J.C. Ingle, Forearc response to subduction of the Cocos Ridge, Panama-Costa Rica, *Geol. Soc. Am. Bull.*, 102, 628-652, 1990.
- Couch, R., and R.M. Whitsett, Structures of the Nazca Ridge and the continental shelf and slope of southern Peru, in *Nazca Plate: Crustal Formation and Andean Convergence* edited by L.D. Kulm, J. Dymond, E.J. Dasch, and D.M. Hussong, *Geol. Soc. America Mem.* 154, 569-586, 1981.
- Coulburn, W.T., Tectonics of the Nazca Plate and the continental margin of western South America, 18°S to 23°S, in *Nazca Plate: Crustal Formation and Andean Convergence* edited by L.D. Kulm, J. Dymond, E.J. Dasch, and D.M. Hussong, *Geol. Soc. America Mem.* 154, 587-618, 1981.
- Dahlen, J.S.F., Critical taper model of fold-and-thrust belts and accretionary wedges, *Annu. Rev. Earth. Planet. Sci.*, 55-99, 1990.
- Dahlen, J.S.F., Non-cohesive Critical Coulomb wedges: an exact solution, *J. Geophys. Res.*, 89, B12, 10125-10133, 1984.
- Dahlen, J.S.F., J. Suppe, and D. Davis, Mechanics of fold-and-thrust belts and accretionary wedges: cohesive Coulomb theory, *J. Geophys. Res.*, 89, B12, 10087-10101, 1984.
- Davies, J.H., Simple analytic model for subduction zone thermal structure, *Geophys. J. Intern.*, 139, 3, 823-828, 1999.
- Davis, E.E., and R.D. Hyndman, Accretion and recent deformation of sediments along the northern Cascadia subduction zone, *Geol. Soc. Am. Bull.*, 101, 1465-1480, 1989.
- Davis, D.M., J. Suppe, and J.S.F. Dahlen, Mechanics of fold-and-thrust belts and accretionary wedges, *J. Geophys. Res.*, 88, B2, 1153-1172, 1983.
- DeMets, C., R.G. Gordon, D.F. Argus, and S. Stein, Current plate motions, *Geophys. J. Intern.*, 101, 425-478, 1990.
- Dmowska, R., G. Zheng, and J.R. Rice, Seismicity and deformation at convergent margins due to heterogeneous coupling, *J. Geophys. Res.*, 101, B2, 3015-3029, 1996.
- Dominguez, S., S. Lallemand, J. Malavieille, and P. Schnuerle, Oblique subduction of the Gagua Ridge beneath the Ryukyu accretionary wedge system: Insights from marine observations and

- sandbox experiments, *Mar. Geophys. Res.*, 20, 383-402, 1998.
- Ellis S., C. Beaumont, and O.A. Pfiffner, Geodynamic models of crustal-scale episodic tectonic accretion and underplating in subduction zones, *J. Geophys. Res.*, 104, B7, 15169-15190, 1999.
- Fagan, M.J., Finite Element analysis: Theory and Practice, *Longman Scientific and Technical*, Harlow, 1992.
- Fischer, K.D., Dreidimensionale Modellierung der synorogenen Entwicklung des Variszischen Vorlandbeckens mit der Finite-Elemente-Methode, *Jenaer Geowiss. Schriften*, 2001.
- Fisher, M.A., J.-Y. Collot, and E.L. Geist, The collision zone between the North d'Entrecasteaux ridge and the New Hebrides island arc, 2. structure from multichannel seismic data, *J. Geophys. Res.*, 96, B3, 4470-4495, 1991.
- Fleitout, L., and C. Froidevaux, Tectonic stress in the lithosphere, *Tectonics*, 2, 315-324, 1983.
- Flueh, E.R., M.A. Fisher, J. Bialas, J.R. Childs, D. Klaeschen, N. Kukowski, T. Parsons, D.W. Scholl, U. ten Brink, A.M. Trehu, and N. Vidal, New seismic images of the Cascadia subduction zone from cruise SO108-ORWELL, *Tectonophysics*, 293, 69-84, 1998.
- Flueh, E.R., and J. Bialas, A digital, high data capacity ocean bottom recorder for seismic investigations, *Int. Underwater Systems Design*, 18, 3, 18-20, 1996.
- Gabriel, G., T. Jahr, G. Jentzsch, and J. Melzer, Deep structure and evolution of the Harz Mountains: results from three-dimensional gravity and finite-element modeling, *Tectonophysics*, 270, 279-299, 1997.
- Gardner, T.W., D. Verdonck, N.M. Pinter, R. Slingerland, K.P. Furlong, T.F. Bullard, and S.G. Wells, Quaternary uplift astride the aseismic Cocos Ridge, Pacific coast, Costa Rica, *Geol. Soc. Am. Bull.*, 104, 219-232, 1992.
- Geist, E.L., M.A. Fisher, and D.W. Scholl, Large-scale deformation associated with ridge subduction, *Geophys. J. Intern.*, 115, 344-366, 1993.
- Gerbault, M., F. Davey, and S. Henrys, Three-dimensional lateral crustal thickening in continental oblique collision: an example from the Southern Alps, New Zealand, *Geophys. J. Intern.*, 150, 770-779, 2002.
- Grant, J.A., and R. Schreiber, Modern swath sounding and sub-bottom profiling technology for research applications: The Atlas Hydrosweep and Parasound systems, *Mar. Geophys. Res.*, 12, 9-19, 1990.
- Gutscher, M.-A., W. Spakman, H. Bijwaard, and E.R. Engdahl, Geodynamics of flat subduction: Seismicity and tomographic constraints from the Andean margin, *Tectonics*, 19, 5, 814-833, 2000.
- Gutscher, M.-A., J. Malavieille, S. Lallemand, J.-Y. Collot, Tectonic segmentation of the North Andean margin: impact of the Carnegie Ridge collision, *Earth Planet. Sci. Lett.*, 168, 255-270, 1999.
- Gutscher, M.-A., J.-L. Olivet, D. Aslanian, J.-P. Eissen, and R. Maury, The "lost Inca Plateau": cause of flat subduction beneath Peru?, *Earth Planet. Sci. Lett.*, 171, 335-341, 1999.
- Gutscher, M.-A., N. Kukowski, J. Malavieille, and S. Lallemand, Material transfer in accretionary wedges from analysis of a systematic series of analog experiments, *J. Struct. Geol.*, 20, 407-416, 1998.

- Gutscher, M.-A., N. Kukowski, J. Malavieille, and S. Lallemand, Cyclical behavior of thrust wedges: Insights from high basal friction sandbox experiments, *Geology*, 24, 135-138, 1996.
- Hagen, R. A., and R. Moberly, Tectonic effects of a subducting aseismic ridge: the subduction of the Nazca Ridge at the Peru Trench, *Mar. Geophys. Res.*, 16, 145-161, 1994.
- Hampel, A., The migration history of the Nazca Ridge along the Peruvian active margin: a re-evaluation, *Earth Planet. Sci. Lett.*, 203, 2, 665-679, 2002.
- Hansen, D.L., S.B. Nielsen, and H. Lykke-Anderson, The post-Triassic evolution of the Sorgenfrei-Tornquist Zone - results from thermo-mechanical modelling, *Tectonophysics*, 328, 245-267, 2000.
- Hardy, S., C. Duncan, J. Masek, and D. Brown, Minimum work, fault activity and the growth of critical wedges in fold and thrust belts, *Basin Res.*, 10, 365-373, 1998.
- Hasegawa, A., and I.S. Sacks, Subduction of the Nazca Plate beneath Peru as determined from seismic observations, *J. Geophys. Res.*, 86, 4971-4980, 1981.
- Hassani, R., D. Jongmans, and J. Chéry, Study of plate deformation and stress in subduction processes using two-dimensional numerical models, *J. Geophys. Res.*, 108, 17951-17965, 1997.
- Heinbockel, R., Gravity and Magnetic Investigations Along the Peruvian Continental Margin, *Staats- u. Universitätsbibliothek Carl von Ossietzky*, Hamburg, 2003. Available from <http://www.sub-uni-hamburg.de/disse/877/dissertation.pdf>
- Hibbitt, Karlson, and Sorenson, ABAQUS/Standard User's Manual, Hibbitt, Karlson and Sorenson, Inc. Pawtucket, RI, USA, version 6.3, 2002.
- Hilde, T.W.C., Sediment subduction versus accretion around the Pacific, *Tectonophysics*, 99, 381-397, 1983.
- Hindle, D., J. Kley, E. Klosko, S. Stein, T. Dixon, and E. Norabuena, Consistency of geologic and geodetic displacements during Andean orogenesis, *Geophys. Res. Lett.*, 29, 8, 10.1029/2001GL013757, 2002.
- House, M.A., B.P. Wernicke, and K.A. Farley, Dating topography of the Sierra Nevada, California, using apatite (U-Th)/He ages, *Nature*, 396, 66-69, 1998.
- Houseman, G.A., and D. Gubbins, Deformation of subducted oceanic lithosphere, *Geophys. J. Intern.*, 131, 535-551, 1997.
- Hsu, J.T., Quaternary uplift of the Peruvian coast related to the subduction of the Nazca Ridge: 13.5 to 15.6 degrees south latitude, *Quatern. Intern.*, 15/16, 87-97, 1992.
- Hubbert, M.K., and W.W. Rubey, Role of fluid pressure in mechanics of overthrust faulting, I, Mechanics of fluid-filled solids and its application to overthrust faulting, *Geol. Soc. Am. Bull.*, 70, 115-166, 159, 1959.
- Hubbert, M.K., Theory of scale models as applied to the study of geological structures, *Geol. Soc. Am. Bull.*, 48, 459-1520, 1937.
- Huhn, K., Analyse der Mechanik des Makran Akkretionskeils mit Hilfe der Finiten und der Diskreten Element Methode sowie analoger Sandexperimente, *STR GFZ Potsdam*, 2002.
- Hussong, D.M., T.B. Reed, and W.A. Bartlett, SEAMARC II sonar imagery and bathymetry of the Nazca Plate and forearc, ODP Leg 112, in *Proceedings of the Ocean Drilling Program, Initial Reports*,

- col. 112, Ocean Drill. Program, College Station, Tex., 125-130, 1988.
- Hussong, D.M, and L.K. Wipperman, Vertical movement and tectonic erosion of the continental wall of the Peru-Chile trench near 11°30'S, in *Nazca Plate: Crustal Formation and Andean Convergence* edited by L. D. Kulm, J. Dymond, E. J. Dasch, and D.M. Hussong, *Geol. Soc. America Mem.* 154, 729-740, 1981.
- Ito, G., M. McNutt, and R.L. Gibson, Crustal structure of the Tuamotu Plateau, 15°S, and implications for its origin, *J. Geophys. Res.*, 100, B5, 8097-8114, 1995.
- Jarrard, R.D., Relations among subduction parameters, *Reviews Geophys.*, 24, 2, 217-284, 1986.
- Karig, D.E., and G.F. Sharman, Subduction and accretion in trenches, *Geol. Soc. Am. Bull.*, 86, 377-389, 1975.
- Kay, S.M., and J.M. Abruzzi, Magmatic evidence for Neogene lithospheric evolution of the central Andean "flat-slab" between 30°S and 32°S, *Tectonophysics*, 259, 15-28, 1996.
- Kearey, P., and F.J. Vine, *Global Tectonics*, Blackwell Scient. Publ, 2nd Edition, 1996.
- Kelleher, J., and W. McCann, Buoyant zones, great earthquakes and unstable boundaries of subduction, *J. Geophys. Res.*, 81, 4885-4896, 1976.
- Kennett, B.L.N., (ed.), IASPEI 1991 Seismological Tables, *Research School of Earth Sciences*, Australian National University, 1991.
- Kennett, J., *Marine Geology*, Prentice Hall, New York, 1982.
- Kirby, E., and K. Whipple, Quantifying differential rock-uplift rates via stream profile analysis, *Geology*, 29, 5, 415-418, 2001.
- Kley, J., and C.R. Monaldi, Tectonic shortening and crustal thickness in the Central Andes: How good is the correlation?, *Geology*, 26, 8, 723-726, 1998.
- Koch, E., Die Tektonik im Subandin des Mittel-Ucayali-Gebietes, Ostperu, *Geotekton. Forsch.* 15, 1-67, 1962.
- Kopp, C., J. Fruehn, E.R. Flueh, C. Reichert, N. Kukowski, J. Bialas, and D. Klaeschen, Structure of the Makran subduction zone from wide-angle and reflection seismic data, *Tectonophysics*, 329, 171-191, 2000.
- Kopp, H., D. Klaeschen, E.R. Flueh, J. Bialas, and C. Reichert, Crustal structure of the Java margin from seismic wide-angle and multichannel reflection data, *J. Geophys. Res.*, 107, B2, 10.1029/2000JB000095, 2002.
- Koyi, H., Analogue modelling: from a qualitative to a quantitative technique: a historical outline, *J. Petrol. Geol.*, 20, 223-283, 1997.
- Krabbenhoft, A., and the GEOPECO Working Group, Crustal structure of the Peruvian continental margin from wide-angle seismic studies, in prep.
- Krantz, R.W., Measurements of friction coefficients and cohesion for faulting and fault reactivation in laboratory models using sand and sand mixtures, *Tectonophysics*, 188, 203-207, 1991.
- Kukowski, N., and the GEOPECO Working group, Long-term and short-term tectonic erosion at the Peruvian active margin between 9°S and 15°S: evidence from bathymetry data and 3D sandbox analogue modelling, in prep.

- Kukowski, N., S.E. Lallemand, J. Malavieille, M.-A. Gutscher, and T.J. Reston, Mechanical decoupling and basal duplex formation observed in sandbox experiments with application to the Western Mediterranean Ridge accretionary complex, *Mar. Geol.*, 186, 29-42, 2002.
- Kukowski, N., T. Schillhorn, K. Huhn, U. von Rad, S. Husen, and E.R. Flueh, Morphotectonics and mechanics of the central Makran accretionary wedge off Pakistan, *Mar. Geology*, 173, 1-19, 2001.
- Kukowski, N., and I. Pecher, Thermo-hydraulics of the Peruvian accretionary complex at 12°S, *J. Geodyn.*, 27, 373-402, 1999.
- Kukowski, N., R. von Huene, J. Malavieille, and S.E. Lallemand, Sediment accretion against a buttress beneath the Peruvian continental margin at 12°S as simulated with sandbox modelling. *Geol. Rundschau*, 83, 822-831, 1994.
- Kulm, L.D., T.M. Thornburg, E. Suess, J. Resig, and P. Fryer, Clastic, diagenetic and metamorphic lithologies of a subsiding continental block: Central Peru forearc, in *Proc. ODP, Init. Rpts.*, 112 edited by E. Suess, R. von Huene et al., College Station, TX, (Ocean Drilling Program), 91-108, 1988.
- Kulm, L.D., J. Dymond, E.J. Dasch, and D.M. Hussong, Nazca Plate: Crustal Formation and Andean Convergence, *Geol. Soc. Am. Mem.*, 154, 1981.
- Kulm, L.D., J.M. Resig, T.C. Moore, and V.J. Rosato, Transfer of Nazca Ridge pelagic sediments to the Peru continental margin, *Geol. Soc. Am. Bull.*, 85, 769-780, 1974.
- Lallemand, S.E., P. Schnuerle, and J. Malavieille, Coulomb theory applied to accretionary and non-accretionary wedges: possible causes for tectonic erosion and/or frontal accretion, *J. Geophys. Res.*, 99, 6, 12033-12055, 1994.
- Lallemand, S.E., J. Malavieille, and S. Calassou, Effects of oceanic ridge subduction on accretionary wedges, experimental modeling and marine observations, *Tectonics*, 11, 6, 1301-1313, 1992.
- Lallemand, S.E., P. Schnuerle, and S. Manoussis, Reconstruction of subduction zone paleo-geometries and quantification of upper plate material losses caused by tectonic erosion, *J. Geophys. Res.*, 99, B7, 12033-12055, 1992.
- LaVision, Manual for DaVis 6.2, LaVision GmbH, Goettingen, 2002.
- LeFevre, L.V., and K. McNally, Stress distribution and subduction of aseismic ridges in the Middle America subduction zone, *J. Geophys. Res.*, 90, B6, 4495-4510, 1985.
- Le Roux, J.P., C. Tavares Correa, and F. Alayza, Sedimentology of the Rímac-Chillón alluvial fan at Lima, Peru, as related to Plio-Pleistocene sea level changes, glacial cycles and tectonics, *J. South Am. Earth Sci.*, 13, 499-510, 2000.
- Li, C., and A.L. Clark, Tectonic effects of the subducting Nazca Ridge on the Southern Peru continental margin, *Mar. Petrol. Geol.*, 11, 5, 575-586, 1994.
- Liu, J.Y., and G. Ranalli, Stresses in an overthrust sheet and propagation of thrusting: an airy stress function solution, *Tectonics*, 11, 3, 549-559, 1992.
- Lohrmann, J., N. Kukowski, J. Adam, and O. Oncken, Geometry and internal kinematics of convergent sand wedges controlled by material parameters, *J. Struct. Geol.*, in press.
- Lohrmann, J., Simulation of tectonically erosive and accretive mass-transfer modes at the the North

- and South Chilean forearc with 2D scaled sandbox experiments, *STR GFZ Potsdam*, 2002.
- Luetgert, J.H., MacRay-interactive two-dimensional seismic ray-tracing for the Macintosh, *US Geological Survey Open File Report*, 92-356, 43pp, 1992.
- Macharé, J., and L. Ortlieb, Plio-Quaternary vertical motions and the subduction of the Nazca Ridge, central coast of Peru, *Tectonophysics*, 205, 97-108, 1992.
- Maekel, G., and J. Walters, Finite-element analyses of thrust tectonics: computer simulation of detachment phase and development of thrust faults, *Tectonophysics*, 226, 167-185, 1993.
- Mandl, G., *Mechanics of tectonic faulting: Models and basic concepts*, 407pp, Elsevier, New York, 1988.
- Marone, C., Laboratory-derived friction laws and their application to seismic faulting, *Annu. Rev. Earth. Planet. Sci.*, 26, 643-696, 1998.
- Marques, F.O., and P.R. Cobbold, Topography as a major factor in the development of arcuate thrust belts: Insights from sandbox experiments, *Tectonophysics*, 348, 247-268, 2002..
- Mayes, C.L., L.A. Lawver, and D.T. Sandwell, Tectonic history and new isochron chart of the South Pacific, *J. Geophys. Res.*, 95, 8543-8567, 1990.
- McCann, W.R., and R.E. Habermann, Morphologic and geologic effects of the subduction of bathymetric highs, *Pure Appl. Geophys.*, 129, 1-2, 41-69, 1989.
- McGeary, S., A. Nur, and Z. Ben-Avraham, Spatial gaps in arc volcanism: The effect of collision or subduction of oceanic plateaus, *Tectonophysics*, 119, 195-221, 1985.
- Mégard, F., D.C. Noble, E.H. McKee, and E. Bellon, Multiple phases of Neogene compressive deformation in the Ayacucho intermontan basin, Andes of Central Peru, *Geol. Soc. Am. Bull.*, 95, 1108-1117, 1984.
- Mégard, F., and H. Philip, Plio-Quaternary tectono-magmatic zonation and plate tectonics in the Central Andes, *Earth Planet. Sci. Lett.*, 33, 231-238, 1976.
- Mohr, G.A., *Finite Elements for solids, fluids and optimization*, *Oxford Science Publications*, 1992.
- Mohr, A., and N. Kukowski, 3D-Finite-Element model of seamount subduction applied to the Costa Rican margin, *MARGINS Meet.*, Kiel, 2001.
- Moore, G.F., T.H. Shipley, and P. Lonsdale, Subduction erosion versus sediment offscraping at the toe of the Middle America Trench off Guatemala, *Tectonics*, 5 (4), 513-523, 1986.
- Moretti, I., *Subduction des rides aséismique*, Thèse Doct. Univ., Univ. Paris XI, Orsay, 1982.
- Mueller, R.D., W.R. Roest, J.-Y. Royer, L.M. Gahagan, and J.G. Sclater, Digital isochrons of the world's ocean floor, *J. Geophys. Res.* 102, 3211-3214, 1997.
- Mulugeta, G., and H. Koyi, Three-dimensional geometry and kinematics of experimental piggyback thrusting, *Geology*, 15, 1052-1056, 1987
- Mulugeta, G., Modelling the geometry of Coulomb thrust wedges, *J. Struct. Geol.*, 10, 8, 847-859, 1988.
- Munsch, M., C. Antoine, and A. Gachon, Evolution tectonique de la région des Tuamotu, océan Pacifique Central, *C.R. Acad. Sci. Paris*, 33, 941-948, 1996.
- Mutter, C. Z. and J.C. Mutter, Variations in thickness of layer 3 dominate oceanic crustal structure, *Earth Planet. Sci. Lett.*, 117, 295-317, 1993.

- Noble, D.C., E.H. McKee, E. Farrar, and U. Petersen, Episodic Cenozoic volcanism and tectonism in the Andes of Peru, *Earth Planet. Sci. Lett.*, 21, 213-220, 1974.
- Noblet, C., A. Lavenue, and R. Marocco, Concept of continuum as opposed to periodic tectonism in the Andes, *Tectonophysics*, 255, 65-78, 1996.
- Norabuena, E., T.H. Dixon, S. Stein, and C.G.A. Harrison, Decelerating Nazca-South America and Nazca-Pacific Plate motions, *Geophys. Res. Lett.*, 26, 22, 3405-3408, 1999.
- Norabuena, E., L. Leffler-Griffin, A. Mao, T. Dixon, S. Stein, I.S. Sacks, L. Ocola, and M. Ellis, Space geodetic observations of Nazca-South American convergence across the Central Andes, *Science*, 279, 358-362, 1998.
- Nur, A., and Z. Ben-Avraham, Volcanic gaps and the consumption of an aseismic ridge in South America, in *Nazca Plate: Crustal Formation and Andean Convergence* edited by L. D. Kulm, J. Dymond, E. J. Dasch, and D.M. Hussong, *Geol. Soc. America Mem.* 154, 729-740, 1981.
- Okal, E.A., and C.R. Bina, The deep earthquakes of 1997 in Western Brazil, *Bull. Seismol. Soc. Am.*, 91, 1, 161-164, 2001.
- Okal, E.A., and C.R. Bina, The deep earthquakes of 1921-1922 in Northern Peru, *Phys. Earth Planet. Inter.*, 87, 33-54, 1994.
- Okal, E.A., and A. Cazenave, A model for the plate tectonic evolution of the East-Central Pacific based on SEASAT investigations, *Earth Planet. Sci. Lett.*, 72, 99-116, 1985.
- Pardo-Casas, F., and P. Molnar, Relative motion of the Nazca (Farallon) and South American Plates since Late Cretaceous time, *Tectonics*, 6, 233-248, 1987.
- Peacock, S.M., Numerical simulations of metamorphic pressure-temperature-time paths and fluid production in subducting slabs, *Tectonics*, 9, 1197-1211, 1990.
- Perg, L.A., R.S. Anderson, and R.C. Finkel, Use of new ¹⁰Be and ²⁶Al inventory method to date marine terraces, Santa Cruz, California, USA, *Geology*, 29, 10, 879-882, 2001.
- Persson, K.S., D. and Sokoutis, Erosion of orogenic wedges - a sandbox view, *Geol. Soc. Greece Bull.*, 1, 467-473, 2001.
- Petford, N., and M.P. Atherton, Crustal segmentation and the isotopic significance of the Abancay Deflection: Northern Central Andes (9-20°S), *Revista Geol. Chile*, 22, 235-243, 1995.
- Pilger, R.-H., Plate reconstructions, aseismic ridges, and low-angle subduction beneath the Andes, *Geol. Soc. Am. Bull.*, 92, 448-456, 1981.
- Pilger, R.H., and D. W. Handschumacher, The fixed hotspot hypothesis and origin of the Easter-Salas y Gomez-Nazca trace, *Geol. Soc. Am. Bull.*, 92, 437-446, 1981.
- Platt, J.P., J.K. Legett, J. Young, H. Raza, and S. Alam, Large-scale sediment underplating in the Makran accretionary prism, south-west Pakistan, *Geology*, 13, 507-511, 1985.
- Poulet, A., H. Cambray, J.-P. Cadet, J. Bourgois, and P. De Wever, Volcanic ash from Leg 112 off Peru, in *Proc. ODP, Sci. Rpts.*, 112 edited by E. Suess, R. von Huene et al., College Station, TX, (Ocean Drilling Program), 465-479, 1990.
- Ranalli, G., R. Pellegrini, and S. D'Offizi, Time dependence of negative buoyancy and the subduction of continental lithosphere, *J. Geodyn.*, 30, 539-555, 2000.

- Ranalli, G., Rheology of the Earth, *Chapman and Hall*, 2nd edition, 1995.
- Ranero, C. R., and R. von Huene, Subduction erosion along the middle America convergent margin, *Nature*, 404, 748-752, 2000.
- Regenauer-Lieb, K., D.A. Yuen, and J. Branlund, The initiation of subduction: Criticality by addition of water?, *Science*, 294, 578-580, 2001.
- Regenauer-Lieb, K., and D.A. Yuen, Quasi-adiabatic instabilities associated with necking processes of an elasto-viscoplastic lithosphere, *Phys. Earth Planet. Interiors*, 89-102, 2000.
- Resig, J.M., Benthic foraminiferal Stratigraphy and Paleoenvironments off Peru, leg 112, in *Proc. ODP, Sci. Rpts.*, 112 edited by E. Suess, R. von Huene et al., College Station, TX, (Ocean Drilling Program), 263-296, 1990.
- Richards, M.A., and G.F. Davies, On the separation of relatively buoyant components from subducted lithosphere, *Geophys. Res. Lett.*, 16, 831-834, 1989.
- Richardson, R.M., Finite element modelling of stress in the Nazca plate: driving forces and plate boundary earthquakes, *Tectonophysics*, 50, 223-248, 1978.
- Rosata, V.J., and L.D. Kulm, Clay mineralogy of the Peru continental margin and adjacent Nazca Plate: Implications for provenance, sea level changes, and continental accretion, in *Nazca Plate: Crustal Formation and Andean Convergence* edited by L. D. Kulm, J. Dymond, E. J. Dasch, and D.M. Hussong, *Geol. Soc. America Mem.* 154, 545-568, 1981.
- Royden, L.H., The tectonic expression of slab pull at continental convergent plate boundaries, *Tectonics*, 12, 303-325, 1993.
- Rutland, R.W.R, Andean orogeny and ocean floor spreading, *Nature*, 233, 252-255, 1971.
- Schellart, W.P., Shear test results for cohesion and friction coefficients for different granular materials; scaling implications for their usage in analogue modelling, *Tectonophysics*, 324, 1-16, 2000.
- Schnuerle, P., C.-S. Liu, S.E. Lallemand, and D.L. Reed, Structural insight into the south Ryukyu margin: effects of the subducting Gagua Ridge, *Tectonophysics*, 288, 237-250, 1998.
- Scholl, D.W., R. von Huene, T.L. Vallier, and D.G. Howell, Sedimentary masses and concepts about tectonic processes at underthrust ocean margins, *Geology*, 8, 564-568, 1980.
- Scholl, D.W., M.N. Christensen, R. von Huene, and M.S. Marlow, Peru-Chile trench sediments and sea-floor spreading, *Geol. Soc. Am. Bull.*, 81, 1339-1360, 1970.
- Scholz, C.H., and C. Small, The effect of seamount subduction on seismic coupling, *Geology*, 25, 6, 487-490, 1997.
- Schrader, H., and J.C. Castaneda, The Ballena and Delfin wells off Central Peru: revised ages, in: E. Suess, R. von Huene et al. (Eds) *Proc. ODP, Init. Rpts. 112*, College Station, TX, (Ocean Drilling Program), pp. 209-215, 1990.
- Schweller, W.J., L.D. Kulm, and R.A. Prince, Tectonics, structure and sedimentary framework of the Peru-Chile trench, in *Nazca Plate: Crustal Formation and Andean Convergence* edited by L.D. Kulm, J. Dymond, E.J. Dasch, and D.M. Hussong, *Geol. Soc. America Mem.* 154, 323-349, 1981.
- Screaton, E.J., D.R. Wuthrich and S.J., Dreiss, Permeabilities, fluid pressures and flow rates in the Barbados ridge complex, *J. Geophys. Res.*, 95, 8997-9007, 1990.

- Sébrier, M., A. Lavenue, M. Fornari, and J.P. Soulas, Tectonics and uplift in the Central Andes (Peru, Bolivia, and Northern Chile) from Eocene to present, *Géodynam.*, 3, 85-106, 1988.
- Sébrier, M., J.L. Mercier, J. Macharé, D. Bonnot, J. Cabrera, and J.L. Blanc, The state of stress in an overriding plate situated above a flat slab: The Andes of Central Peru, *Tectonics*, 7, 4, 895-928, 1988.
- Sébrier, M., J.L. Mercier, F. Mégard, B. Laubacher, and E. Carey-Gailhardis, Quaternary normal and reverse faulting and the state of stress in the Central Andes of South Peru, *Tectonics*, 4, 7, 739-780, 1985.
- Shipboard Scientific Party, Leg 202, Preliminary Report, *ODP Prelim. Rpt.*, 102, 2002. Available from http://www-odp.tamu.edu/publications/prelim/202_prel/202PREL.PDF.
- Siame, L.L., D.L. Bourlès, M. Sébrier, O. Bellier, J.C. Castano, M. Araujo, M. Perez, G.M. Raisbeck, and F. Yiou, Cosmogenic dating ranging from 20 to 700 ka of a series of alluvial fan surfaces affected by the El Tigre fault, Argentina, *Geology*, 25, 975-978, 1997.
- Smith, W.H.F., and D.T. Sandwell, Global Seafloor Topography from Satellite Altimetry and Ship Depth Soundings, *Science*, 277, 1956-1962, 1997a.
- Smith, W.H.F., and D.T. Sandwell, Marine gravity from Geosat and ERS 1 Satellite altimetry, *J. Geophys. Res.*, 102, B5, 10039-10054, 1997b.
- Somoza, R., Updated Nazca (Farallon)- South America relative motions during the last 40 My: implications for mountain building in the central Andean region, *J. South Am. Earth Sci.*, 11, 3, 211-215, 1998.
- Spence, W., C. Mendoza, E.R. Engdahl, G.L. Choy, and E. Norabuena, Seismic subduction of the Nazca Ridge as shown by the 1996-97 Peru earthquakes, *Pure Appl. Geophys.*, 154, 753-776, 1999.
- Spikings, R.A., W. Winkler, D. Seward, and R. Handler, Along-strike variations in the thermal and tectonic response of the continental Ecuadorian Andes to the collision with heterogeneous oceanic crust, *Earth Planet. Sci. Lett.*, 186, 57-73, 2001.
- Stein, S., J.E. Engeln, C. DeMets, R.G. Gordon, D. Woods, P. Lundgren, D. Argus, C. Stein, and D.A. Wiens, The Nazca-South America convergence rate and the recurrence of the great 1960 Chilean earthquake, *Geophys. Res. Lett.*, 13, 713-716, 1986.
- Storti, F., and K. McClay, Influence of syntectonic sedimentation on thrust wedges in analogue models, *Geology*, 23, 11, 999-1002, 1995.
- Suess, E., R. von Huene et al., *Proc. ODP, Sci. Results*, 112, College Station, TX, (Ocean Drilling Program), 1990.
- Suess, E., R. von Huene et al., *Proc. ODP, Init. Rpts.*, 112, College Station, TX, (Ocean Drilling Program), 1988.
- Swenson, J., and S. Beck, Source Characteristics of the 12 November 1996 M(w) 7.7 Peru subduction zone earthquake, *Pure Appl. Geophys.*, 154, 731-751, 1999.
- Talandier, J., and E.A. Okal, Crustal structure in the Society and Tuamotu Islands, French Polynesia, *Geophys. J. R. astr. Soc.*, 88, 499-528, 1987.
- Tapponnier, P., and P. Molnar, Slip-line field theory and large-scale continental tectonics, *Nature*, 264,

- 319-324, 1976.
- Thomas, J.N., An improved accelerated initial stress procedure for elasto-plastic finite element analysis, *Intern. J. Num. Analyt. Mathem. Geomech.*, 8, 359-379, 1984.
- Toksoez, M.N., J.W. Minear, and B.R. Julian, Temperature field and geophysical effects of a downgoing slab, *J. Geophys. Res.*, 76, 1113-1138, 1971.
- Trummer, I., and E.R. Flueh and the Paganini Working Group, Seismic constraints on the crustal structure of Cocos Ridge off the coast of Costa Rica, *N. Jb. Geol. Paleont. Abh.*, 255, 1, 25-37, 2002.
- Turcotte, D.L., and G. Schubert, *Geodynamics*, Cambridge Univers. Press, 2nd edition, 2002.
- Turcotte, D.L., D.C. McAdoo, and J.G. Caldwell, An elastic-perfectly plastic analysis of the bending of the lithosphere at a trench, *Tectonophysics*, 47, 193-205, 1978.
- van den Beukel, J., and R. Wortel, Temperatures and shear stresses in the upper part of a subduction zone, *Geophys. Res. Lett.*, 14, 10, 1057-1060, 1987.
- van Hunen, J., A.P. van den Berg, and N.J. Vlaar, A thermo- mechanical model of horizontal subduction below an overriding plate, *Earth Planet. Sci. Lett.* 182, 157-169, 2000.
- Vanneste, L.E., and R.D. Larter, Sediment subduction, subduction erosion, and strain regime in the northern South Sandwich forearc, *J. Geophys. Res.*, 107, B7, 10.1029/2001JB000396, 2002.
- Vannucchi, P., D.W. Scholl, M. Meschede, and K. McDougall-Reid, Tectonic erosion and consequent collapse of the Pacific margin of Costa Rica: Combined implications from ODP Leg 170, seismic offshore data, and regional geology of the Nicoya Peninsula, *Tectonics*, 20, 649-668, 2001.
- Vogt, P.R., A. Lowrie, D.R. Brace, and R.N. Hey, Subduction of aseismic oceanic ridges: effects on shape, seismicity and other characteristics of consuming plate boundaries, *Geol. Soc. Am. Bull. Spec. Paper*, 172, 1976.
- von Huene, R., and I. Pecher, Vertical tectonics and the origins of BSRs along the Peru margin, *Earth Planet. Sci. Lett.*, 166, 47-55, 1999.
- von Huene, R., W. Weinrebe, and F. Heeren, Subduction erosion along the North Chile margin, *J. Geodyn.*, 27, 345 - 358, 1999.
- von Huene, R., J. Corvalan, E.R. Flueh, K. Hinz, J. Korstgard, C. Ranero, and W. Weinrebe, CONDOR Scientists, Tectonic control of the subducting Juan Fernandez Ridge on the Andean margin near Valparaiso, Chile, *Tectonics*, 16, 3, 474-488, 1997.
- von Huene, R., I. Pecher, and M.-A. Gutscher, Development of the accretionary prism along Peru and material flux after subduction of Nazca Ridge, *Tectonics*, 15, 19-33, 1996.
- von Huene, R., D. Klaeschen, B. Cropp, and J. Miller, Tectonic structure across the accretionary and erosional parts of the Japan Trench, *J. Geophys. Res.*, 99, B11, 22349-22361, 1994.
- von Huene, R., and D.W. Scholl, Observations at convergent margins concerning sediment subduction, sediment erosion, and the growth of continental crust, *Reviews Geophys.*, 29, 3, 279-316, 1991.
- von Huene, R., and S. Lallemand, Tectonic erosion along the Japan and Peru convergent margins, *Geol. Soc. Am. Bull.*, 102, 704-720, 1990.
- von Huene, R., E. Suess, Leg 112 shipboard scientific party, Ocean Drilling Program Leg 112, Peru

- continental margin: Part 1: Tectonic history, *Geology*, 16, 934-938, 1988.
- Walther, C., Crustal structure of the Cocos Ridge northeast of Cocos Island, Panama Basin, *Geophys. Res. Lett.*, 29, 20, 1986, doi:10.1029/2001GL014267, 2002.
- Wang, K., Kinematic models of dewatering accretionary prisms, *J. Geophys. Res.*, 99, 4429-4438, 1994.
- Wessel, P., and W.H.F. Smith, Free software helps map and display data, *EOS Transactions, AGU*, 72, 441, 1991.
- Wieneke, B., PIV adaptive multi-pass correlation with deformed interrogation windows, *PIV Challenge*, 1-6, 2001.
- Willett, S.D., and M.T. Brandon, On steady states in mountain belts, *Geology*, 30, 175-178, 2002.
- Winder, R.O., and S.M. Peacock, Viscous forces acting on subducting lithosphere, *J. Geophys. Res.*, 106, B10, 21937-21951, 2001.
- Wipf, M., D. Seward, and F. Schlunegger, Preliminary fission track data on the effects of the subducting Nazca Ridge on the geomorphology in South-Central Peru, 5th Intern. Symp. And. Geodyn., 2002.
- Wolf, R.A., K.A. Farley, and L.T. Silver, Assessment of (U-Th)/He thermochronometry: The low-temperature history of the San Jacinto mountains, California, *Geology*, 25, 65-68, 1997.
- Woods, T.M., and E.A. Okal, The structure of the Nazca Ridge and Sala y Gomez seamount chain from dispersion of Rayleigh waves, *Geophys. J. Intern.*, 117, 205-222, 1994.
- Wu, P., Postglacial induced surface motion and gravity in Laurentia for uniform mantle with power-law rheology and ambient tectonic stress, *Earth Planet. Sci. Lett.*, 186, 427-435, 2001.
- Wu, P., Modelling postglacial sea levels with power-law rheology and a realistic ice model in the absence of ambient tectonic stress, *Geophys. J. Intern.*, 139, 691-702, 1999.
- Yoshioka, S., and M.J.R. Wortel, Three-dimensional numerical modeling of detachment of subducted lithosphere, *J. Geophys. Res.*, 100, B10, 20223-20244, 1995.
- Zelt, C.A., and R.B. Smith, Seismic traveltimes inversion for 2-D crustal velocity structure, *Geophys. J. Intern.*, 108, 16-34, 1992.
- Zhong, S., and M. Gumis, Controls on trench topography from dynamic models of subducted slabs, *J. Geophys. Res.*, 99, 15683-15695, 1994.
- Zienkiewicz, O.C., and R.L. Taylor, The finite element method. McGraw-Hill, London, 1987.
- Zoback, M.L., and M. Zoback, State of stress in the conterminous United States, *J. Geophys. Res.*, 85, 6113-6156, 1980.

7 Acknowledgements

First of all, I thank Nina Kukowski for giving me the opportunity to join the GEOPECO project and for her continued, highly valuable support and advice. The thesis benefitted from many interesting discussions with her. I would like to thank her and Joerg Bialas as the co-chief scientists of the RV "Sonne" cruises SO146 1&2 for the successful work (during which the term "OBS-Fischerei" got a new meaning) and for the pleasant time onboard. Joerg Bialas provided extremely helpful advice with the wide-angle seismic data, and fruitful discussions with him and Anne Krabbenhoef helped to clarify the data interpretation. Many thanks go to the participants of cruises SO146 1&2 for their help during data acquisition and processing. In particular, I thank Christian Huebscher and Raffaella Heinbockel for providing the reflection seismic data and the results of the gravity and magnetic modelling, respectively. The SEAMARC II data was made available by Greg Moore.

I wish to thank very much the referee Onno Oncken and co-referee Hans-Juergen Goetze for accepting the examination of the thesis and their valuable comments.

Many thanks go to Silvan Hoth and Jo Lohrmann for their support in all aspects of carrying out the analogue experiments. I would like to thank especially Juergen Adam, who, with encouraging enthusiasm, spent a lot of his time and even more of his patience on the sophisticated PIV monitoring and processing. Katrin Huhn and Axel Mohr are thanked for providing input for the initial numerical models.

Patrick Wu, Kasper Fischer, Klaus Regenauer-Lieb and Gabriele Morra provided valuable help in overcoming problems encountered during realization of the numerical models in ABAQUS, which I gratefully acknowledge. I would like to thank Yuri Podladchikov for interesting discussions on numerical modelling approaches and his invitation to the Structural Geology seminar at the ETH Zurich. During my visit to Switzerland, I enjoyed the inspiring discussions with Diane Seward, Martin Wipf and Fritz Schlunegger about their onshore work in Peru. Edmundo Norabuena, Udo Barckhausen and Garrett Ito are thanked for their helpful comments during the work on the migration history of the Nazca Ridge. This part of the thesis furthermore benefitted from reviews by Emile Okal, Tim Dixon and Steven Cande.

Thanks to all colleagues at GEOMAR, Kiel, and the GFZ Potsdam for creating a pleasant working atmosphere. In particular, I would like to thank my room-mate Matthias Rosenau for three years of good fellowship. Ulrich Riller, David Hindle and Ralf Hetzel are thanked for interesting discussions on geologic implications of parts of this thesis and on numerous other topics, thereby widening my knowledge substantially.

The German Ministry of Education, Science and Technology (BMBF) provided funding from March 2000 to April 2002 within the GEOPECO project (grant no. 03G0146A). I thank Onno Oncken for giving me the opportunity to work as guest scientist at the GFZ Potsdam from May 2000 to April 2002. From May 2002 to April 2003, Onno Oncken provided financial support through the Leibniz program of the German Science Foundation (DFG) that I gratefully acknowledge.

Finally, I wish to warmly thank my mother and grandparents for always being interested in my work and their continuous trust and support.

Curriculum vitae

Name	Andrea Hampel
Date and place of birth	14.04.1975 in Ludwigsburg
Citizenship	German

Education

June 1994	Allgemeine Hochschulreife, Gymnasium Eschwege
September 1994 – February 2000	Study of Geophysics, Chr.-Albrechts-University, Kiel
February 2000	Diploma in Geophysics

Positions held

March 2000 - April 2002	Research assistant at the GEOMAR Research Center for Marine Geosciences, Kiel; guest scientist at the GeoForschungsZentrum Potsdam
May 2002 – April 2003	Research assistant at GFZ Potsdam

Honours

November 2002	Bernd-Rendel-Award of the German Science Foundation (DFG)
---------------	---



Erklärung

Hiermit versichere ich, dass ich die vorliegende Arbeit selbständig verfasst und dabei keine anderen als die angegebenen Hilfen und Hilfsmittel benutzt habe.